

ELECTROSTATIC WAVES GENERATED BY GASES
INTERACTING WITH FLOWING PLASMAS

by

Ti-Ze Ma

A thesis submitted in partial fulfillment
of the requirements for the Doctor of
Philosophy degree in Physics
in the Graduate College of
The University of Iowa

August 1986

Thesis supervisor: Professor Donald A. Gurnett

Graduate College
The University of Iowa
Iowa City, Iowa

CERTIFICATE OF APPROVAL

PH.D. THESIS

This is to certify that the Ph.D. thesis of

Ti-Ze Ma

has been approved by the Examining Committee
for the thesis requirement for the Doctor of
Philosophy degree in Physics at the August 1986
graduation.

Thesis committee:

Daniel A. Huettner
Thesis supervisor

Christopher K. Anderson
Member

D. S. Kline
Member

Karl E. Long
Member

Dwight Nicholson
Member

ACKNOWLEDGEMENTS

The author wishes to express great appreciation to his advisor, Professor D. A. Gurnett, for his guidance throughout this study. The author thanks Dr. N. Omid for valuable discussions and cooperations. The author thanks Ms. Kathy Kurth for typing the thesis and Ms. Joyce Chrisinger for drawing the graphs in the thesis. The author also thanks all professors, staff and graduate students in the Department of Physics and Astronomy. The author thanks his wife, Fan Xiao, for her support and encouragement.

The research at the University of Iowa was supported by grants N00014-82-K-0183 and N00014-85-K-0404 with the Office of Naval Research, NGL-16-001-043 with NASA Headquarters and contract 954013 with the Jet Propulsion Laboratory.

ABSTRACT

Intense electrostatic waves are often observed during interactions between neutral gases and rapidly moving plasma. These waves usually have a broad bandwidth, typically from a few Hz to a few kHz. Two examples are analyzed in detail, (1) the shock-like waves associated with the AMPTE solar wind releases, and (2) waves associated with Titan's wake. In both cases the waves are believed to be caused by an electrostatic instability between the flowing plasma and the nearly stationary plasma produced by ionization of the neutral gas. The analysis shows that this beam-plasma instability gives high growth rates and frequencies in the proper frequency range. The growth rate is quite sensitive to the ion densities and is large only in regions where the two plasmas have similar densities. This study is also supported by particle simulations which show that the waves produce considerable ion heating.

TABLE OF CONTENTS

	Page
LIST OF TABLES	v
LIST OF FIGURES	vi
CHAPTER I. INTRODUCTION	1
CHAPTER II. ELECTROSTATIC INSTABILITIES IN THE MULTICOMPONENT PLASMAS	4
CHAPTER III. THE SHOCK-LIKE NOISE ASSOCIATED WITH THE AMPTE SOLAR WIND LITHIUM RELEASES	11
3.1 Summary of Observations	11
3.2 Instability Analysis	14
CHAPTER IV. THE SHOCK-LIKE NOISE ASSOCIATED WITH THE AMPTE SOLAR WIND BARIUM RELEASES	23
4.1 Summary of Observations	23
4.2 Instability Analysis	25
CHAPTER V. THE SHEATH NOISE OBSERVED BY VOYAGER 1 IN TITAN'S WAKE	32
5.1 Summary of Observations	32
5.2 Instability Analysis	35
CHAPTER VI. COMPARISON WITH THE PLASMA SIMULATION RESULT . .	44
CHAPTER VII. CONCLUSIONS	48
REFERENCES	152

LIST OF TABLES

	Page
Table 1. Parameters used for the analysis of the sheath noise in Titan's wake.	52

LIST OF FIGURES

	Page
Figure 1. A sketch map of complex z -plane for evaluating the plasma dispersion function, $Z(z)$. The power series expansion is used in region I, Salzer's method in region II, continued fraction in region III, and asymptotic expansion in region IV.	54
Figure 2. A summary of the plasma density, magnetic field, and electric field observations for the AMPTE solar wind lithium release on September 20, 1984. The intense burst of electrostatic noise occurred in the region where the lithium ion density, N_{Li}^+ , is comparable to the solar wind proton density, N_p	56
Figure 3. The peak and average electric field spectrums at 0956:19.53 UT on September 20, 1984. The main power of the noise is within frequencies below 1 kHz.	58
Figure 4 A model for the instability calculation. Lithium ions are stationary, protons drift with solar wind velocity, V_{sw} , two groups of	

electrons (hot and cold) drift with a velocity,
 V_D , between 0 and V_{sw} 60

Figure 5. A representative growth rate calculation in the
lithium case as $\vec{k} \parallel \vec{V}_{sw}$. The upper panel shows the
 $k\lambda_D$, wave number normalized by the Debye length,
as a function of frequency and the lower panel
shows the growth rate, γ , as a function of
frequency. The solid curves are for the case
 $N_e^c = 0$ and the dashed curves are for the case
 $N_e^c = N_{Li}^+$, assuming $N_{Li}^+ = N_p = 8 \text{ cm}^{-3}$ 62

Figure 6. The plots of the frequency of marginal instability
marked $\gamma = 0$, and the frequency for the maximum
growth rate, the dashed curve marked γ_{max} as the
functions of the lithium to proton density ratio,
 N_{Li}^+/N_p , for the case $\vec{k} \parallel \vec{V}_{sw}$, $N_e^c = 0$ 64

Figure 7. The similar plots as in Figure 6 for the case
 $N_e^c = N_{Li}^+$ 66

Figure 8. The maximum growth rates, γ_{max} , as the functions
of N_{Li}^+/N_p , for the case $\vec{k} \parallel \vec{V}_{sw}$. The solid curve
is for the case $N_e^c = 0$, and the dashed curve is
for the case $N_e^c = N_{Li}^+$ 68

Figure 9. Illustration for the current effect to the
marginal instability boundary. The cross-hatched

region shows the variation in the $\gamma = 0$ boundary for a $\pm 25\%$ variation in the electron drift velocity.	70
Figure 10. Plots of maximum growth rates, γ_{\max} , versus θ , the angle between \vec{k} and \vec{V}_{sw} for the case $N_{\text{Li}^+} =$ $N_p = 8 \text{ cm}^{-3}$. The solid curve is for $N_e^c = 0$, and the dashed curve is for $N_e^c = N_{\text{Li}^+}$	72
Figure 11. A plot of $k\lambda_D$, wave number normalized by the Debye length of the plasma, as a function of frequency (upper panel) and γ , growth rate, as a function of frequency (lower panel) for the case $N_{\text{Li}^+} = N_p = 8 \text{ cm}^{-3}$, $N_e^c = 0$, and $\theta = 82^\circ$	74
Figure 12. Plots of $f_{\gamma=0}$, the frequency for the marginal instability, vs. N_{Li^+}/N_p , lithium to proton density ratio; γ_{\max} , maximum growth rate (maximized over k and θ), vs. N_{Li^+}/N_p , and f_{\max} , the frequency for the maximum growth rate, vs. N_{Li^+}/N_p . Assume $N_p = 8 \text{ cm}^{-3}$, $N_e^c = 0$	76
Figure 13. The same plots as in Figure 12 for $N_e^c = N_{\text{Li}^+}$	78
Figure 14. A plot of the plasma density obtained from the electron plasma oscillation (top panel) and the magnetic field from the magnetometer (bottom panel) during the solar wind barium release on December 27, 1984. The diamagnetic cavity and the compression region are indicated.	80

Figure 15.	A 16-channel electric field intensity plot. The shock-like noise is observed near the outer boundary of the plasma compression region. It lasts about 1 minute.	82
Figure 16.	The spectrums of the intense shock-like electrostatic noise at the time 1234:28 and 1234:40 UT. Most of the power in this noise is concentrated at frequencies below a few hundred Hz.	84
Figure 17.	A model for the instability analysis for the artificial comet experiment. Barium ions are stationary, protons stream through the barium plasma with the solar wind velocity. Two groups of electrons (hot and cold) drift with a velocity, V_D , between 0 and V_{sw}	86
Figure 18.	A representative growth rate calculation for $N_{Ba}^+ = 10 N_p = 80 \text{ cm}^{-3}$, $N_e^c = N_{Ba}^+$, $\theta = 0$. The upper panel shows $k\lambda_D$ vs. frequency and the lower panel shows γ vs. frequency.	88
Figure 19.	A plot of the frequency for the marginal stability, labelled $\gamma = 0$, and the frequency for the maximum growth rate, the dashed curve marked γ_{max} , as the functions of N_{Ba}^+/N_p , the barium to proton density ratio for $\theta = 0^\circ$, $N_e^c = 0$	90
Figure 20.	The same plot as in Figure 19 for $N_e^c = N_{Ba}^+$	92

Figure 21.	A plot of the maximum growth rates versus N_{Ba}^+/N_p for $\theta = 0^\circ$. The solid curve is for $N_e^c = 0$ and the dashed curve is for $N_e^c = N_{Ba}^+$	94
Figure 22.	Plots of maximum growth rates versus θ for $N_{Ba}^+ = 10 N_p = 80 \text{ cm}^{-3}$. The solid curve is for the case $N_e^c = 0$ and the dashed curve is for the case $N_e^c = N_{Ba}^+$	96
Figure 23.	Plots of $k\lambda_D$ vs. f (upper panel) and γ vs f (lower panel) for $N_e^c = 0$, $N_{Ba}^+ = 10 N_p = 80 \text{ cm}^{-3}$, $\theta = 85.5^\circ$	98
Figure 24.	Plots of the frequency for the marginal instability, $f_{\gamma=0}$, vs. N_{Ba}^+/N_p , the barium to proton density ratio and the maximum growth rate, γ_{max} , vs. N_{Ba}^+/N_p , and the frequency corresponding to the maximum growth rate, f_{max} , vs. N_{Ba}^+/N_p for the case $N_p = 8 \text{ cm}^{-3}$, $N_e^c = 0$. The angle, θ , for this plot is the one which corresponds to the peak value of γ_{max}	100
Figure 25.	The same plots as in Figure 24 for $N_e^c = N_{Ba}^+$	102
Figure 26.	Titan and its environment during Voyager 1 flyby. Magnetospheric plasma flows around Titan. Voyager 1 trajectory, projected in the Saturnian equatorial plane, is shown. The sheath noise was observed in the cross-hatched region.	104

Figure 27.	Upper panel shows the plasma density along the Voyager 1 trajectory. The dashed line indicates the plasma density level of the magnetosphere near Titan's orbit, which is 0.3 cm^{-3} . The lower panel shows the electric field intensities. The sheath noise occurs from 0532:30 to 0538:30 SCET.	106
Figure 28.	A spectrum of the sheath noise at the time 0535:35 SCET, as marked by an arrow in Figure 27.	108
Figure 29.	Radial density distribution of Titan's exosphere, normalized by the density of H at the exobase, N_0 [Hartle et al., 1982].	110
Figure 30.	A model for analyzing an ion beam-plasma instability. N^+ and H^+ in the corotational magnetoplasma flow with speed V_m , and electrons (hot and cold) drift with speed, V_D , the newly created ions, N^+ and H^+ , are nearly stationary.	112
Figure 31.	A plot of the growth rate, γ , versus frequency (bottom panel) and $k\lambda_D$, the wave number normalized by the Debye length versus frequency, $\lambda_D = 0.77 \text{ m}$, $N_s = 5$, $N_b = 1.5 \text{ cm}^{-3}$, $N_{ns} = N_{ps}$ and $N_e^c = 0$	114
Figure 32.	A plot of maximum growth rates, γ_{\max} , as functions of θ for the case $N_{ns} = N_{ps}$, $N_s = N_b$. The solid curve is for the case of absence of	

	cold electrons and the dashed curve is for the case $N_e^c = N_s$	116
Figure 33.	A plot of frequency for the marginal instability vs. the density ratio, N_s/N_b , for the case, $N_{ns} =$ N_{ps} , $T_e^c = T_e^h = 200$ eV. The frequency corresponding to the maximum growth rate, γ_{max} , is plotted by the dashed curve.	118
Figure 34.	The same plot as Figure 33 for the case $T_e^c =$ 2 eV.	120
Figure 35.	The plot of maximum growth rate vs. N_s/N_b in the same condition of Figure 33.	122
Figure 36.	The same plot as Figure 35 for the case $T_e^c =$ 2 eV.	124
Figure 37.	A plot of frequency for the marginal instability vs. N_s/N_b for the case $T_e^c = T_e^h = 200$ eV, $N_{ns} =$ $2 N_{ps}$	126
Figure 38.	A plot of γ_{max} vs. N_s/N_b for the case $T_e^c = T_e^h =$ 200 eV, $N_{ns} = 2 N_{ps}$	128
Figure 39.	The same plot as in Figure 37 for the case $N_{ns} =$ $0.5 N_{ps}$	130
Figure 40.	The same plot as in Figure 38 for the case $N_{ns} =$ $0.5 N_{ps}$	132
Figure 41.	A plot of the frequency for the marginal insta- bility vs. N_s/N_b for the case $T_e^c = 2$ eV, $N_e^c =$ N_s and $N_{ns} = 2 N_{ps}$	134

Figure 42.	A plot of γ_{\max} vs. N_s/N_b for the case $T_e^c = 2$ eV, $N_e^c = N_s$ and $N_{ns} = 2 N_{ps}$.	136
Figure 43.	The same plot as in Figure 41 for the case $N_{ns} =$ $0.5 N_{ps}$.	138
Figure 44.	The same plot as in Figure 42 for the case $N_{ns} =$ $0.5 N_{ps}$.	140
Figure 45.	An illustration to the ion gyrations in the sheath. Ions escaped away from the exosphere on the inbound side and were absorbed by the exosphere on the outbound side.	142
Figure 46.	The particle simulation result for the AMPTE lithium release. Plots of field energy and particle energies vs. time for $N_{Li} = N_p$, $\theta = 85^\circ$.	144
Figure 47.	Lithium ion distributions in phase space at $t =$ $300 \omega_{pe}^{-1}$, $500 \omega_{pe}^{-1}$ and $700 \omega_{pe}^{-1}$.	146
Figure 48.	Proton distributions in phase space at $300 \omega_{pe}^{-1}$, $600 \omega_{pe}^{-1}$ and $700 \omega_{pe}^{-1}$.	148
Figure 49.	Plots of field energy and particle energies vs. time for $N_{Li} = 0.11 N_p$, $\theta = 85^\circ$.	150

CHAPTER I

INTRODUCTION

One of the common and important phenomena observed in the space plasma physics experiments is the low frequency electrostatic noise associated with a gas in flowing plasma environment. For instance, during the AMPTE (Active Magnetospheric Particle Tracer Explorers) solar wind ion release experiments very intense electrostatic waves were detected on the upstream side of the gas clouds [Gurnett et al., 1985; Häusler et al., 1986], and similar waves were detected during the Voyager 1 spacecraft flyby of Titan [Gurnett et al., 1981; 1982]. In most cases the gas is fully or partially ionized by the solar ultraviolet light or some other mechanisms. It is the interaction between the newly created plasma, which is nearly stationary, and the rapidly flowing plasma that causes the waves. The purpose of this thesis is to interpret the generation of these waves by a beam plasma instability.

A linear theory for analyzing the wave instability is presented in Chapter II. For an unmagnetized plasma with many species, the electrostatic stability is determined by a reduced, one-dimensional distribution function $F(v)$, which is expressed by

$$F(v) = \sum_s \frac{m_e}{m_s} n_s F_s(v) \quad (1)$$

where m_s , n_s and $F_s(v)$ are the mass, number density and distribution function for s^{th} species, respectively, and m_e is the electron mass. If the function $F(v)$ is sufficiently double-humped to satisfy the Penrose criterion, the plasma is unstable, and therefore a wave can be generated [Krall and Trivelpiece, 1973].

Some specific examples of gas plasma interactions are analyzed in detail in Chapters III, IV and V. In Chapter III, the September 20th AMPTE solar wind lithium release is considered. The low frequency electrostatic noise on the upstream side of the lithium ion cloud is called shock-like noise because a shock is possibly associated with it [Gurnett et al., 1986a]. The properties of the shock-like noise will be compared to the theoretically calculated result. In Chapter IV a similar analysis is carried out for the December 27, 1984, AMPTE solar wind barium release, sometimes called an artificial comet. For the shock-like noise observed in the AMPTE solar wind lithium and barium releases, an interpretation was given by Gurnett et al. [1986a, 1986b]. The calculations were carried out for the case in which the waves were propagating parallel to the solar wind direction. The present analysis is more complete and systematic. The direction dependence of the wave instability will be studied. In Chapter V the noise observed during the Voyager 1 flyby of Titan's wake is considered. Titan, a moon of Saturn, is the only moon in the solar system known to

have a substantial atmosphere. At the time of Voyager 1's flyby, Titan was located within the rapidly rotating outer magnetosphere of Saturn. A broadband of low frequency electric field noise was detected by Voyager during the inbound wake crossing. This noise was called sheath noise by Gurnett et al., because it is qualitatively similar to the electrostatic wave seen in the magnetosheath at Earth and the ionosheath at Venus [Gurnett et al., 1982; Rodriguez, 1979; Scarf et al., 1980].

In Chapter VI, the results of the particle simulation for the AMPTE lithium release in the solar wind are introduced and compared with the linear theory result obtained in Chapter III.

Finally, in Chapter VII, by showing the good agreement between the theoretically calculated results and the observed data, we conclude that the beam-plasma instabilities are responsible for generating the low frequency electrostatic noises associated with gases in flowing plasma environment.

CHAPTER II

ELECTROSTATIC INSTABILITIES IN MULTICOMPONENT PLASMAS

Starting from the Vlasov equation and Poisson's equation ($\nabla^2 \phi = -4\pi\rho$), it can be shown that the linearized electrostatic wave dispersion equation for a collisionless, unmagnetized multicomponent plasma is given by

$$D(\vec{k}, \omega) = 1 + \sum_s \frac{4\pi e^2}{m_s k^2} \int \frac{d^3 \vec{v} \vec{k} \cdot \nabla_{\vec{v}} f_s(\vec{v})}{\omega - \vec{k} \cdot \vec{v}} = 0, \quad (2)$$

where m_s and $f_s(\vec{v})$ are the mass and distribution function for the s^{th} species, respectively, \vec{k} and ω are the wave vector and frequency of the wave, and e is the electronic charge [see Fried and Wong, 1966]. This equation assumes that all particles are singly charged.

If we choose the coordinates in such a way that \vec{k} is in the z -direction, then the dispersion equation (2) can be written as

$$D(k, \omega) = 1 + \sum_s \frac{4\pi e^2}{m_s k^2} \int \frac{\frac{\partial}{\partial v_z} F_s(v_z)}{\frac{\omega}{k} - v_z} dv_z = 0, \quad (3)$$

where $F_s(v_z)$ is the one-dimensional distribution function for the species s . Furthermore, we can rewrite equation (3) as

$$D(k, \omega) = 1 + \frac{\omega_e^2}{k^2} \int \frac{\frac{\partial}{\partial v} F(v)}{\frac{\omega}{k} - v} dv = 0 \quad , \quad (4)$$

and

$$F(v) = \sum_s \frac{m_e}{m_s} n_s F_s(v) \quad , \quad (5)$$

where m_e and ω_e are the electron mass and electron plasma frequency, respectively, and the subscript z is dropped for simplicity. It can be shown that the stability of the plasma is determined by the function $F(v)$. If the function $F(v)$ is sufficiently double-humped, for example, when a beam is present, the plasma is unstable and exponentially growing waves are generated [Krall and Trivelpiece, 1973].

Fried and Wong [1966] studied the ion beam-plasma instability in detail for the case of a Maxwellian velocity distribution. For the Maxwellian distributions the velocity distribution function is given by

$$f_s(\vec{v}) = \frac{n_s}{\pi^{3/2} a_s^3} \exp [-(\vec{v} - \vec{V}_s)^2 / a_s^2] \quad , \quad (6)$$

where $a_s = \sqrt{\frac{2k_B T_s}{m_s}}$ is the thermal speed, \vec{V}_s is the drift velocity, k_B is the Boltzmann constant and T_s is the temperature. For this distribution function, the dispersion equation can be shown to be

$$D(k, \omega) = 1 - \frac{1}{2} \sum_s \frac{1}{(k \lambda_{Ds})^2} Z'(z_s) = 0 \quad , \quad (7)$$

where λ_{Ds} is the Debye length for the s^{th} species, Z' is the derivative of the plasma dispersion function [Fried and Conte, 1961] with the argument

$$z_s = \frac{\frac{\omega}{k} - V_s}{a_s} \quad , \quad (8)$$

where $V_s = |\vec{V}_s| \cos \theta_s$ is the projection of the drift velocity \vec{V}_s onto the \vec{k} direction, and θ_s is the angle between \vec{V}_s and \vec{k} .

To solve the dispersion equation (7), one should properly evaluate the function $Z(z)$. If $|z|$ is small, one can use the power series expansion,

$$Z(z) = i\pi^{1/2} \exp(-z^2) - z \sum_{n=0}^{\infty} (-z^2)^n / (n + \frac{1}{2})! \quad . \quad (9)$$

For larger $|z|$, one can use the asymptotic expansion,

$$Z(z) \doteq i\pi^{1/2} \sigma \exp(-z^2) - \sum_{n=0}^{\infty} z^{-(2n+1)} (n - \frac{1}{2})! \quad , \quad (10)$$

where

$$\sigma = \begin{array}{ll} 0, & \text{for } \text{Im}z > 0 \\ 1, & \text{for } \text{Im}z = 0 \\ 2, & \text{for } \text{Im}z < 0 \end{array} \quad , \quad (11)$$

Some less elementary methods are needed for some regions of the complex z plane. The continued fraction method works well for the argument z off the real axis [Fried and Conte, 1961]. H. E. Salzer [1951] and others developed a general method to evaluate the error function with complex variable, by which the $Z(z)$ function can be expressed. There is one set of formulae, which works particularly well for the z near the real axis. These formulae are

$$\begin{aligned} Z(z) &= i\pi^{1/2} \exp(-z^2) \left(1 + \frac{2}{\sqrt{\pi}} \int_0^{iz} e^{-t^2} dt \right) \\ &= i\pi^{1/2} \exp(-z^2) + 2i \exp[(iz)^2] \int_0^{iz} e^{-t^2} dt \\ &= i\pi^{1/2} \exp(-z^2) + 2i(A + iB) \quad , \end{aligned} \quad (12)$$

where

$$\begin{aligned}
 A = & \pi^{-1/2} e^{x^2} [\pi(24Y)^{-1} \sin(2XY) - e^{-Y^2} \sin(2XY) \{ \frac{1}{2}Y \\
 & + \sum n^{-1} \exp(-\frac{n^2}{4}) \sinh(nY) \}] \\
 & + \pi^{1/2} e^{x^2} \sum_{n=1}^{24} [(n^2\pi^2 - 144Y^2)^{-1} \exp(-\frac{n^2\pi^2}{144}) \{ n\pi \\
 & \sin(\frac{1}{6}n\pi X) - 12Y \sin(2XY) \}] \quad , \quad (13)
 \end{aligned}$$

$$\begin{aligned}
 B = & \pi^{-1/2} e^{x^2} [\pi(24Y)^{-1} \{1 - \cos(2XY)\} + e^{-Y^2} \cos(2XY) \cdot \\
 & \{ \frac{1}{2}Y + \sum n^{-1} \exp(-\frac{n^2}{4}) \sinh(nY) \} \\
 & + 12\pi^{1/2} e^{x^2} \sum_{n=1}^{24} (n^2\pi^2 - 144Y^2)^{-1} \exp(-\frac{n^2\pi^2}{144}) \{ \cos(2XY) - \\
 & \cos(\frac{1}{6}n\pi X) \} \quad , \quad (14)
 \end{aligned}$$

$$X = \operatorname{Re}(iz) \quad , \quad Y = \operatorname{Im}(iz) \quad . \quad (15)$$

Therefore, for better results, we will choose different methods for the different regions of the z -plane, as shown in Figure 1. The power series is used in the region I, Salzer's method is used in

region II, the continued fraction method is used in region III, and the asymptotic expansion in region IV.

The dispersion equation can be solved numerically by the Muller's method [Muller, 1956]. The complex solution for ω is expected for a given real k . In other words, we have

$$\omega = 2\pi f + i\gamma, \quad (16)$$

where f is the frequency of the wave, and γ is the growth rate.

Positive growth rates produce exponentially growing waves.

As has been mentioned before, the dispersion equation (2) is valid for an unmagnetized plasma. In general, if there is a magnetic field, the Harris dispersion should be used [Harris, 1959]. However, if the frequency of the wave is much greater than the ion cyclotron frequency, the magnetic field does not affect the ion motion because the ions move essentially in straight lines. For the electrons, more care must be taken because in many cases the electron cyclotron frequency is comparable to the frequency of the wave. However, if the wavelength is very short, much less than the electron cyclotron radius then the wave motion is essentially not affected by the magnetic field. This result was proven by K. N. Stepanov [1959].

The magnetic field has another effect on the velocity distribution function of the plasma. Since the exact distribution is often unknown, the Maxwellian (or drifted Maxwellian) distribution is often

assumed in the theoretical modelling. This assumption is usually good for an unmagnetized plasma or even for the plasma with magnetic field, but without an external electric field. For the latter case, the distribution function may be anisotropic, but the one-dimensional distribution can still be approximated by a Maxwellian. However, if both electric and magnetic fields are present, a ring distribution is formed instead of a single-peaked Maxwellian. The type of distribution function that occurs depends on the particle gyroradius, R_c , and the scale length (size) of the plasma, L . If R_c is greater than L , a ring distribution can not be formed. If R_c is much less than L , or the plasma is nearly uniform, then a ring distribution may occur. Whether a ring distribution occurs depends on the drift velocity, V_o , which is given by cE/B , and the thermal speed of the particles, a_s . A ring distribution can be formed only if the drift velocity is greater than the particle's thermal speed, $V_o > a_s$.

In the later analysis, we will ignore the magnetic field for simplicity and check the consistencies or make some comments afterwards.

CHAPTER III

THE SHOCK-LIKE NOISE ASSOCIATED WITH THE AMPTE

SOLAR WIND LITHIUM RELEASES

3.1 Summary of Observations

As the first example, we will study the shock-like noise observed during the AMPTE solar wind lithium releases. Two lithium gas releases were performed in the solar wind upstream of the earth's bow shock [Haerendel et al., 1985b], the first on September 11th and the second on September 20th. The September 20th event is taken to be a representative example.

A summary of the plasma density, magnetic field and electric field data for the September 20th event is shown in Figure 2. The top panel shows the plasma density obtained from the analysis of electron plasma oscillations observed by the plasma wave instrument [Anderson et al., 1985]. The second panel shows the magnetic field from the magnetometer [Lühr et al., 1986]. The third panel shows the electric field spectrum from the wideband receiver. The bottom panel shows the electric field intensities from the 16-channel plasma wave spectrum analyzer [Gurnett et al., 1986a]. The lithium gas was injected into the solar wind at the time 0956:02 UT after which it was ionized by solar ultraviolet light with a time constant of about 1 hour. About 0.2 seconds after the injection the plasma density jumped up to about

10^5 cm^{-3} in the place where the spacecraft IRM (Ion Release Module) was located. At the same time, the magnetic field dropped from about 8 nT to nearly zero. The region of zero field is called the diamagnetic cavity. The IRM spacecraft stayed in the diamagnetic cavity for about 7 seconds. Due to the momentum exchange between the solar wind and the gas cloud, the entire cloud was starting to move approximately downstream a few seconds after the injection. Equivalently, the IRM spacecraft moved through the cloud toward the upstream direction. After moving out of the diamagnetic cavity the IRM went into a so-called compressed region where there was an enhanced plasma density and strong magnetic field. About 17 seconds after the injection, the spacecraft encountered a very intense electric field noise, i.e., the shock-like noise. Because no corresponding magnetic field component was detected with the search coil magnetometer, this noise is known to be electrostatic. This region, where the magnetic field was returning to the pre-event value, was located upstream (sunward side) of the lithium ion cloud. The plasma density profile in this region is shown in Figure 2. The dashed line indicates considerable uncertainty in the plasma density [see Anderson et al., 1985].

The straight line in the top panel of Figure 2 indicates the solar wind proton density level, which is about 8 cm^{-3} . As shown in Figure 2, the intense shock-like noise occurs in the region where the lithium ion density is comparable to the solar wind proton density.

A spectrum of the electrostatic noise at the time 0956:19.53 UT for the September 20th event is shown in Figure 3. Two types of

spectrum are shown, labelled peak and average. The peak is the maximum electric field spectral density detected over 1.0-second interval, and the average is the electric field spectral density averaged over a 50-msec interval. The peak and average broadband field strengths, integrated from 31 Hz to 178 kHz, are 40.4 and 6.6 mV/m, respectively. These intensities are among the most intense recorded by a space plasma wave experiments. The power of the noise is mainly contained in a frequency range from a few tens of Hz up to a few kHz. Above a few kHz, the intensity drops very rapidly to near the instrument noise level. The large difference between the peak and average spectrum in Figure 3 indicates that the noise is very impulsive, consisting of many short bursts lasting only a fraction of a second.

No evidence for spin modulation is observed. This indicates that the electric field, and therefore the wave propagating direction, tends to be distributed over a broad range of angles.

The magnetic field in the compression region is up to about 45 nT, and in the region where the shock-like noise occurs is about 10 nT. The magnetic field is approximately perpendicular to the solar wind direction.

The solar wind velocity, V_{sw} , at the time of the September 20th release is known to be about 460 km/sec [Paschmann et al., 1986]. In addition to the parameters shown in Figure 2, some information about other parameters is necessary for the wave analysis. The temperature of solar wind protons, T_p , is known to be about 10^5 K [Coates et al., 1986]. The drift velocity of lithium ions is nearly zero in the

the spacecraft reference frame, and the lithium ion temperature is very low, not more than 2000°K [Haerendel et al., 1985b]. The temperature of the electrons associated with the solar wind is about $5 \times 10^5^{\circ}\text{K}$ [Paschmann et al., 1986], and there could be some relatively cold electrons associated with the photoionization.

3.2 Instability Analysis

The intense electrostatic noise which occurred near the upstream edge of the lithium ion cloud is believed to be caused by the interaction between the solar wind and the plasma formed by the photoionization of the released lithium gas. The protons in the solar wind stream (like a beam) through the ion cloud. The exact process involved in this multi-component plasma could be very complicated. However, for the purpose of investigating the generation of the shock-like noise, a simplified model, shown in Figure 4, is used. We assume that each species has a Maxwellian (or drifted Maxwellian) velocity distribution. The lithium ion temperature, T_{Li}^+ , is taken to be 2000°K . The drift velocity of the lithium ions is zero. The proton temperature is taken to be 10^5°K , and the drift velocity of protons is equal to the solar wind velocity, $V_{\text{sw}} = 460 \text{ km/sec}$. Because of the lack of information about the electron temperature, we assume that there are two groups of electrons, hot electrons associated with the solar wind protons and cold electrons associated with the photoionization of the lithium gas. The temperature of the hot electrons, T_{e}^{h} , is equal to the solar wind electron temperature, which is $5 \times 10^5^{\circ}\text{K}$.

It is likely that the cold electron temperature is on the order of 10^4 °K, which is comparable to the characteristic energy, a few eV, of the solar ultraviolet spectrum. We adopt the value, $T_e^C = 5 \times 10^4$ °K for the cold electron temperature. Two extreme situations can be considered for the electrons. The first, corresponding to the early phase of the ion cloud expansion, is that the cold electron density is equal to the lithium ion density, $N_e^C = N_{Li}^+$. The second, possibly close to the real case in the later phase of the cloud expansion, is that the cold electron density is zero. The two groups of electrons are assumed to drift with the same velocity, which is constrained by the net current. As a first approximation, we can assume that the net current is zero. Later on, we will discuss the possible current effect on the wave analysis. If the net current is zero, from the macroscopic charge neutrality one can show

$$\vec{V}_D = \frac{N_P}{N_P + N_{Li}^+} \vec{V}_{sw} \quad , \quad (17)$$

where \vec{V}_D is the drift velocity of electrons.

First, we consider the case of the wave vector, \vec{k} , parallel to the beam velocity, \vec{V}_{sw} . As shown in Figure 4, there are two possible instabilities, one with phase velocities $0 < \omega/k < V_D$, and the other with phase velocities $V_D < \omega/k < V_{sw}$. For parallel propagation, the growth rate computations show that the instability with the phase

velocities between 0 and V_D is the most important one. The reason is that the lithium ion temperature, $T_{Li^+} = 2 \times 10^3 K$, is much lower than the proton temperature, $T_p = 1 \times 10^5 K$, and therefore the double hump associated with the lithium ions and electrons is more pronounced than the double hump associated with the electrons and protons. The instability with phase velocities between V_D and V_{sw} only occurs for proton temperatures less than $3 \times 10^4 K$. Since the measured proton temperature is $1 \times 10^5 K$, this instability never occurs.

For the instability with phase velocities between 0 and V_D , a representative growth rate computation is shown in Figure 5. The top panel shows $k\lambda_D$, the wave number normalized by the Debye length of the entire plasma, as a function of frequency, and the bottom panel shows the growth rate, γ , as a function of frequency. In these plots, the densities of protons and lithium ions are assumed to be equal, i.e., $N_{Li^+} = N_p = 8 \text{ cm}^{-3}$. The solid curves are for the case $N_e^c = 0$, and the dashed curves are for the case $N_e^c = N_{Li^+}$. Both cases give high growth rates, up to 25 sec^{-1} and 72 sec^{-1} . The frequency range is up to about 250 Hz. This range of frequencies is in good agreement with the spectra in Figure 3, which shows that the most intense noise occurs at the frequencies from a few tens of Hz up to a few hundred Hz.

Next, let us discuss the effect of the magnetic field. Taking the magnetic field to be 10 nT, we can estimate the proton cyclotron frequency, which is about 0.15 Hz. It is much less than the wave

frequency. The cyclotron frequency of the lithium ions is even smaller. Therefore, we can safely ignore the effect of the magnetic field on the ion motion. For the electrons, the cyclotron frequency is about 280 Hz, which is comparable to the main part of the frequency spectrum. However, even if we take the cold limit of the electron temperature, we find the electron gyroradius to be about 500 meters. From the results in Figure 5, we can take $k\lambda_D$ to be 0.1 or larger, then the wavelength λ is about 60 meters or shorter. Therefore, in general, the wavelength is much shorter than the electron gyroradius. From Stepanov's theory, which has been mentioned in Chapter II, we see that the magnetic field can be ignored.

The size of the diamagnetic cavity is estimated to be about 30 km in radius [Haerendel et al., 1985b]. The cyclotron radii of the solar wind protons and lithium are estimated by Gurnett et al. [1986a] to be about 56 km and 2500 km, respectively. Therefore, the ion cyclotron radii are larger than the size of the interaction region. For the electrons, the thermal speed is about 900 km/sec for the cold limit, which is much larger than the drift velocity. According to the discussion in Chapter II, we confirmed that the assumption for the distribution for each species is basically good.

In order to explain why the noise only occurs in a limited region near the upstream edge of the lithium ion cloud, we study the dependence of the instability on the lithium to proton density ratio, N_{Li^+}/N_p . Figures 6 and 7 show the frequency of marginal stability ($\gamma = 0$) as a function of the density ratio, N_{Li^+}/N_p . The dashed line

labelled γ_{\max} gives the frequency for the maximum growth rate. Figure 6 is for the case $N_e^c = 0$, and Figure 7 is for the case $N_e^c = N_{Li}^+$. In both cases the instability occurs over a broad range of frequency, which extends from zero up to 1 kHz. It is seen that the instability only occurs over a limited range of lithium to proton density ratio, which is from about 2.5×10^{-2} to 50. This agrees well with the spectrum in Figure 2 both in frequency range and in the location of the noise. In the far upstream side of the cloud, there are too few lithium ions to generate the noise, and in the cloud the lithium density is too high to cause the instability.

Figure 8 shows the maximum growth rates, γ_{\max} , as functions of N_{Li}^+/N_p for the two extreme cases, $N_e^c = 0$ and $N_e^c = N_{Li}^+$. The growth rate increases when cold electrons are present. For $N_e^c = 0$, γ_{\max} extends up to 25 sec^{-1} , while for $N_e^c = N_{Li}^+$, γ_{\max} extends up to 75 sec^{-1} . These growth rates are high enough to produce the observed intensities. This is easily seen from the following argument. From Figure 5 the group velocity $\partial\omega/\partial k$ is estimated to range from about 5.3 to 50 km/sec. Taking the higher limit of the group velocity ~ 50 km/sec, it takes 0.6 seconds for a wave packet to propagate through the unstable region which is estimated to have a thickness of about 30 km. For a growth rate of 25 sec^{-1} , the wave amplitude would grow by a factor of e^{15} . Waves with lower group velocities grow to even larger amplitudes.

In the above calculation, we assumed that the current in the interaction region is zero. Now we consider the effect of a finite

current. From the variation of magnetic field shown in Figure 2, we see that the magnetic field varies by $\Delta B \approx 35$ nT over a scale length $\Delta L \approx 200$ km. The scale length ΔL here is the diameter of the whole cloud estimated by taking the expansion speed of 4 km/sec [Häusler et al., 1986] and the time interval of 25 sec. The current density is estimated to be $0.14 \mu\text{A}/\text{m}^2$. For an electron density of 8 cm^{-3} , this current density produces a shift in the electron drift velocity of about 25%. For the more dense region of the cloud, the velocity shift is smaller. Figure 9 shows the effect of a $\pm 25\%$ shift in the electron drift velocity for the case $N_e^c = N_{Li^+}$. Similar results are obtained for the case $N_e^c = 0$. As can be seen the shift toward V_{sw} increases the size of the unstable region, both in frequency and in lithium to proton density ratio, and the shift toward $V = 0$ decreases the size of the unstable region. Generally, the effect of the current is quite small.

Next, we consider the wave propagating in different directions. The highest intensities should occur in the direction for which the growth rate is the highest. Figure 10 shows the maximum growth rate, γ_{\max} , maximized over k , as a function of θ for the case $T_{Li^+} = 2 \times 10^3 \text{ K}$, $T_e^h = 5 \times 10^5 \text{ K}$, $T_e^c = 5 \times 10^4 \text{ K}$, $T_p = 1 \times 10^5 \text{ K}$, $V_{sw} = 460$ km/sec, and $N_{Li^+} = N_p = 8 \text{ cm}^{-3}$. The maximum growth rate for the case $N_e^c = 0$ (the solid curve) decreases initially as θ increases from 0° to about 72° , then increases rapidly to a peak as θ increases to about 82° , and then falls abruptly as θ reaches 90° . The maximum growth rate at $\theta = 82^\circ$ is about 300 sec^{-1} , ten times higher than at $\theta = 0^\circ$.

For the case $N_e^c = N_{Li}^+$ (the dashed curve) the maximum growth rate, γ_{max} , decreases slowly as θ increases from 0° to about 76° , then γ_{max} increases to a peak value as θ reaches about 84° , and finally γ_{max} falls rapidly as θ approaches 90° . In contrast to the case of $N_e^c = 0$, the peak value γ_{max} at $\theta = 84^\circ$ for $N_e^c = N_{Li}^+$ is just as high as the γ_{max} at $\theta = 0^\circ$.

The main features of the instability for large θ are very similar to those at $\theta = 0^\circ$. Figure 11 shows the frequency dependence of k and γ for comparison with Figure 5. The upper panel shows the plot of $k\lambda_D$ versus frequency, where λ_D is again the Debye length of the plasma, and the lower panel shows the growth rate, γ , versus frequency. This plot is for the case $N_{Li}^+ = N_p = 8 \text{ cm}^{-3}$, $N_e^c = 0$ and $\theta = 82^\circ$. As can be seen from Figures 5 and 11, the curves for $k\lambda_D$ vs. f and γ vs. f are very similar, and the frequency ranges are almost identical for $\theta = 0^\circ$ and $\theta = 82^\circ$. The big difference between these two cases is that the growth rate for $\theta = 82^\circ$ is about ten times higher than the corresponding growth rate for $\theta = 0^\circ$.

Figures 12 and 13 show the frequencies for marginal stability, and the maximum growth rates, γ_{max} , as the functions of the lithium to proton density ratio, N_{Li}^+/N_p . The frequencies for which the growth rate is zero are indicated by $f_{\gamma=0}$. The frequencies for maximum growth rates are plotted in the dashed curves marked f_{max} . The maximum growth rates, γ_{max} , here are calculated by maximizing over both θ and k . Figure 12 shows the case for $N_e^c = 0$. The instability occurs

for N_{Li^+}/N_p ranging from about 2×10^{-3} to 8×10^2 . This range is much larger than that for $\theta = 0^\circ$ shown in Figure 6. The frequency range for marginal stability extends from 0 to more than 6000 Hz, which is also larger than the frequency range for $\theta = 0^\circ$. The maximum growth rate is up to 300 sec^{-1} . For a wide range of N_{Li^+}/N_p , the maximum growth rate is larger than 10 sec^{-1} . However, for $N_e^c = N_{Li^+}$, the unstable region of N_{Li^+}/N_p , the frequency range of marginal instability and the maximum growth rates, γ_{\max} , are almost the same as those for $\theta = 0^\circ$ (see Figures 7 and 13). Here the instability occurs for N_{Li^+}/N_p from about 2×10^{-3} to about 35. The frequency range is from 0 to 800 Hz. The maximum growth rate reaches about 80 sec^{-1} , slightly higher than γ_{\max} for $\theta = 0^\circ$.

As in the case $\theta = 0^\circ$, the effect of a finite current on the wave instability is very small. Therefore we will not discuss the effect of a current any further.

It is easily seen that when θ is taken to be a large angle, like 80° or more, the instability is caused essentially by the interaction between the lithium ions and the solar wind protons, instead of the interaction between the lithium ions and electrons, like the case for $\theta = 0^\circ$. Because of the higher mass of protons than of electrons, the distribution can have a more positive slope than in the electron case, and therefore it is not surprising to have a higher growth rate. However, this argument is only valid in the case in which the electron temperature is quite high; in other words, the electron distribution is very flat at the wave phase velocity. The results in Figure 12

belong to this case. If the electron temperature is not very high or some cold electrons are present, the Landau damping is very strong for such an ion wave. The growth rates are then reduced substantially. The results for $N_e^c = N_{Li}^+$ are just like this case.

So far, we have little information about the direction of the wave propagation. These two kinds of instabilities both are possible for generating the shock-like noise. Because of the high growth rates the ion-ion interaction is most likely to cause the noise in the later stage of the process, in which the electrons are heated up or the solar wind electrons replace the photoelectrons. For the early stage, it is hard to decide which mechanism is really responsible. Perhaps the two interactions occur simultaneously.

CHAPTER IV
THE SHOCK-LIKE NOISE ASSOCIATED WITH THE AMPTE
SOLAR WIND BARIUM RELEASES

4.1 Summary of Observations

The AMPTE solar wind barium release experiment, so-called artificial comet, was performed on December 27, 1984. During the artificial comet experiment, two canisters of barium were released from the IRM on the morning side of the Earth at a geocentric radial distance of about $17.2 R_E$. Figure 14 shows the plasma density profile (upper panel) obtained from the electron plasma oscillations and the magnetic field (bottom panel) strength from the magnetometer on the IRM. The canisters were exploded at 1232:01 UT. As can be seen, shortly after the explosion the plasma density jumps up to about $2 \times 10^5 \text{ cm}^{-3}$, then decays back to the ambient solar wind density over a period of about 2 minutes. The straight line in the upper panel indicates the solar wind plasma density level, which is about 8 cm^{-3} [Gurnett et al., 1985]. The magnetic field is essentially zero in the diamagnetic cavity, increases to as much as 130 nT in the compression region, and then decreases to the pre-event level, which is about 10 nT [Lühr et al., 1985].

During the artificial comet experiment, numerous plasma wave effects were detected by the instruments on the IRM spacecraft

[Gurnett et al., 1985, 1986b]. Figure 15 shows the electric field intensities from the 16-channel plasma wave spectrum analyzer. The magnetic field is shown in the bottom panel for comparison. The intense shock-like electrostatic noise occurs on the sunward boundary of the compression region. It starts at about 1234:23 UT and lasts about 1 minute. It is so intense that some channels are saturated. The plasma density profile in the region where the shock-like noise appears is not well-determined. However, it is evident that in this region the barium ion density makes a transition from higher than the solar wind proton density to lower than the solar wind proton density. In other words, the shock-like noise occurs when the barium ion density is comparable to the solar wind proton density.

Two representative spectra of the noise are shown in Figure 16. The left panel shows the spectrum at 1234:28.0 UT, and the right panel shows the spectrum at 1234:40.0 UT. Similar to the spectra in Figure 3, both peak and average spectra are shown. Most of the power of the noise is concentrated at the frequencies below a few hundred Hz. The intensity decreases rapidly at frequencies above a few hundred Hz. The broadband electric field strength at the maximum intensity integrated over all the frequency channels is about 140 mV/m, and may be higher because some of the channels are saturated [Gurnett et al., 1986b].

The other plasma quantities are basically similar to those in the solar wind lithium releases. The barium ions are very cold, with a

temperature of no more than $2 \times 10^3 \text{K}$. The solar wind proton temperature is about $1 \times 10^5 \text{K}$, and the drift velocity is about 500 km/sec. The solar wind electron temperature is about $5 \times 10^5 \text{K}$ [Haerendel et al., 1985a; Gurnett et al., 1986b; Rodgers et al., 1985].

A thin current sheet with a current density of $20 \text{ } \mu\text{A/m}^2$ occurs on the inner boundary of the compression region over a scale length of 300m [Lühr et al., 1985]. Since the scale length of the outer boundary of the compression region is of the order of the size of the diamagnetic cavity, which is about 90 km, the current density in the outer boundary of the compression region is of the order of $0.1 \text{ } \mu\text{A/m}^2$.

4.2 Instability Analysis

As in the solar wind lithium releases, it is believed that the intense shock-like noise observed during the artificial comet experiment is generated by the solar wind protons streaming through the nearly stationary plasma produced by the photoionization of the barium gas. The model for the wave instability calculation is shown in Figure 17. Since the basic features of the ion cloud are very similar for both the barium and lithium releases, we will simply assume that all species have Maxwellian (or drifted Maxwellian) distributions without further discussion. The drift velocity of barium ions is taken to be zero and the temperature, T_{Ba^+} , is taken to be $2 \times 10^3 \text{K}$. The protons drift with the solar wind velocity, $V_{\text{sw}} = 500 \text{ km/sec}$, and the proton temperature, T_p , is taken to be $1 \times 10^5 \text{K}$. We assume again that there are two groups of electrons, hot and cold. The cold

group is associated with the photoionization of barium gas. The temperature of the cold electrons is assumed to be 5×10^4 °K. The hot electrons are associated with the solar wind, whose temperature is 5×10^5 °K. These two groups of electrons are assumed to drift with the same velocity, \vec{V}_D , which can be estimated by assuming the total current density to be zero because the current effect is less important. As in the lithium release, the current density in the region where the shock-like noise occurs is on the order of $0.1 \mu\text{A}/\text{m}^2$. The current produces a shift in the electron drift velocity of less than 25%, and does not affect the wave instability calculation. Therefore, we neglect the current effect in the analysis. From the zero-current assumption and macroscopic charge neutrality, we obtain

$$\vec{V}_D = \frac{N_P}{N_P + N_{Ba^+}} \vec{V}_{sw} \quad . \quad (18)$$

For the wave propagating parallel to the solar wind direction, i.e., for the angle between \vec{k} and \vec{V}_{sw} , $\theta = 0^\circ$, the instability again occurs with the phase velocity $0 < \omega/k < V_D$. The instability is again caused by a double hump formed by the barium ions and electrons. The instability with the phase velocity $V_D < \omega/k < V_{sw}$ can not occur under the present conditions.

For waves with the phase velocities $0 < \omega/k < V_D$, Figure 18 shows a sample result of the growth rate calculation. The upper panel shows the plot of $k\lambda_D$, the wave number normalized by the Debye length,

versus the frequency and the lower panel shows the plot of γ , growth rate, versus the frequency. The conditions for these plots are that $T_{Ba^+} = 2 \times 10^3 K$, $T_p = 1 \times 10^5 K$, $T_e^h = 5 \times 10^5 K$, $T_e^c = 5 \times 10^4 K$, $V_{sw} = 500$ km/sec, $N_p = 8$ cm $^{-3}$, $N_{Ba^+} = 10 N_p$, and $N_e^c = N_{Ba^+}$. As shown in this figure, the frequency ranges up to 135 Hz, and the growth rate varies up to 10 sec $^{-1}$. A similar result can be obtained for the case $N_e^c = 0$, for which the growth rate is lower by about a factor of 2. The growth rates here are not as high as the corresponding ones in the lithium case, but we can easily show that these growth rates are still high enough to generate waves of the observed intensity. The frequency range is not as large as the spectra in Figure 16, but it does cover the part of frequency spectrum with the highest field spectral density. Taking $k\lambda_D = 0.1$, which is corresponding to the highest growth rate, we can estimate the wavelength to be about 21m. For the cold electrons, the cyclotron radius is about 500m. Therefore, the wavelength is much shorter than the electron cyclotron radius, and we can neglect the effect of the magnetic field on the wave instability.

The unstable regions for the two extreme cases are shown in Figures 19 and 20. Figure 19 shows the frequency of marginal instability, i.e., for $\gamma = 0$ as a function of N_{Ba^+}/N_p , the barium-to-proton density ratio. The unstable region is indicated. The frequency for the maximum growth rate versus N_{Ba^+}/N_p is plotted by the dashed curve

labelled γ_{\max} . This plot is for the case $N_e^c = 0$ using the same parameters mentioned before. As shown in the figure, instability occurs for frequencies ranging up to 700 Hz and N_{Ba^+}/N_p from about 2×10^{-2} to 2×10^2 . Similar results are shown in Figure 20 for the case $N_e^c = N_{Ba^+}$. In this case instability occurs for frequencies ranging up to 350 Hz and N_{Ba^+}/N_p between about 2.2×10^{-2} to 2.5×10^2 .

Figure 21 shows the maximum growth rates as the functions of barium to proton density ratio, N_{Ba^+}/N_p . The solid curve is for $N_e^c = 0$ and the dashed curve is for $N_e^c = N_{Ba^+}$. The growth rate is the highest when $N_{Ba^+}/N_p = 1$. For the case $N_e^c = N_{Ba^+}$, the growth rate extends up to 17 sec^{-1} , while for the case $N_e^c = 0$ the growth rate extends up to 7 sec^{-1} . As stated before, the growth rate is high enough to enable the wave to grow to the observed intensity for either case. Comparing with the spectra in Figure 16, it is seen that the frequency ranges in Figure 19 or Figure 20 just cover the main part of the observed spectra. These results also show that the instability occurs in a limited region where the densities of the barium ions and the protons are comparable. This explains why the shock-like noise occurs on the outer boundary of the compression region shown in Figure 14.

Again, like in the lithium case, we want to know how the instability, namely the growth rate, depends on the wave propagation direction. Figure 22 shows the plots of the maximum growth rates versus θ , the angle between \vec{k} and \vec{V}_{sw} . These plots are for the case $N_{Ba^+} = 10 N_p = 80 \text{ cm}^{-3}$, $N_e^c = 0$ (the solid curve) and the case $N_{Ba^+} =$

$10 N_p = 80 \text{ cm}^{-3}$, $N_e^c = N_{Ba}^+$ (the dashed curve). The curves here are quite similar to the curves shown in Figure 10. The maximum growth rate, γ_{\max} , for $N_e^c = 0$ decreases slowly to a minimum as θ increases from 0° to about 75° , then γ_{\max} rises rapidly to a peak as θ increases to about 85° , and then γ_{\max} falls abruptly to zero as θ approaches 90° . The peak value of γ_{\max} at $\theta = 85.5^\circ$ is about 60 sec^{-1} , which is about 17 times higher than γ_{\max} at $\theta = 0^\circ$. For the case $N_e^c = N_{Ba}^+$, γ_{\max} decreases initially as θ increases from 0° to about 80° , then γ_{\max} grows to a peak at $\theta = 86^\circ$, not as quickly as in the previous case, and then γ_{\max} falls to zero as θ approaches 90° . Unlike the case $N_e^c = 0$, the peak value of γ_{\max} at $\theta = 86^\circ$ is less than γ_{\max} at $\theta = 0^\circ$.

In Figure 23, the frequency dependence of $k\lambda_D$ and γ is illustrated for $N_{Ba}^+ = 10 N_p = 80 \text{ cm}^{-3}$, $N_e^c = 0$ at $\theta = 85.5^\circ$, which is the angle for the peak of γ_{\max} in Figure 22. The upper panel shows the plot of $k\lambda_D$ versus the frequency and the lower panel shows the plot of γ versus the frequency. The curves are similar to those shown in Figure 18 and also in Figures 5 and 11. This means that they have similar properties. However, the frequency range at $\theta = 85.5^\circ$ is slightly larger than that at $\theta = 0^\circ$, and the growth rate for the former is much higher than that for the latter.

For those large angles at which the maximum growth rates have peak values, the frequencies for the marginal instability and for the maximum growth rate are computed as functions of N_{Ba}^+/N_p . The results

are shown in Figures 24 and 25. Figure 24 shows the plots of $f_{\gamma=0}$ versus N_{Ba^+}/N_p for the case $N_e^c = 0$. It is seen that the frequency range extends up to 3000 Hz, which is higher than that for $\theta = 0^\circ$ shown in Figure 19. The barium-to-proton density ratio, N_{Ba^+}/N_p for the unstable region is between about 2×10^{-3} and 3.5×10^3 , which is much larger than that for $\theta = 0^\circ$. The maximum growth rate, γ_{max} , for a large range of N_{Ba^+}/N_p , from 5×10^{-3} to 1×10^3 , is higher than the highest value of γ_{max} for $\theta = 0^\circ$. However, for $N_e^c = N_{Ba^+}$ as shown in Figure 25, the frequency range is up to 300 Hz, which is less than that for $\theta = 0^\circ$ shown in Figure 20. N_{Ba^+}/N_p for the unstable region varies from about 3×10^{-3} to 2×10^2 . The maximum growth rate, γ_{max} , compared with the corresponding value in Figure 21, is slightly higher for $N_{Ba^+}/N_p < 1$, but slightly lower for $N_{Ba^+}/N_p > 1$.

From the above analysis, one can see that the situation for the barium release is very similar to that for the lithium releases. If there are no cold electrons, the instability at large θ occurs over a larger range of N_{Ba^+}/N_p and for higher frequencies than the instability at $\theta = 0^\circ$. While in another limit, if the cold electron density is equal to the barium ion density, the instabilities caused by the two kinds of interactions give essentially the same results. However, the results shown in Figure 24 agree with the results shown in Figures 14, 15 and 16 best. In contrast to the lithium case, one may conclude that the result for the ion-ion interaction without cold electrons is more likely to be close to the real case. During the September 20th event (lithium release) the shock-like noise was

detected 17 seconds after the injection, while during the artificial comet experiment, the shock-like noise was detected about 140 seconds after the injection. Therefore, in the latter case, the electrons are more likely to have a higher temperature. Under these conditions the ion-ion interaction is more likely to generate the noise because of the higher growth rate.

CHAPTER V

THE SHEATH NOISE OBSERVED BY VOYAGER 1 IN TITAN'S WAKE

5.1 Summary of Observations

As the third example, we will analyze the so-called sheath noise observed during the Voyager 1 spacecraft flyby of Titan on November 12, 1980.

At the time of Voyager 1's flyby, Titan was located within the outer magnetosphere of Saturn. A model described by Hartle et al. [1982], which represents the environment near Titan during the Voyager flyby, is shown in Figure 26. The Voyager 1 trajectory, projected into the Saturnian equatorial plane, is indicated. The electrostatic field, or the sheath noise, was observed in the inbound wake, shown cross-hatched in Figure 26. It has been found that Titan has no appreciable intrinsic magnetic field and therefore, its atmosphere-ionosphere interacted directly with the Saturnian magnetosphere [Ness et al., 1981].

The low frequency electric field noise intensities detected by the plasma wave spectrum analyzer are shown in the bottom panel of Figure 27. The sheath noise from 0532:30 to 0538:30 SCET, is distinct from the noise in the tail region, from 0539:30 to 0545:30 SCET. The sheath noise has a broad frequency range, from 10 to 1000 Hz. A representative spectrum of this noise, at the point marked by the

arrow in Figure 27, is shown in Figure 28. The spectrum has a broad peak centered at a frequency of about 100 to 200 Hz. Most of the power is contained in the frequency range from a few tens of Hz to a few hundred Hz. The broadband electric field strength is about 0.5 mVm^{-1} .

The upper hybrid resonance emissions observed in the vicinity of Titan have provided a plasma density profile along the trajectory of the spacecraft. The top panel of Figure 27 shows the plasma density profile. This figure was reproduced from the information in Gurnett et al. [1982]. The inbound sheath, the tail region and the outbound sheath, if there was one, are indicated. The density level of magnetospheric plasma, N^+ and H^+ , which was about 0.3 cm^{-3} , is indicated by the dashed line. As can be seen in the figure, the density is enhanced up to 40 cm^{-3} in the vicinity of Titan. Since the plasma in the wake originated mostly from the photoionization of exospheric particles, then the plasma density profile is mainly controlled by the exospheric density distribution.

Titan's exosphere has been studied in detail by Hartle et al. [1982]. The exosphere is composed mainly of molecular nitrogen, N_2 , and atomic hydrogen, H. The densities of N_2 and H are estimated to be about 10^8 cm^{-3} and $4 \times 10^4 \text{ cm}^{-3}$, respectively, at the exobase, which is 4000 km from the center of Titan (see Figure 26) [Broadfoot et al., 1981]. The temperature of the upper atmosphere was measured to be 186°K , varying by about 30°K [Smith et al., 1982]. Taking the temperature to be 160°K , Hartle et al. [1982] derived the radial density

distributions shown in Figure 29. The density scale height of N_2 was about 150 km, and that of H was about 1500 km. The scale height is about 500 km in the inbound wake, which indicates that the densities of H and N_2 must be similar in this region. However, there is no information about the fractions of H^+ and N^+ , or any other minor species, such as N_2^+ or H_2CN^+ .

As can be seen from Figure 27, the frequency of the sheath noise has a tendency to increase as Voyager 1 approached Titan. However, a clear cutoff is seen at about 0539:00 SCET, when the density is about 15 cm^{-3} to 20 cm^{-3} . The intense noise was only observed on the inbound leg, which is on the dayside of Titan, and was essentially absent on the outbound nightside leg.

The properties of the magnetospheric plasma just outside the wake region are fundamental to the magnetospheric interaction with Titan's atmosphere. It has been known from the Voyager 1 experiments that there were at least two major components, H^+ and N^+ , in the magnetosphere near the orbit of Titan. N_2^+ and H_2CN^+ were also possibly present [Hartle et al., 1982]. Neubauer et al. [1984] summarized the basic properties of the magnetospheric plasma near the orbit of Titan. The number density of protons was about 0.1 cm^{-3} , and the density of nitrogen ions, N^+ , was about 0.2 cm^{-3} . The other possible components were minor and will be ignored in the present analysis. The temperature of H^+ and N^+ ions were 210 eV and 2.9 keV, respectively. The electron number density and temperature were about 0.3 cm^{-3} and 200

eV. The plasma flow velocity was approximately in the corotational direction (20° deflected toward Saturn), with speed ranging from 80 to 150 km/sec, which is somewhat less than 200 km/sec, the corotational speed near Titan's orbit.

The average magnetic field magnitude was measured to be about 5 nT in the magnetoplasma. Neubauer et al. [1984] derived the gyroradii of each species of particles. The gyroradii of the thermal protons and thermal N^+ ions in the magnetoplasma were 413 km and 5790 km, respectively. The gyroradius of the electrons was 9.5 km. The gyroradii of the protons and newly created N^+ ions from the exosphere were 248 km and 3470 km, respectively. The magnetic field changed in both magnitude and direction in the vicinity of Titan. It varied about 4 nT over a scale length of about 4 Titan radii. From this, one can estimate that the average current density is not more than 3×10^{-10} A/m².

5.2 Instability Analysis

As shown in Figure 26 in the region just outside of the ionopause, plasma is produced from the photoionization of the exospheric particles. This plasma is essentially stationary relative to Titan, and therefore to the spacecraft because the component of the Voyager 1's velocity in the corotational direction is very small compared to the flow velocity of magnetospheric plasma. Consequently, the ions in the corotational magnetospheric plasma stream (like a beam) through a nearly stationary plasma created from the exosphere of Titan. The

known to be complicated and involves ionization, mass loading, and ion acceleration. To try to understand the origin of the plasma wave noise, a simple model will be used. A reduced (one-dimensional) velocity distribution for the model is shown in Figure 30. Six groups of particles are considered. Minor constituents are neglected. In the assumed model, each component is represented by a drifted Maxwellian velocity distribution. The drift velocity of N^+ and H^+ in the beam is the magnetospheric flow velocity, V_m , which is taken to be 150 km/sec. The drift velocity of N^+ and H^+ in the plasma is approximately zero. Since there is no information about the drift velocity of electrons, we assume that the electrons drift with a velocity between 0 and V_m , in such a way that the total current is zero. The validity of this assumption can be verified by estimating the maximum possible current effect. Since the current density is not more than 3×10^{-10} A/m², the current correction to the beam velocity is only 7 km/sec, assuming a number density of 0.3 cm^{-3} , which is not more than 10%. Using the same argument as in the AMPTE releases, the current essentially does not affect the instability analysis. Therefore, the electron drift velocity is determined by the zero current condition $\sum_i n_i e \vec{v}_i = 0$ and charge neutrality, so that

$$\vec{v}_d = \frac{N_b \vec{v}_m}{N_b + N_s} \quad (19)$$

where N_b and N_s are the total density of the ions in the beam, and the total density of the ions in the newly created plasma.

There are several other parameters which are not well known and for which reasonable assumptions are required. First of all, the electron temperature in the interaction region is unknown. It is possible that the electron temperature is similar to that in the magnetosphere, or that there is a cold component associated with the exospheric photoionization. Therefore, we assume that there are two groups of electrons, hot and cold. The hot electrons have a temperature, T_e^h , of 200 eV, which is the temperature of the magnetospheric plasma. The cold electrons are assumed to have a temperature, T_e^c , from 2 eV to 200 eV. The lower limit is estimated from the photoionization by the ultraviolet light and the higher limit is the temperature of the magnetospheric plasma. Finally the temperatures of N^+ and H^+ in the plasma are unknown. These temperatures are presumably close to the exosphere temperature which was measured to be 186°K. A summary of all parameters and their values used is listed in Table 1.

As can be seen from Figure 30, for the case of waves propagating parallel to \vec{V}_m , instabilities can in principle occur for phase velocities between 0 and V_d and between V_d and V_m . As in the AMPTE case the instability with $V_d < \omega/k < V_m$ cannot occur because the beam ion distribution is too broad to produce a double hump. Therefore, instability only occurs in association with the relatively cold exospheric ions at phase velocities between 0 and V_d .

Figure 31 shows a representative growth rate computation for the instability. The top panel shows the wave number, k , normalized by the Debye length, λ_D , as a function of frequency. The bottom panel shows the growth rate, γ , versus frequency. The parameters used here are as follows: $N_{ps} = N_{ns}$, $N_s = 5 \times N_b = 1.5 \text{ cm}^{-3}$, $T_e^c = 200 \text{ eV}$, i.e., $N_e^c = 0$, $N_e^h = N_s + N_b$, (see Table 1 for the definitions of all symbols). For the remaining parameters the values in Table 1 are used. The Debye length, λ_D , is estimated to be about 0.77 m. Taking $k\lambda_D$ to be 0.05 or larger, the wavelength is estimated to be about 20m or less. Comparing to the electron gyroradius of 9.5 km, we see that the wavelength is much shorter than the electron gyroradius. The cyclotron frequency of protons is less than 0.1 Hz and that of N^+ is even less. Since the cyclotron frequencies of the ions are much smaller than the wave frequency, we can treat the ions as unmagnetized. By the theory of Stepanov, it follows that the wave motion is basically not affected by the magnetic field.

As is shown in Figure 31, the growth rate is very high, up to 6 sec^{-1} , which means that wave disturbances can increase by a factor of a thousand in 1 second. At Voyager 1's approach, the radial distance to the center of Titan was about 6500 km. If a wave starts 1000 km upstream of the plasma flow, it takes 5 seconds (at a speed of 200 km/sec, including the wave propagation) to reach the spacecraft. During this time the wave can grow to 10^{15} times, which is more than enough to grow from a thermal level to very high amplitudes. The

frequency range, up to 200 Hz, agrees very well with the spectrum in Figure 28.

To study how the instability depends on the wave propagation direction, we plot the maximum growth rate, γ_{\max} , as functions of θ , the angle between \vec{k} and \vec{V}_m , as shown in Figure 32. The solid curve is for the case $N_e^c = 0$, and the dashed curve is for $N_e^c = N_s$. In this plot, it is assumed that $N_{ps} = N_{ns}$, $N_s = N_b$. Unlike the AMPTE case, the maximum growth rates for both $N_e^c = 0$ and $N_e^c = N_s$ decrease monotonically as θ increases, and the instability ceases at about 85° . In other words, the most unstable case is for waves propagating parallel to the beam direction. Similar results are obtained for a variety of conditions in Table 1.

It can be shown that the necessary condition for a peak growth rate other than at $\theta = 0^\circ$ is that the drift velocity of the beam ions must be larger than the thermal velocity. In this case, the thermal velocity is estimated to be about 200 km/sec, which is larger than the drift velocity of 150 km/sec. Therefore, it is not surprising that the maximum growth rate occurs at $\theta = 0^\circ$. Therefore, we will only consider the case $\theta = 0^\circ$ in the rest of the study.

As has been done in the AMPTE case, in order to study the dependence of the instability on the plasma density, the relation of the marginal instability condition ($\gamma = 0$) to the plasma-beam density ratio, N_s/N_b , must be investigated. Figures 33 and 34 show the frequency of marginal instability as a function of N_s/N_b for the case of $N_{ns} = N_{ps}$, i.e., equal densities of N^+ and protons. The dashed curves

in the figures show the frequencies for the maximum growth rates. The corresponding maximum growth rates, γ_{\max} , versus N_s/N_b are shown in Figures 35 and 36. Figures 33 and 35 are for the case $T_e^c = T_e^h = 200$ eV, or $N_e^c = 0$, $N_e^h = N_s + N_b$, while Figures 34 and 36 are for the case $T_e^c = 2$ eV, $T_e^h = 200$ eV, $N_e^c = N_s$, and $N_e^h = N_b$. The parameters which are not mentioned here are given in Table 1. These two groups of figures cover the two extreme cases for the electron temperatures. The two extremes give very similar results. For the case $N_e^c = 0$, the maximum growth rate reaches about 11 sec^{-1} . The frequency ranges from 0 to about 650 Hz, and N_s/N_b for the unstable region varies from about 0.001 to 50. For the case $T_e^c = 2$ eV, $N_e^c = N_s$, the maximum growth rate reaches about 14 sec^{-1} . The frequency ranges from 0 to about 400 Hz, and N_s/N_b for the unstable region is from 0.001 to about 25.

This result shows that the instability cannot occur far from Titan where the newly created plasma density is too low or close to Titan where the newly created plasma density is too high. As can be seen from Figure 27, the sheath noise started about six minutes before Voyager 1's closest approach to Titan where the exospheric plasma density is less than the magnetoplasma density. When the exospheric plasma density is about 50 times higher than the magnetoplasma density, the noise ceased. Along with the frequency range, we see that the theoretical and the observed results are in very good agreement.

Since the composition of the newly created plasma is not well known, the density of nitrogen ions, N_{ns} , could be either higher

or lower than the density of protons, N_{ps} . To study the effect of the composition on the instability, plots similar to Figures 33 and 36 have been done. Figures 37 and 38 show the frequency for the marginal instability and γ_{max} as functions of N_s/N_b for the case $N_e^c = 0$ and $N_{ns} = 2 N_{ps}$. Figures 39 and 40 show the same plots for the case $N_{ns} = 0.5 N_{ps}$. From these figures, we see that the unstable frequency range for $N_{ns} = 2 N_{ps}$ is smaller than that for $N_{ns} = 0.5 N_{ps}$. The former is about 600 Hz, and the latter is about 800 Hz. The growth rate for $N_{ns} = 2 N_{ps}$ is also slightly less than that for $N_{ns} = 0.5 N_{ps}$. Similar features are also found for the case $T_e^c = 2$ eV, $N_e^c = N_s$. Figures 41 and 42 show the case $N_{ns} = 2 N_{ps}$. The frequency range is about 300 Hz and the growth rate is up to about 12 sec^{-1} . Figures 43 and 44 show the case $N_{ns} = 0.5 N_{ps}$. The frequency range is about 400 Hz and the growth rate is about 15 sec^{-1} . Therefore, although the different composition of the newly created plasma gives basically similar results for the instability analysis, it is slightly more unstable if more protons are present.

There was no sheath noise observed in the outbound wake. This is believed to be due to the low density of the newly created plasma, which is not sufficient to cause the instability. As shown in Figure 27, the plasma density fell to the magnetoplasma level after 0545:30 UT. There are two reasons for this inbound-outbound asymmetry. The first reason is the day-night asymmetry. The outbound wake is on the nightside. There is less photoionization than in the inbound wake, which is on the dayside. The second reason is the direction of

acceleration of the newly created ions. As is shown in Figure 45, on the inbound side of Titan the ions are accelerated away from the exosphere and therefore escape downstream. This causes a density enhancement. However, on the outbound side of Titan, the ions are accelerated into the exosphere and are absorbed (see Gurnett et al., [1982] and Bridge et al. [1981]).

As mentioned in Chapter II, when the gyroradius is comparable to the scale size of the system, the assumption of a Maxwellian distribution for each species of particles may be questionable. In the present case, the magnetic field is roughly perpendicular to Titan's equatorial plane, and the electric field, which is induced by the corotational motion of the Saturnian magnetosphere, is approximately in Titan's equatorial plane and perpendicular to the flow direction, as shown in Figure 45. Since the drift velocity of the beam ions is about 150 km/sec, it is less than the thermal velocity of the beam ions, which is about 200 km/sec. The thermal velocity of the electrons is about 850 km/sec (for $T_e^c = 2$ eV) to 8500 km/sec (for $T_e^h = 200$ eV), which is much higher than the drift velocity. Therefore, for the electrons and the beam ions, it is impossible to form a ring distribution. For these species, a Maxwellian (or a drifted Maxwellian) distribution is a good assumption for each of them. Since the exospheric ions are very cold, the important thing is their gyroradii. The gyroradius of the newly created exospheric H^+ is 248 km and that of N^+ is 3470 km. The scale length of the interaction

region, L , can be taken as the scale length of the exosphere, which is about 2000 km (see Figure 29). The gyroradii of these ions are comparable to the scale length, L . Therefore, the assumption of a Maxwellian distribution may not be very good. However, since it is not sufficient to form a ring distribution, the deviation from a Maxwellian probably does not change the basic characteristics of the wave instability.

CHAPTER VI

COMPARISON WITH THE PLASMA SIMULATION RESULT

In the preceding chapters, the analysis is based on the linear theory, which is valid for small amplitude waves near the very beginning of the wave growth. For a fast-growing wave nonlinear effects will quickly appear. To fully understand the waves that we analyze in this paper, it is useful to compare the linear theory with the plasma simulation result. In this chapter, a simulation result for the AMPTE lithium release is described and compared with the linear theory result in Chapter III. The simulation was done in collaboration with UCLA [Omidi et al., 1986].

In the plasma simulation for the AMPTE lithium release, a one-dimensional electrostatic code is used. All ions and electrons are treated as particles. The system contains totally 10^5 particles, with 5×10^4 electrons and 5×10^4 ions. The size of the simulation dimension is chosen to be 32 times the electron Debye length, in which there are 64 grid points. The boundary condition is periodic and the time step is $0.2 \omega_{pe}^{-1}$. All other parameters, such as temperatures, drift velocities, etc., for the particles are the same as those in Chapter III. Some crucial results of the simulation are shown in Figures 46 to 49. In the plots in Figures 46 to 48, it is assumed that $N_{Li}^+ = N_p$ and that the angle between \vec{k} and \vec{V}_{sw} is 85° . No

photoelectrons are present. All particles are uniformly distributed in the simulation box. The initial velocity distribution is a drifting Maxwellian.

Figure 46 shows the energy changes of the particles and field as a function of time. The scale for each energy is normalized to the initial total energy, and the time is in the unit of ω_{pe}^{-1} . The top panel shows the electric field energy. The second, third, and bottom panels show the electron energy, proton energy and lithium ion energy, respectively. As seen from the figure, the electric field energy starts from a thermal noise level and increases rapidly to a maximum intensity at a time of about $550 \omega_{pe}^{-1}$. This means that the plasma is unstable and that the particle energy is rapidly transferred to field energy. This is exactly the same instability mechanism described in Chapter III. Later on, the field energy decreases gradually and is transferred back to the particle energy, and then the particles are heated up. This effect can be seen more clearly in Figures 47 and 48, which show the lithium and proton distributions in phase space at different times. As can be seen from Figure 47, at $t = 300 \omega_{pe}^{-1}$, the lithium ion distribution is only slightly modified by the waves. However, the wave amplitude is not large, and the instability is in the linear growth stage. At $t = 500 \omega_{pe}^{-1}$, we can see that the wave amplitude is very large. Some particles gain velocities higher than $5 V_{Li}$, where V_{Li} is the initial thermal velocity of lithium ions. Further, at $t = 700 \omega_{pe}^{-1}$, the wave is distorted and some particles have become trapped. Eventually the lithium ions are thermalized.

The evolution of the proton distribution is shown in Figure 48. At $t = 300 \omega_{pe}^{-1}$, shown in the top panel, we see the linear growing waves. The middle panel shows the nonlinear stage of the wave-particle interaction. At $t = 600 \omega_{pe}^{-1}$, the protons become trapped and the waves are saturated. Finally at $t = 700 \omega_{pe}^{-1}$, more trapping is shown, the beam is broadened and the system is stabilized. A similar result for $N_{Li}^+ = 0.11 N_p$ is shown in Figure 49. In this case, the field energy changes slower than that in Figure 46 for the case $N_{Li}^+ = N_p$. This agrees with the result in Chapter III, in which we show that the highest instability occurs as $N_{Li}^+ = N_p$. It is difficult to compare the spectra directly because the ion to electron mass ratio differs from the real case. However, it is clear that the simulation result is consistent with the linear theory.

The simulation also shows that in the absence of cold electrons, the instability for $\theta = 0$ is much less than that for $\theta = 85^\circ$ and that introducing the cold electrons makes the former increase and the latter decrease. This trend agrees with the linear theory result.

N. Omid [1986, personal communication] recently put the magnetic field in various directions in the simulation and found that there is no appreciable change to the result. This confirms the reliability of our linear theory result.

There are a few things about the simulation to be discussed. First of all, the condition for the simulation is slightly different from the actual experiment. Especially, in the simulation, the beam

is only introduced initially while in the actual case, the "fresh" beam is continuously supplied. This may not make a big difference to the very beginning of the wave generation, but it does make a considerable difference to the wave saturation level. We expect that stabilization in the actual case is not as fast as in the simulation. Also, some actual phenomena may not be seen by the simulation. Second, by using the actual ion to electron mass ratio, we may calculate the growth rates and frequency spectra, and be better able to compare the theoretical result with the observed result. This is a subject for further study.

CHAPTER VII

CONCLUSIONS

The occurrence of intense electrostatic noise during interaction between a neutral gas and a rapidly flowing plasma is a common phenomenon. The generation of such noise is interpreted by a model based upon the ion beam-plasma instability caused by interaction of a moving plasma with a nearly stationary plasma produced by the ionization of the neutral gas. For some well-known examples, such as the shock-like noise associated with the AMPTE solar wind lithium and barium releases and the so-called sheath noise associated with the Titan's wake, a detailed analysis has been carried out in this thesis. The results of the calculation agree very well with the observed results.

In the case of the AMPTE solar wind ion (lithium and barium) releases, the shock-like noise is interpreted as being generated by an interaction of the streaming solar wind protons and the nearly stationary lithium or barium gas cloud. The instability is a combination of an electron-ion interaction and an ion-ion interaction. The type of interaction depends on the angle between the wave propagating direction and the solar wind direction. This angle, θ , governs the wave growth rate and determines whether the ion-electron interaction or the ion-ion interaction is predominant. There are two maxima in a

plot of wave growth rate as a function of θ . One occurs at $\theta = 0^\circ$, and another occurs at θ greater than about 80° . The instability corresponding to the former is basically caused by the interaction between the lithium or barium ions and electrons, and the instability corresponding to the latter by the interaction between the lithium or barium ions and the solar wind protons. The calculations show that both types of instabilities give high growth rates and frequencies in the observed range. The calculations also show that the noise can only occur when the density of the solar wind protons is comparable to the density of the lithium or barium ions. This explains why the noise is only observed near the upstream edge of the gas cloud. The growth rates for the two types of instabilities depend somewhat on the presence of cold electrons. In the absence of cold electrons, the growth rate for the ion-ion interaction is much higher (an order of magnitude) than that for the ion-electron interaction. However, in another limit, if the cold electron density is equal to the lithium or barium ion density, the growth rate for the ion-ion interaction is the same as or even less than that for the ion-electron interaction. Because of the lack of the information about cold electrons and the wave propagating direction, it is difficult to determine which instability is really responsible for the noise generation. However, it is likely that in the early stage of the gas cloud evolution, the ion-electron interaction is a better candidate because of the presence of a large number of photoelectrons, while in the later stage, after the

electrons are heated up, the ion-ion interaction may be a better candidate because of the high growth rate. The linear theory results have been confirmed by computer particle simulations.

Unlike the AMPTE case, the analysis of the noise associated with Titan's wake shows that the most unstable direction is parallel to the plasma flow. There is no secondary ion-ion peak at a large angle between the wave propagating direction and the flowing plasma direction. The basic reason for this result is that in order to have two maxima for the growth rate, the beam drift velocity has to be greater than the beam thermal velocity. In the Saturnian magnetosphere the temperature of the flowing plasma is so high that the thermal velocity is greater than the drift velocity. We expect that the wave is propagating in the flowing direction because of the highest growth rate. The calculation shows that the frequency range of the wave instability agrees with the frequency range of the observed noise, and that the growth rate is adequate to generate the noise at the observed level. Moreover, the instability only occurs in a limited range for the plasma to beam density ratio, N_g/N_b , from about 0.001 to 50. This explains why the noise only occurs in the inbound wake.

Many similarities exist in the various cases of the interactions between neutral gas and rapidly moving plasma, such as the noise pattern, frequency range, etc. The analysis presented in this thesis can be applied to many other cases for the electrostatic noise

interpretation. For example, a similar kind of wave turbulence was observed in the vicinity of the space shuttle [Shawhan and Murphy, 1983], during ICE encounter with the Comet Giacobini-Zinner and during Comet Halley observations [Scarf et al., 1985; Mendis and Tsurutani, 1986]. In those cases, although the gas composition may be different, and the drift velocities and the temperatures may widely vary, the same basic mechanism is applicable. Since the magnetic field strength varies enormously from case to case, special attention needs to be given to the effect of the magnetic field. In one situation, we may neglect the magnetic field for simplicity, but in another, we may have to include the magnetic field. Careful examination is necessary.

Table 1. Parameters used for the analysis of the sheath
noise in Titan's wake.

TABLE 1.

Quantities	Notations	Values
H ⁺ density in beam	N_{pb}	0.1 cm^{-3}
N ⁺ density in beam	N_{nb}	0.2 cm^{-3}
Total density in beam	$N_b (= N_{pb} + N_{nb})$	0.3 cm^{-3}
Newly created H ⁺ density	N_{ps}	Variable
Newly created N ⁺ density	N_{ns}	Variable
Total newly created density	$N_s (= N_{ps} + N_{ns})$	Variable
H ⁺ temperature in beam	T_{pb}	210 eV
N ⁺ temperature in beam	T_{nb}	2.9 keV
Exospheric H ⁺ temperature	T_{ps}	186°K
Exospheric N ⁺ temperature	T_{ns}	186°K
Hot electron temperature	T_e^h	200 eV
Cold electron temperature	T_e^c	2 eV ~ 200 eV
Beam velocity	V_m	150 km/sec
Electron drift velocity	V_d	Variable
Cold electron density	N_e^c	Variable
Hot electron density	N_e^h	Variable

Figure 1. A sketch map of complex z -plane for evaluating the plasma dispersion function, $Z(z)$. The power series expansion is used in region I, Salzer's method in region II, continued fraction in region III, and asymptotic expansion in region IV.

A-G86-61

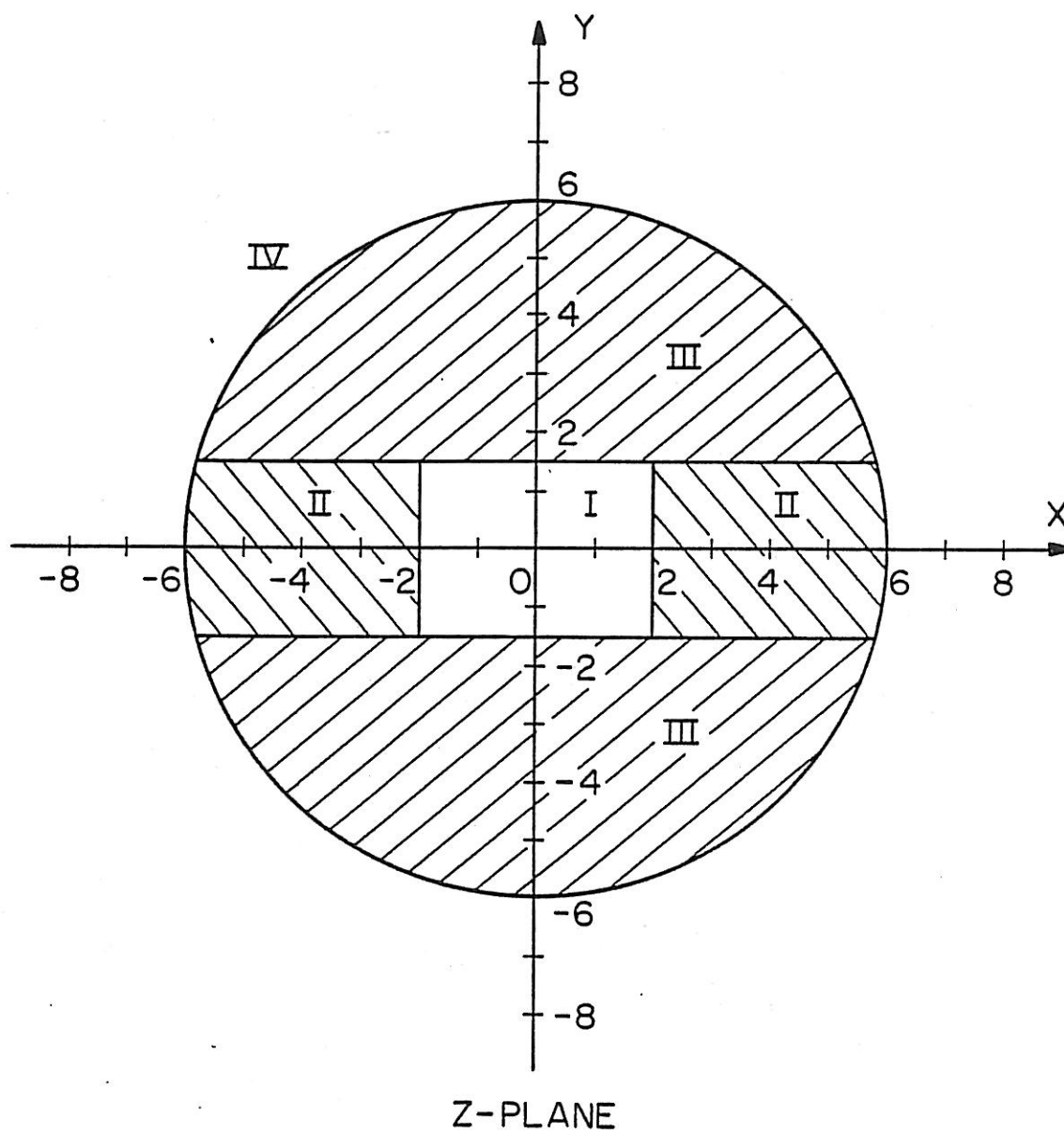


Figure 1

Figure 2. A summary of the plasma density, magnetic field, and electric field observations for the AMPTE solar wind lithium release on September 20, 1984. The intense burst of electrostatic noise occurred in the region where the lithium ion density, N_{Li}^+ , is comparable to the solar wind proton density, N_p .

D-G84-1476-3

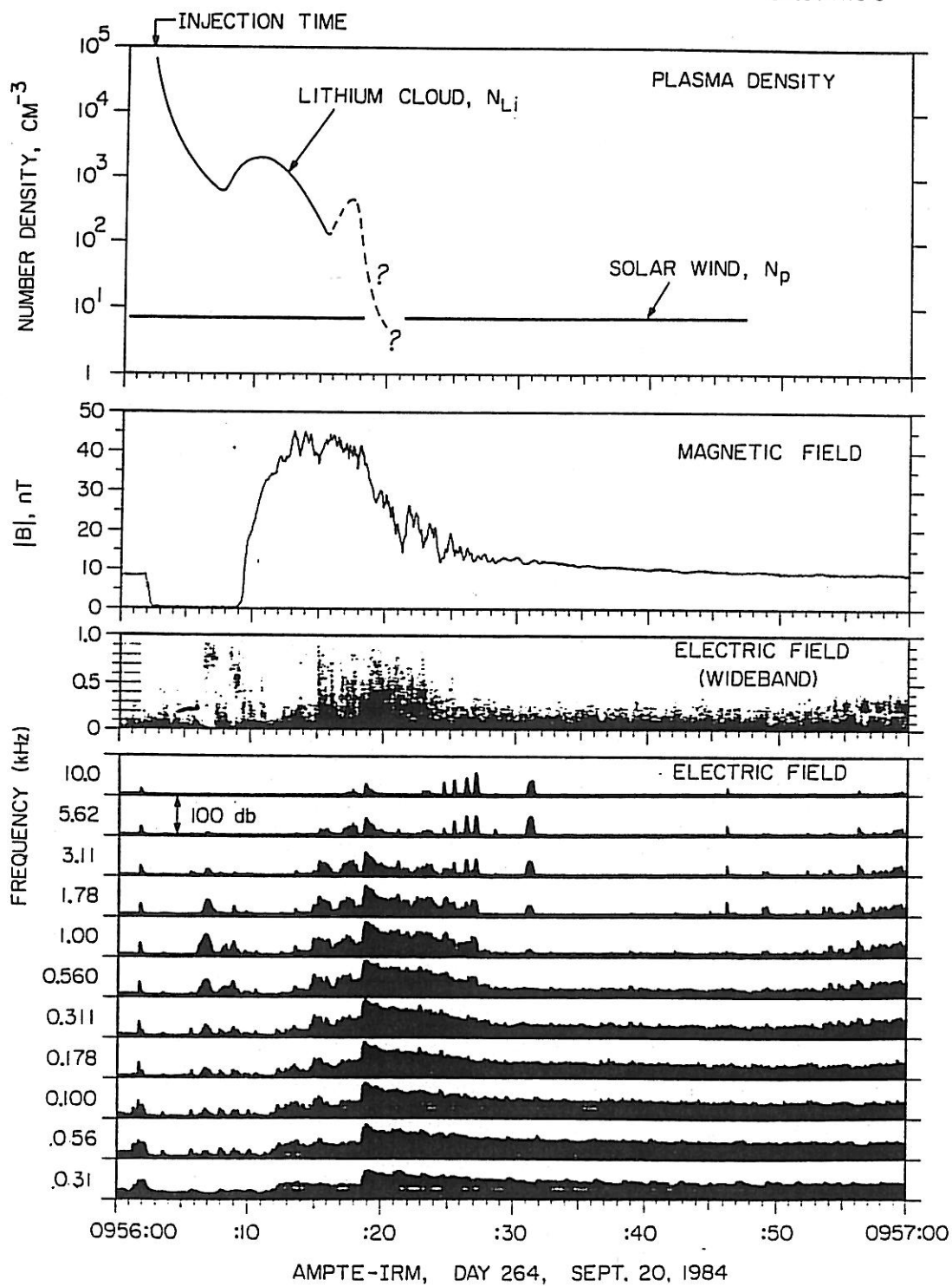


Figure 2

Figure 3. The peak and average electric field spectrums at 0956:19.53 UT on September 20, 1984. The main power of the noise is within frequencies below 1 kHz.

C-G84-1319

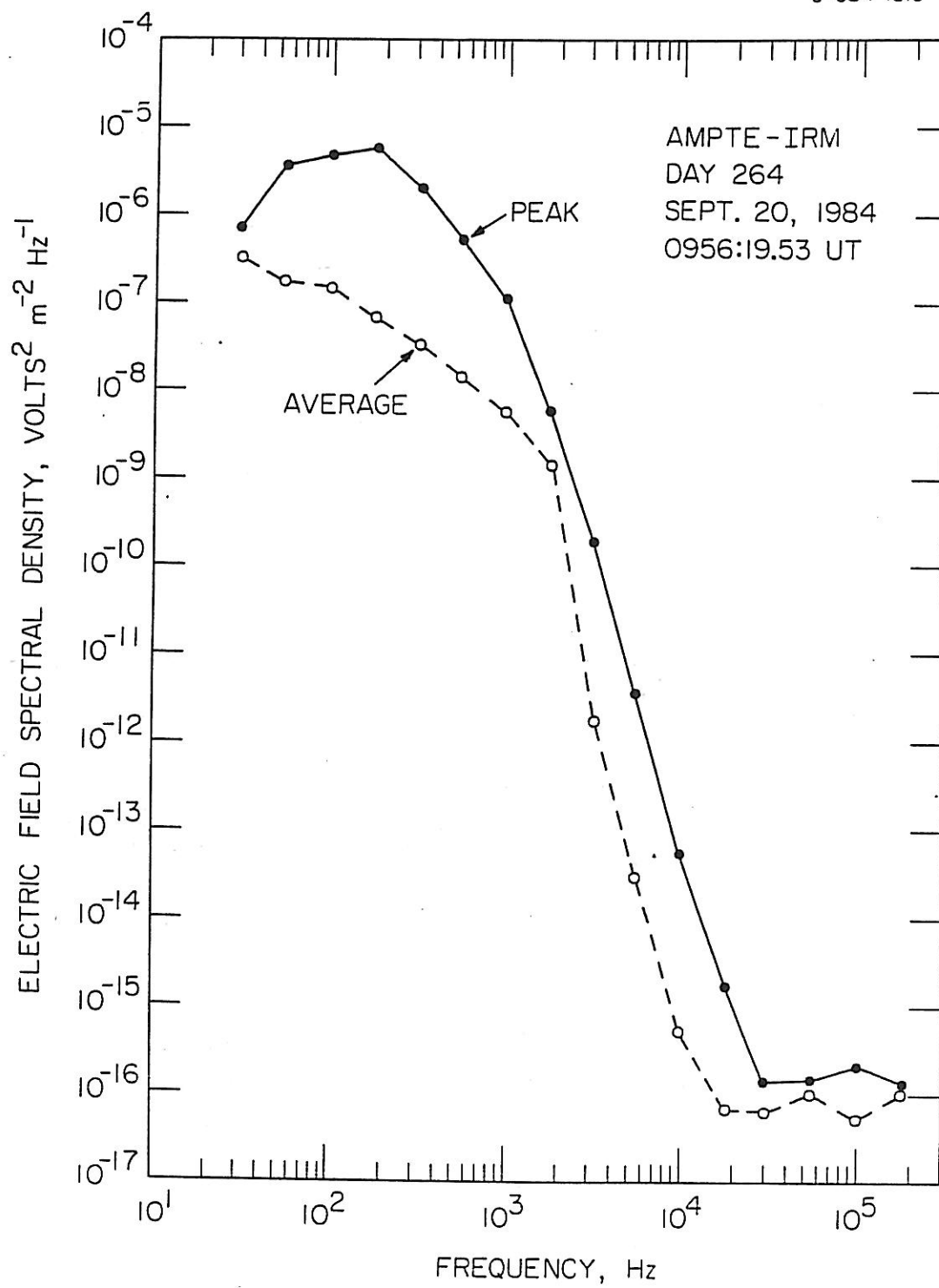


Figure 3

Figure 4 A model for the instability calculation.

Lithium ions are stationary, protons drift with solar wind velocity, V_{sw} , two groups of electrons (hot and cold) drift with a velocity, V_D , between 0 and V_{sw} .

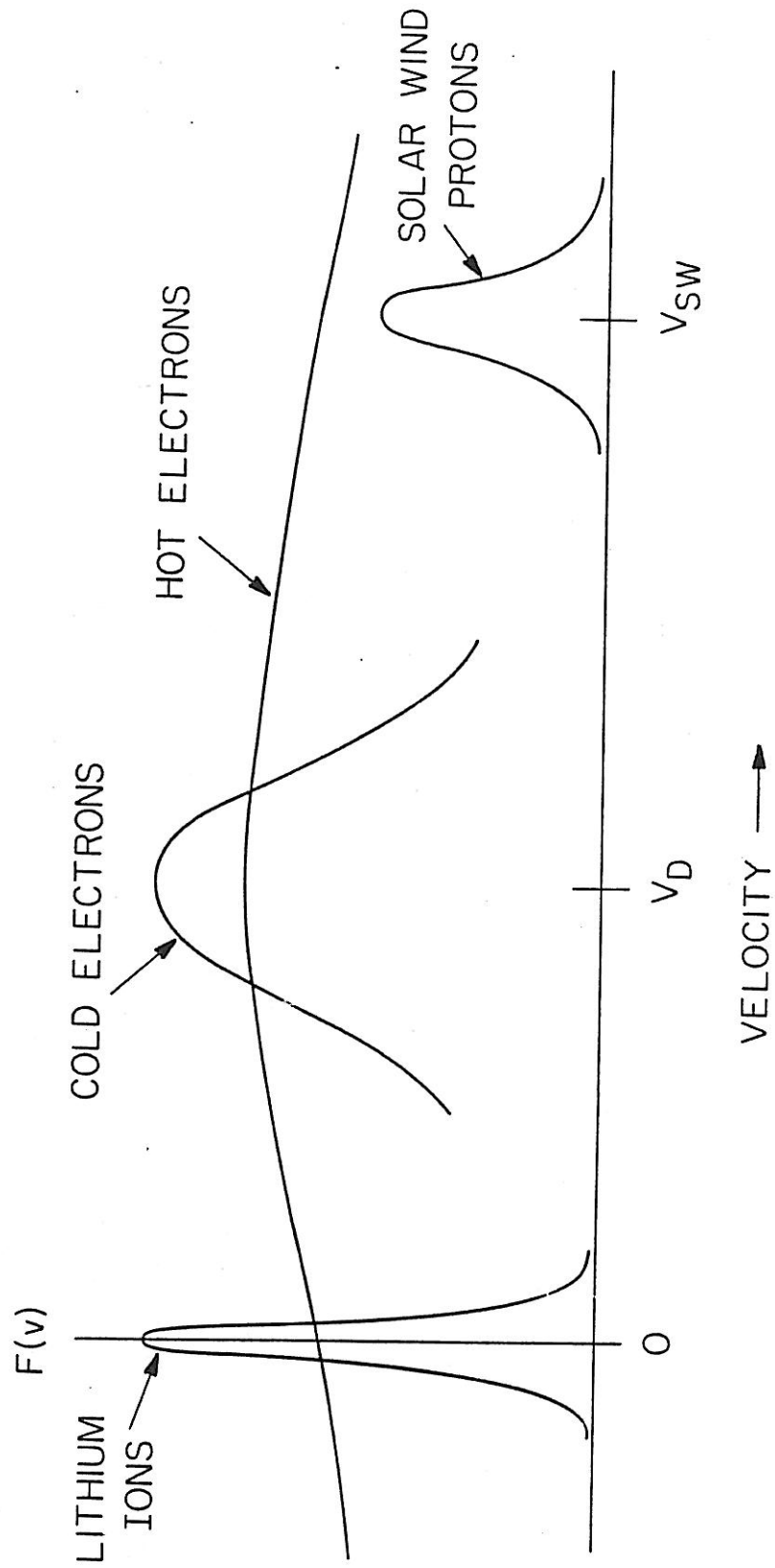


Figure 4

Figure 5. A representative growth rate calculation in the lithium case as $\vec{k} \parallel \vec{V}_{sw}$. The upper panel shows the $k\lambda_D$, wave number normalized by the Debye length, as a function of frequency and the lower panel shows the growth rate, γ , as a function of frequency. The solid curves are for the case $N_e^c = 0$ and the dashed curves are for the case $N_e^c = N_{Li}^+$, assuming $N_{Li}^+ = N_p = 8 \text{ cm}^{-3}$.

A-G86-123-1

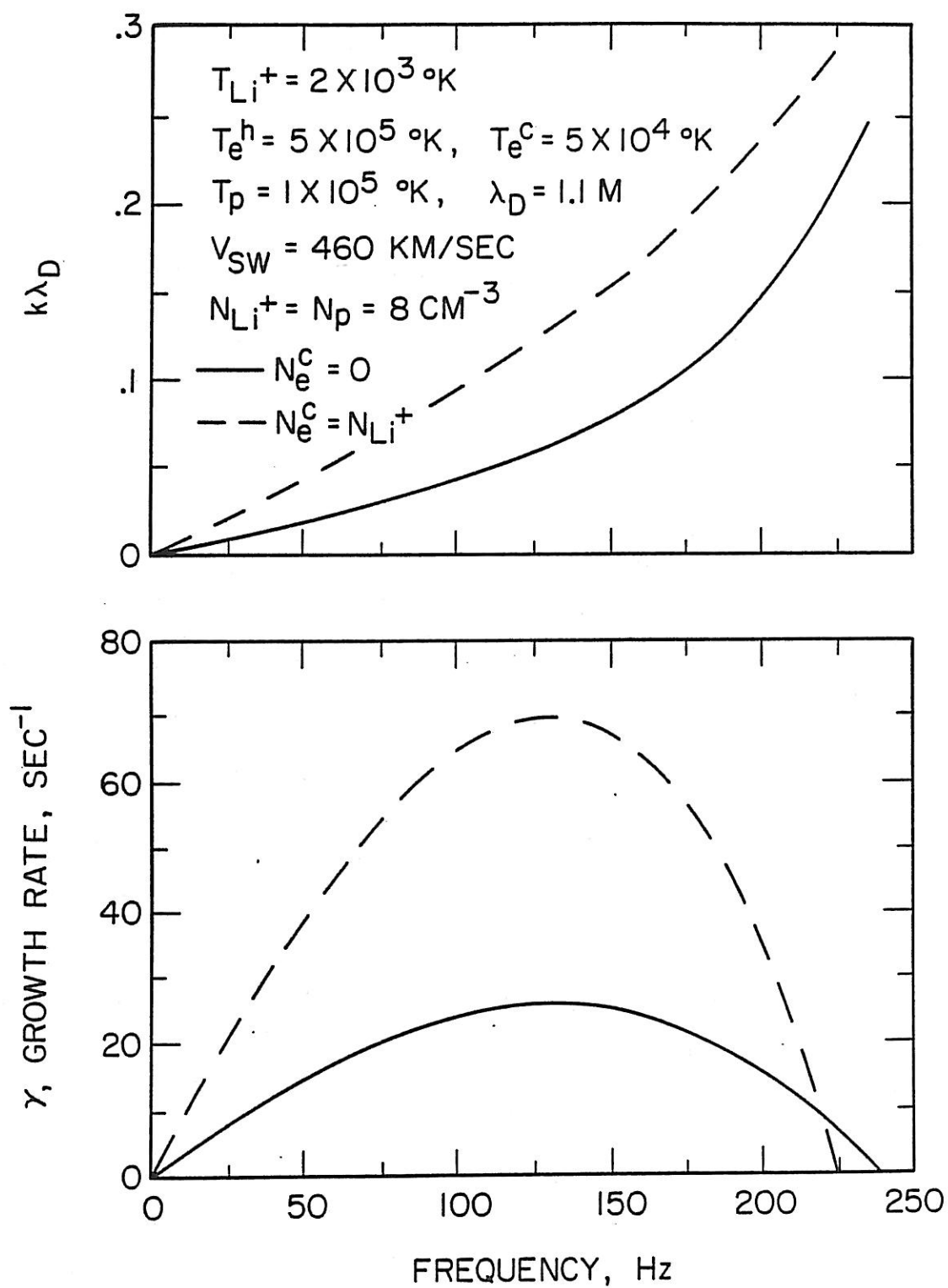
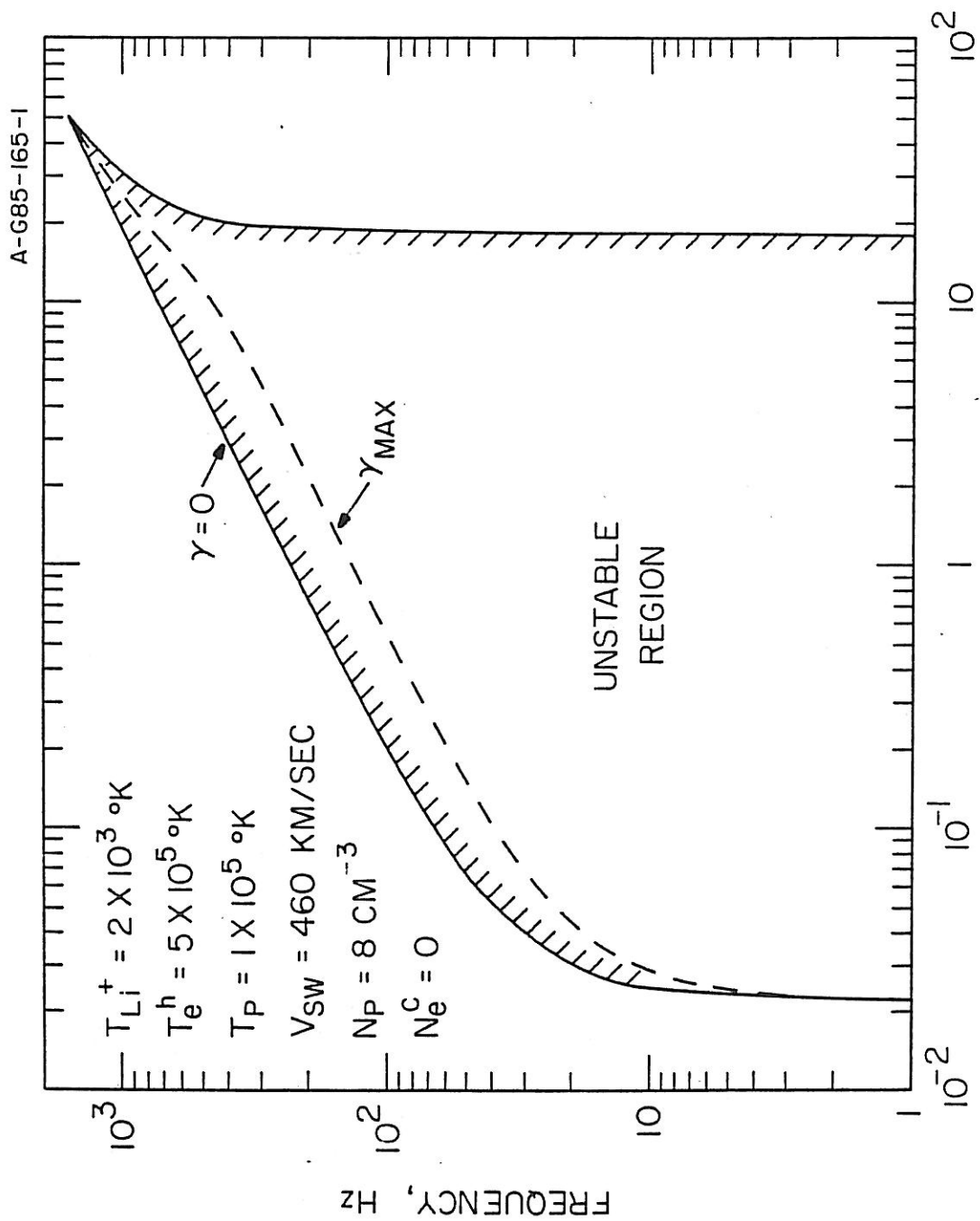


Figure 5

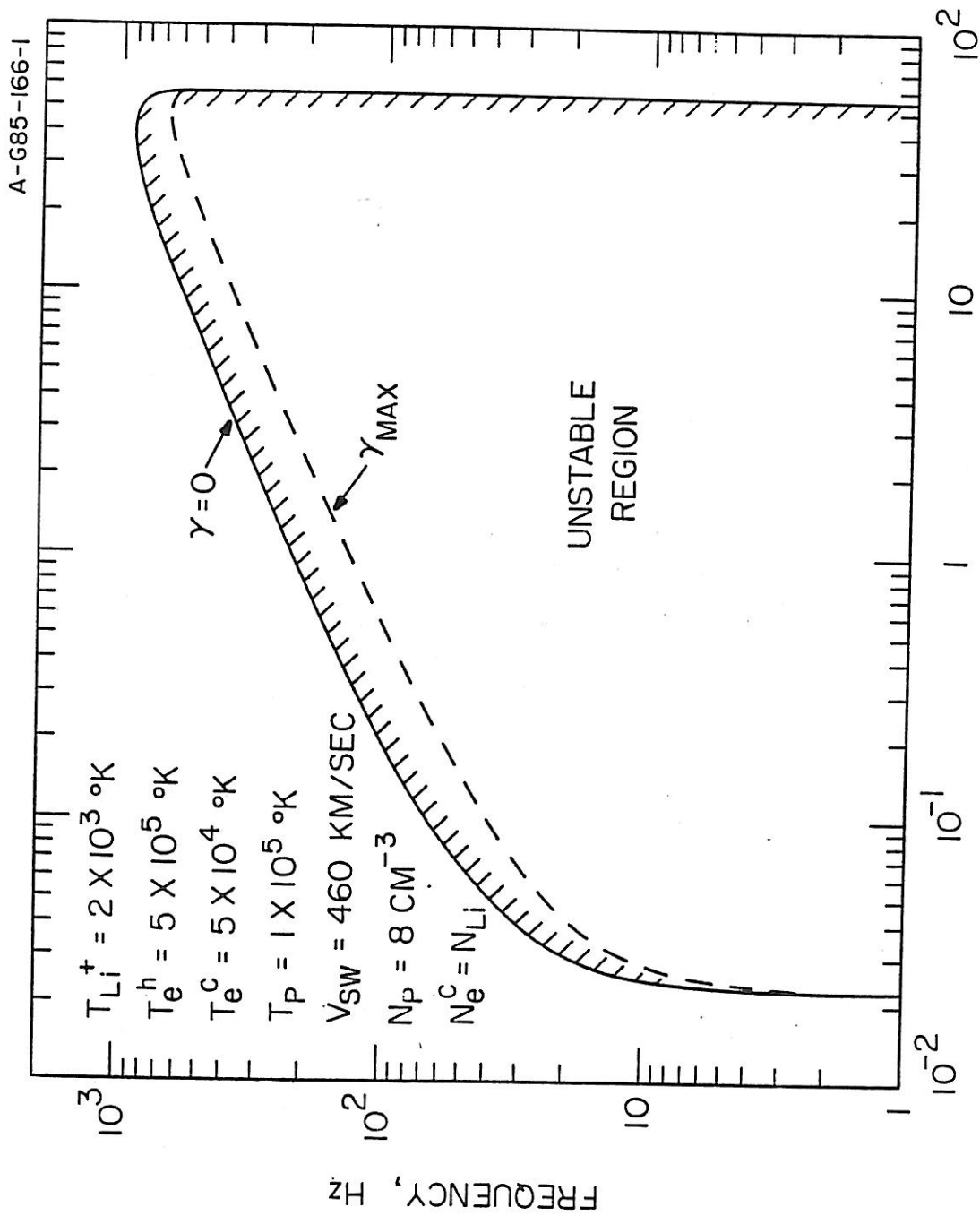
Figure 6. The plots of the frequency of marginal instability, marked $\gamma = 0$, and the frequency for the maximum growth rate, the dashed curve marked γ_{\max} as the functions of the lithium to proton density ratio, N_{Li^+}/N_p , for the case $\vec{k} \parallel \vec{V}_{\text{sw}}$, $N_e^c = 0$.



N_{Li^+}/N_P , LITHIUM TO PROTON DENSITY RATIO
 Figure 6

Figure 7. The similar plots as in Figure 6 for the case

$$N_e^c = N_{Li}^+.$$



N_{Li^+}/N_P , LITHIUM TO PROTON DENSITY RATIO
 Figure 7

Figure 8. The maximum growth rates, γ_{\max} , as the functions of N_{Li}^+/N_p , for the case $\vec{k} \parallel \vec{V}_{sw}$. The solid curve is for the case $N_e^c = 0$, and the dashed curve is for the case $N_e^c = N_{Li}^+$.

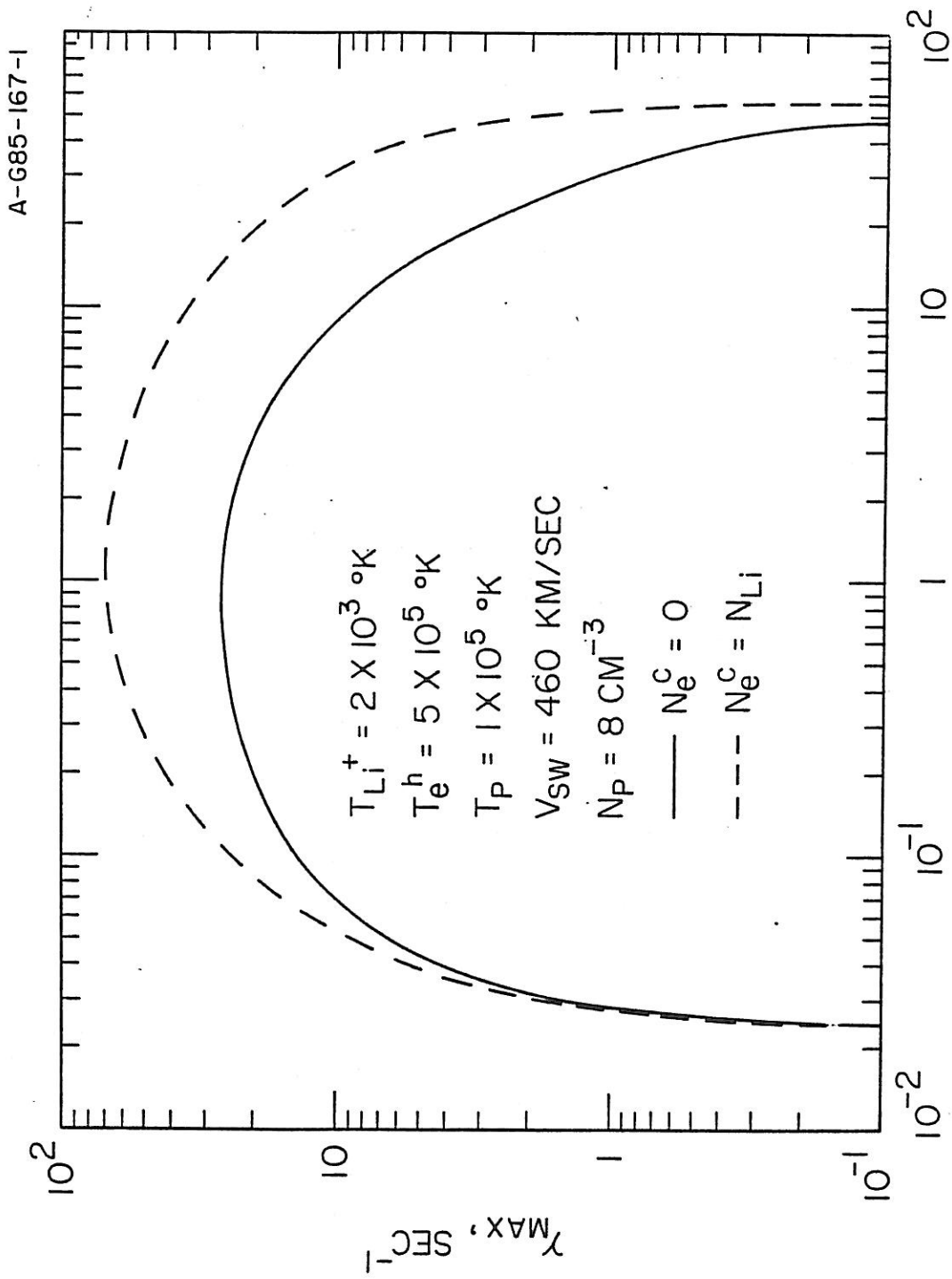


Figure 8
 $N_{\text{Li}}^+/N_{\text{P}}$, LITHIUM TO PROTON DENSITY RATIO

Figure 9. Illustration for the current effect to the marginal instability boundary. The cross-hatched region shows the variation in the $\gamma = 0$ boundary for a $\pm 25\%$ variation in the electron drift velocity.

B - G85 - 253

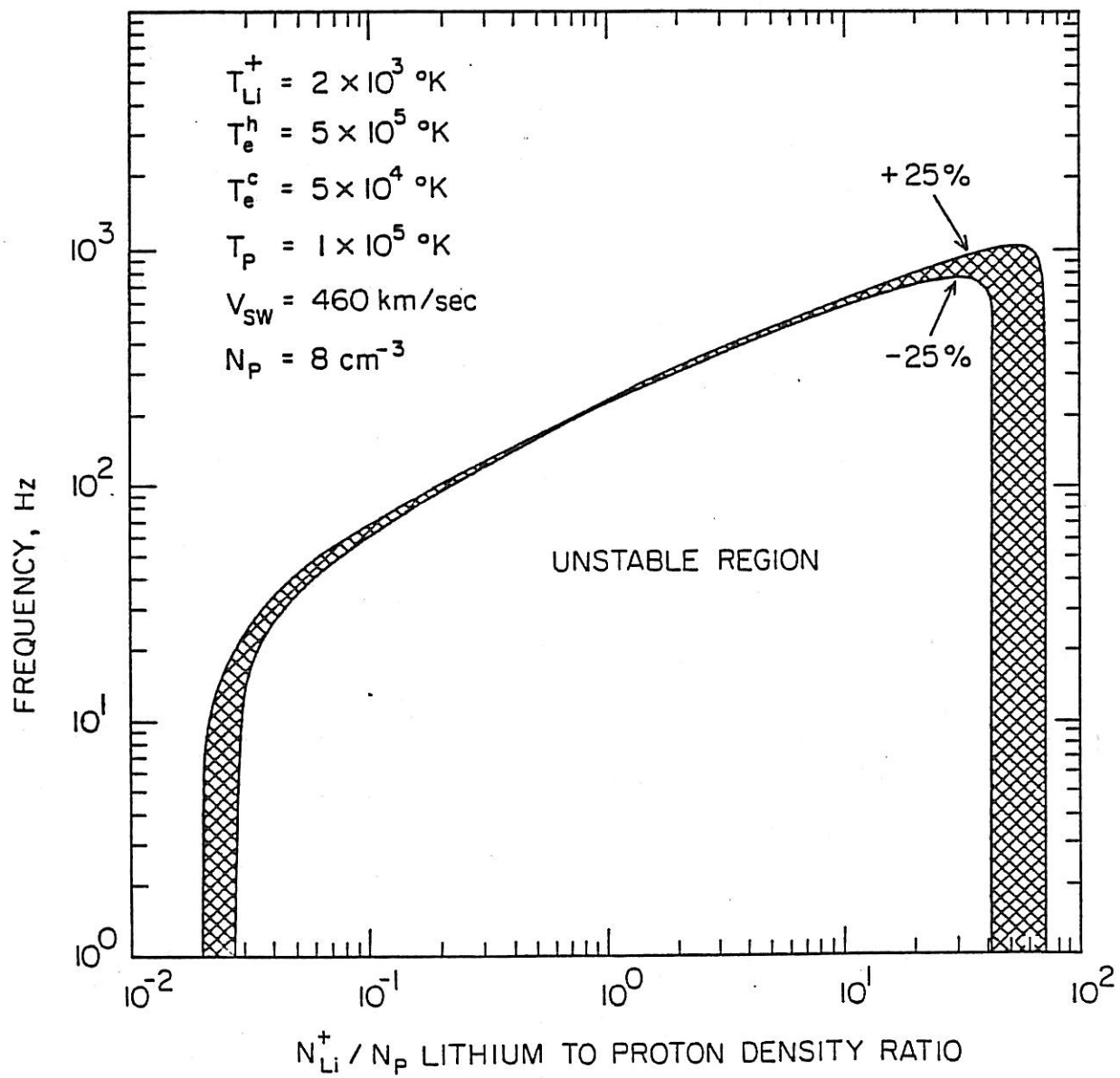


Figure 9

Figure 10. Plots of maximum growth rates, γ_{\max} , versus θ , the angle between \vec{k} and \vec{V}_{sw} for the case $N_{\text{Li}}^+ = N_{\text{p}} = 8 \text{ cm}^{-3}$. The solid curve is for $N_{\text{e}}^{\text{c}} = 0$, and the dashed curve is for $N_{\text{e}}^{\text{c}} = N_{\text{Li}}^+$.

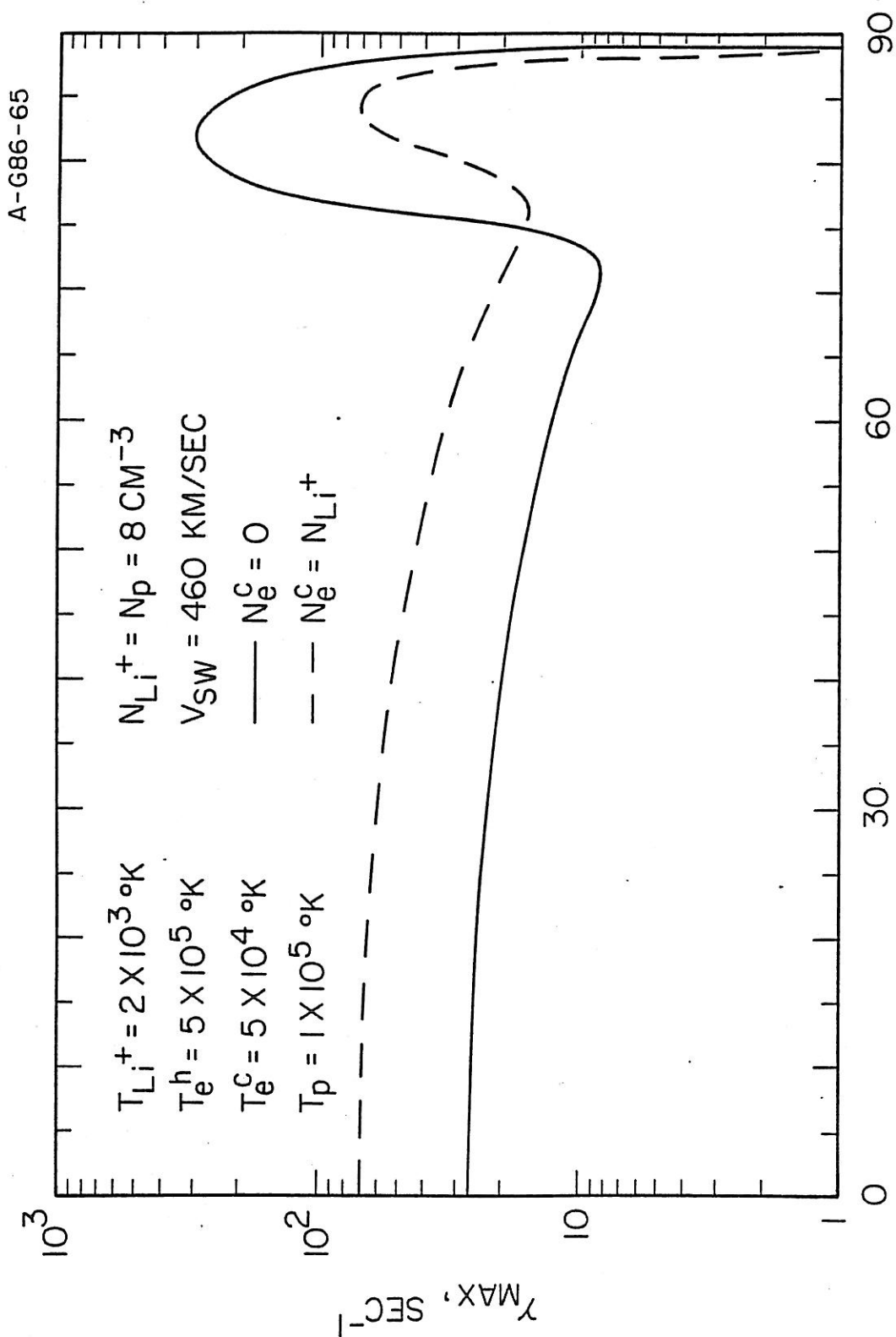


Figure 10

Figure 11. A plot of $k\lambda_D$, wave number normalized by the Debye length of the plasma, as a function of frequency (upper panel) and γ , growth rate, as a function of frequency (lower panel) for the case $N_{Li}^+ = N_p = 8 \text{ cm}^{-3}$, $N_e^c = 0$, and $\theta = 82^\circ$.

A-G86-63-1

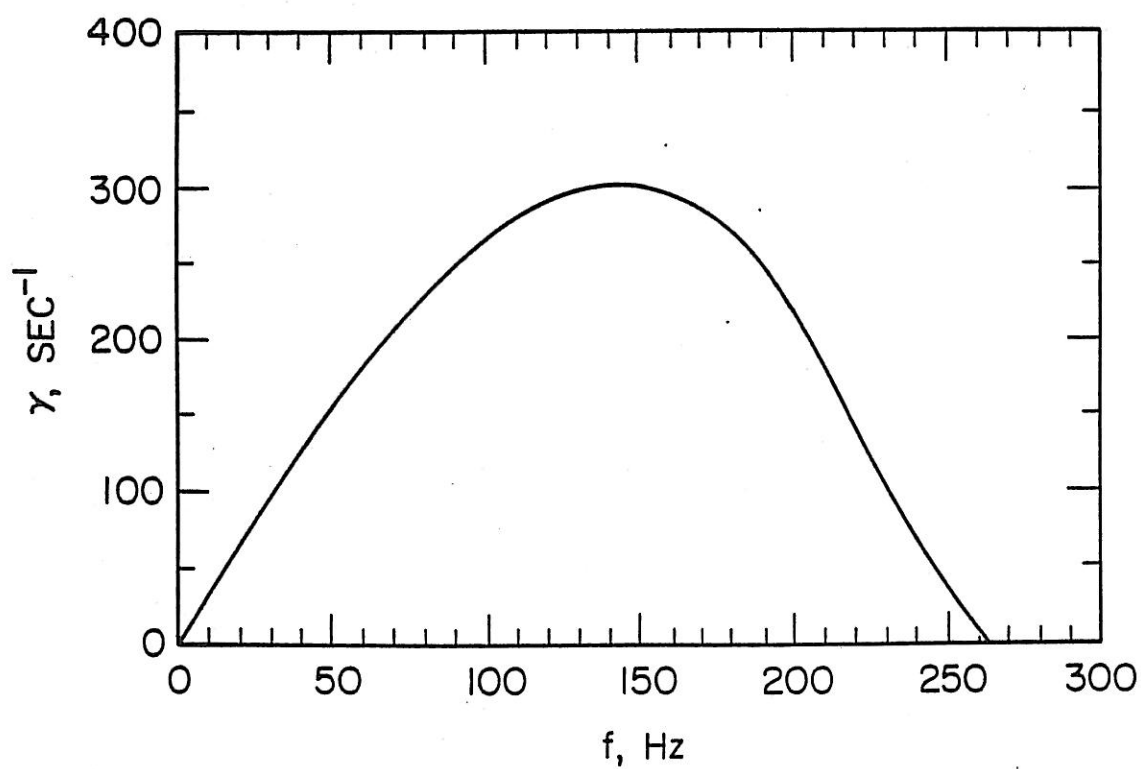
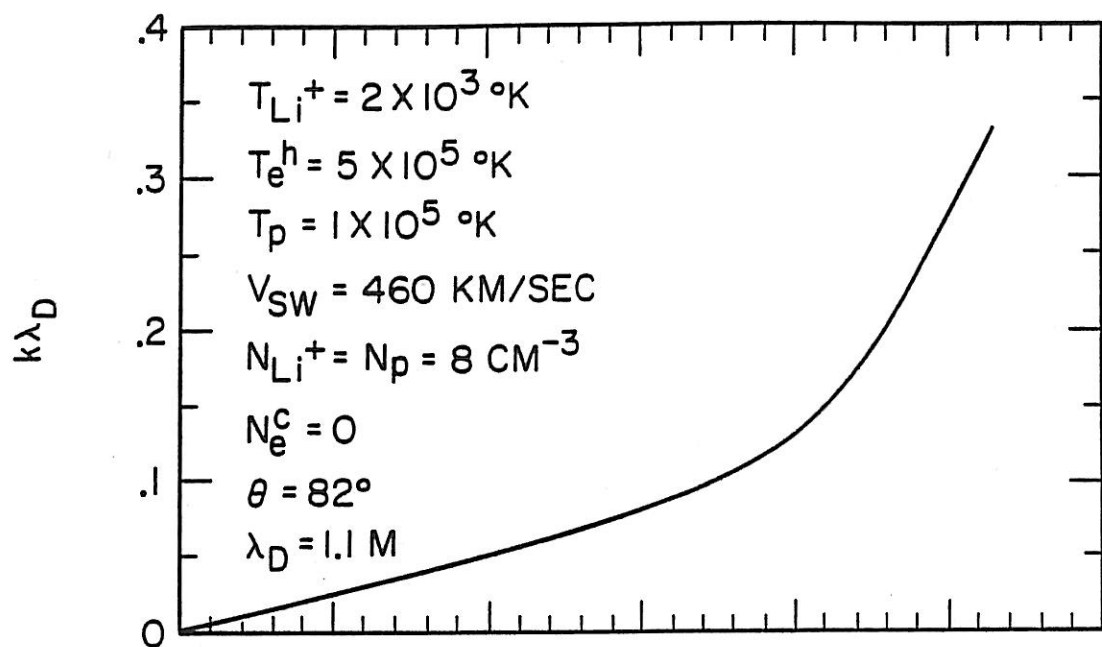
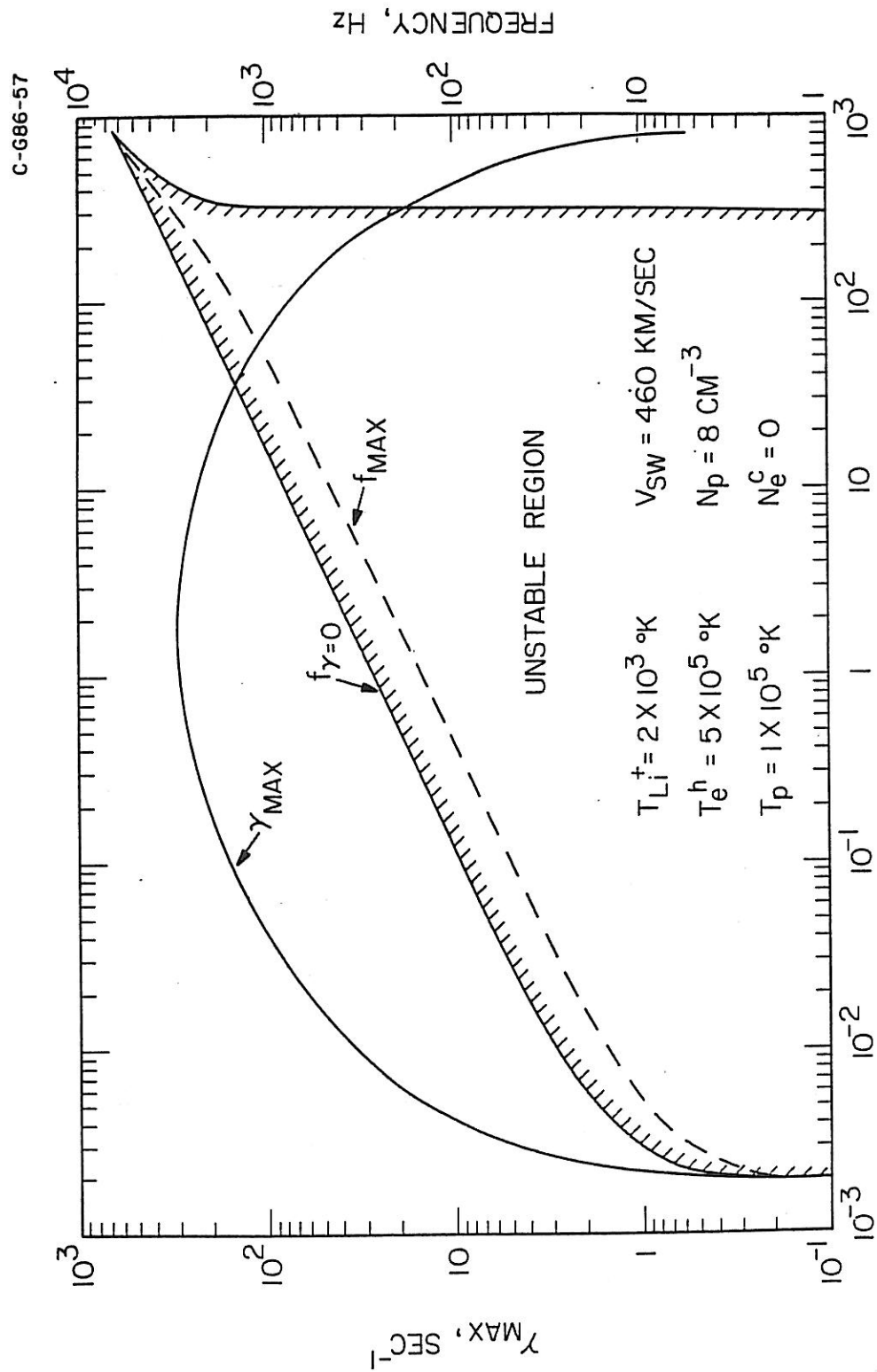


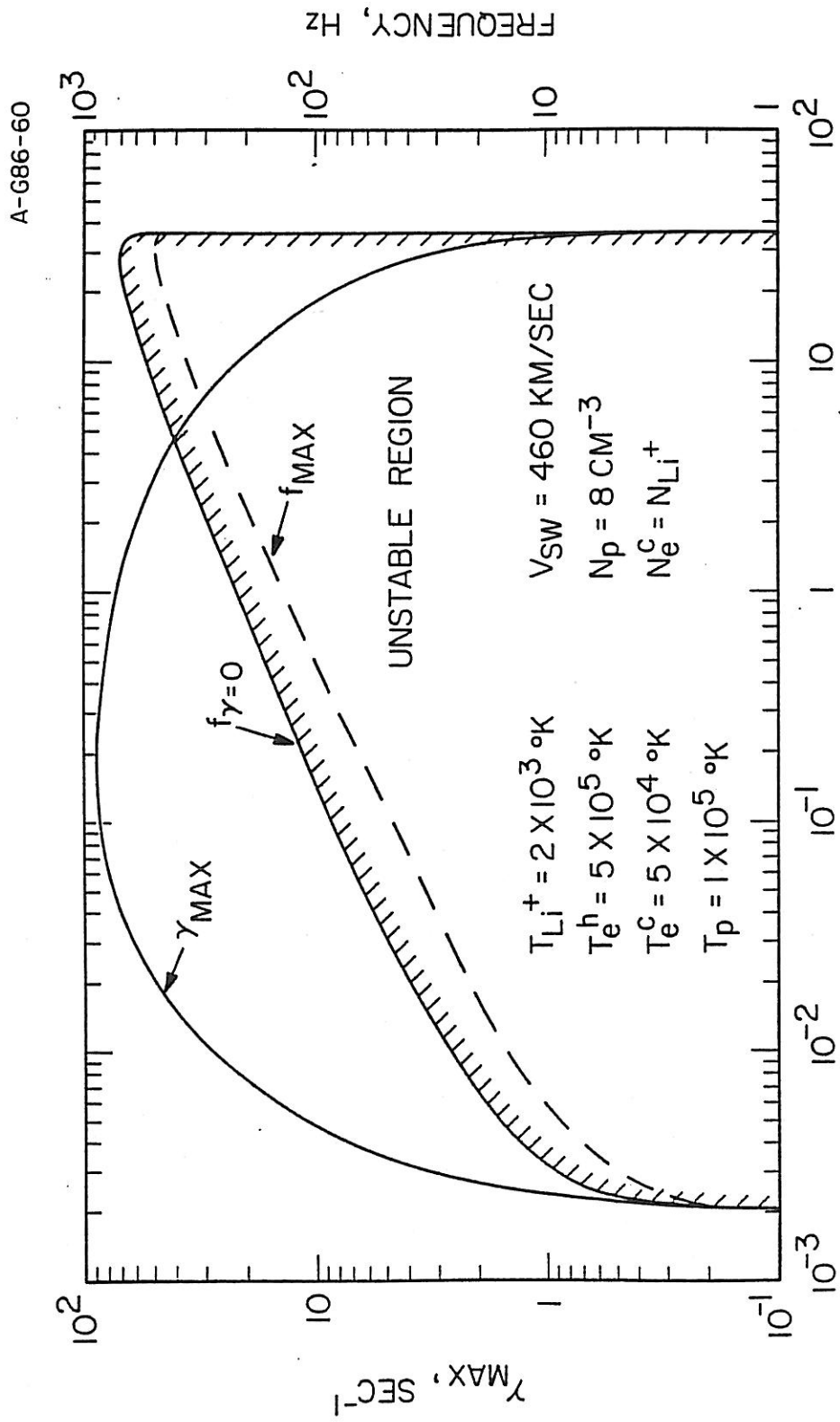
Figure 11

Figure 12. Plots of $f_{\gamma=0}$, the frequency for the marginal instability, vs. N_{Li}^+/N_p , lithium to proton density ratio; γ_{max} , maximum growth rate (maximized over k and θ), vs. N_{Li}^+/N_p , and f_{max} , the frequency for the maximum growth rate, vs. N_{Li}^+/N_p . Assume $N_p = 8 \text{ cm}^{-3}$, $N_e^c = 0$.



N_{Li^+}/N_p , LITHIUM TO PROTON DENSITY RATIO
Figure 12

Figure 13. The same plots as in Figure 12 for $N_e^c = N_{Li}^+$.

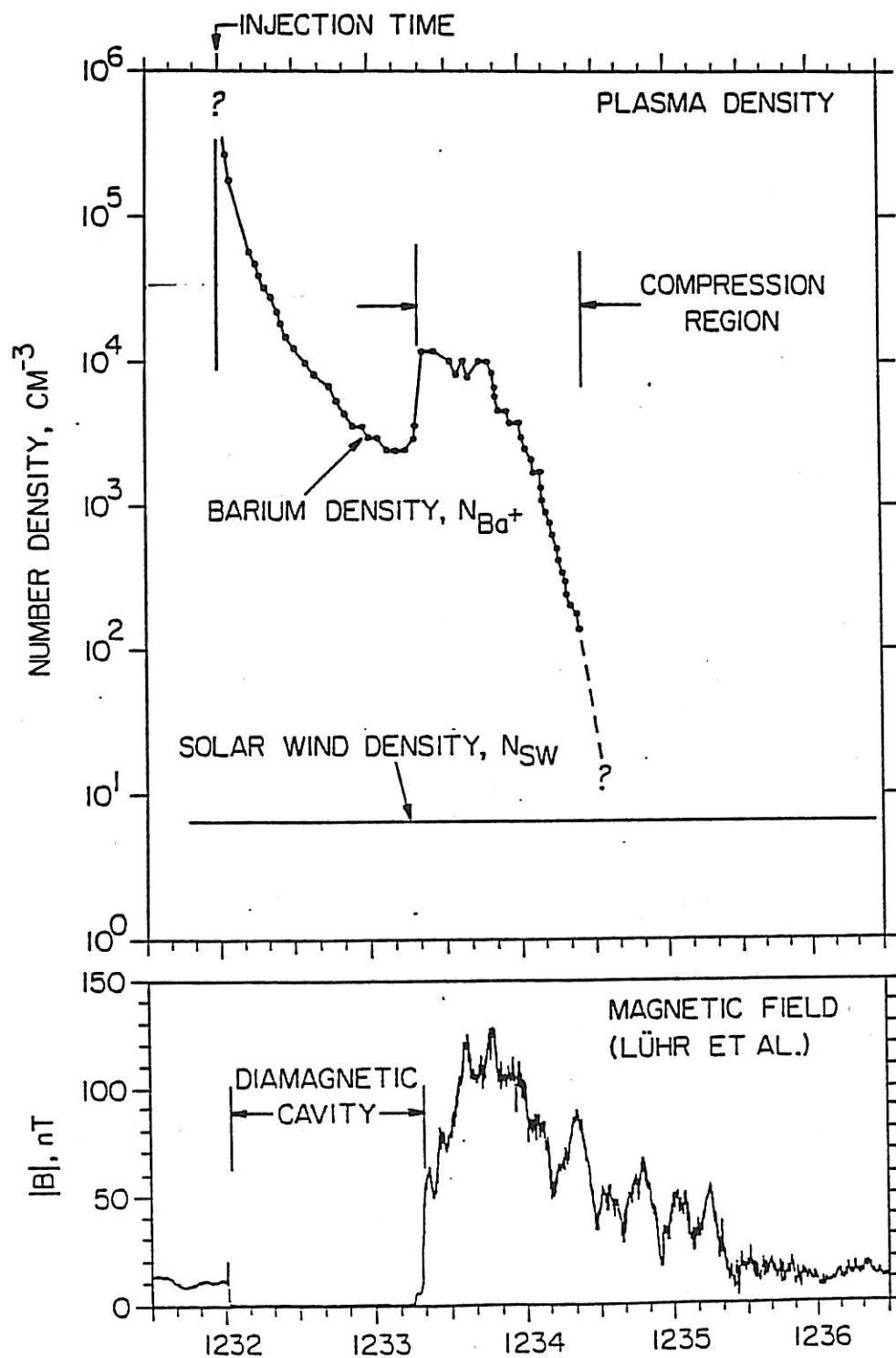


N_{Li^+}/N_p , LITHIUM TO PROTON DENSITY RATIO

Figure 13

Figure 14. A plot of the plasma density obtained from the electron plasma oscillation (top panel) and the magnetic field from the magnetometer (bottom panel) during the solar wind barium release on December 27, 1984. The diamagnetic cavity and the compression region are indicated.

C-G85-506



AMPTE-IRM, DEC. 27, 1984

Figure 14

Figure 15. A 16-channel electric field intensity plot. The shock-like noise is observed near the outer boundary of the plasma compression region. It lasts about 1 minute.

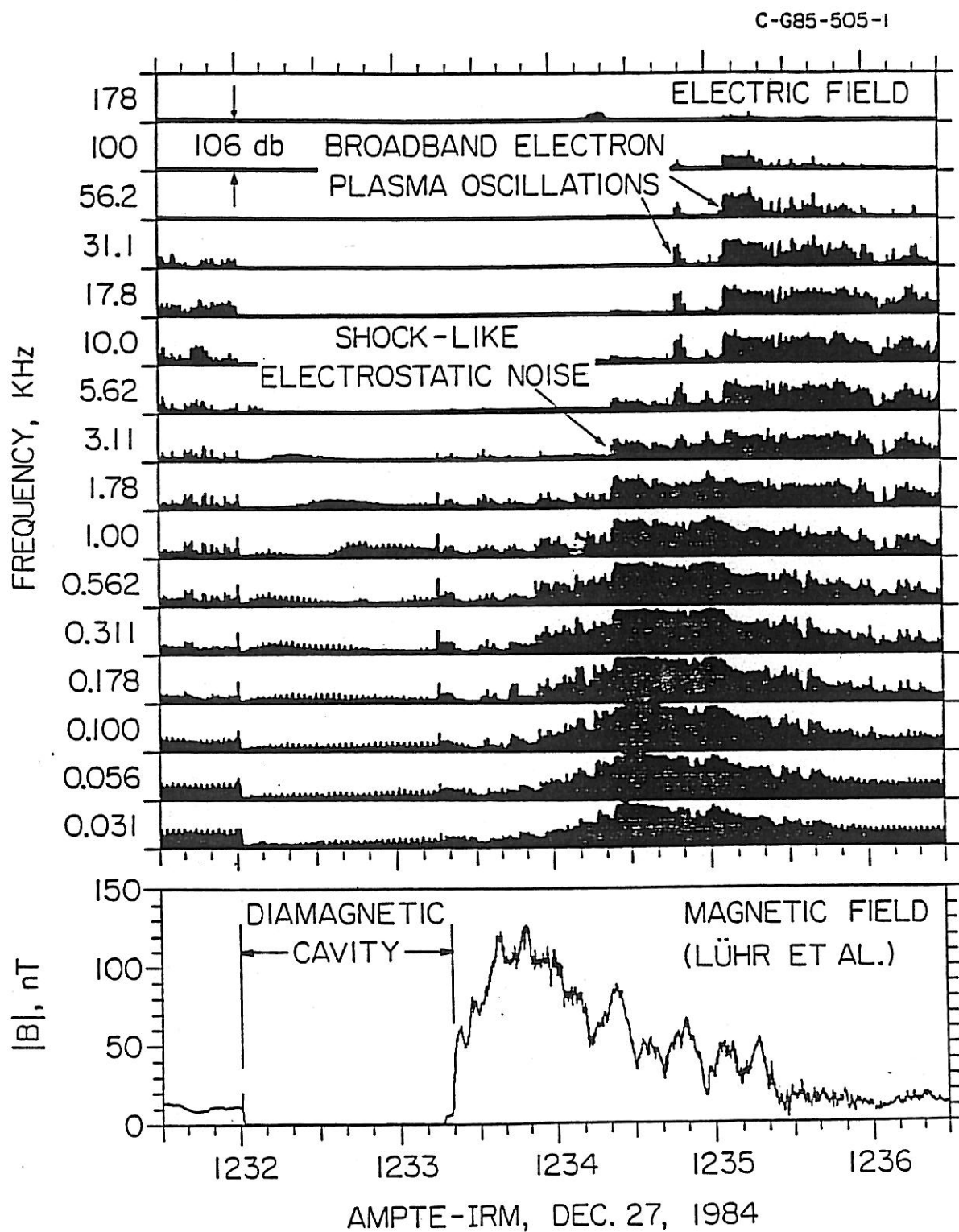
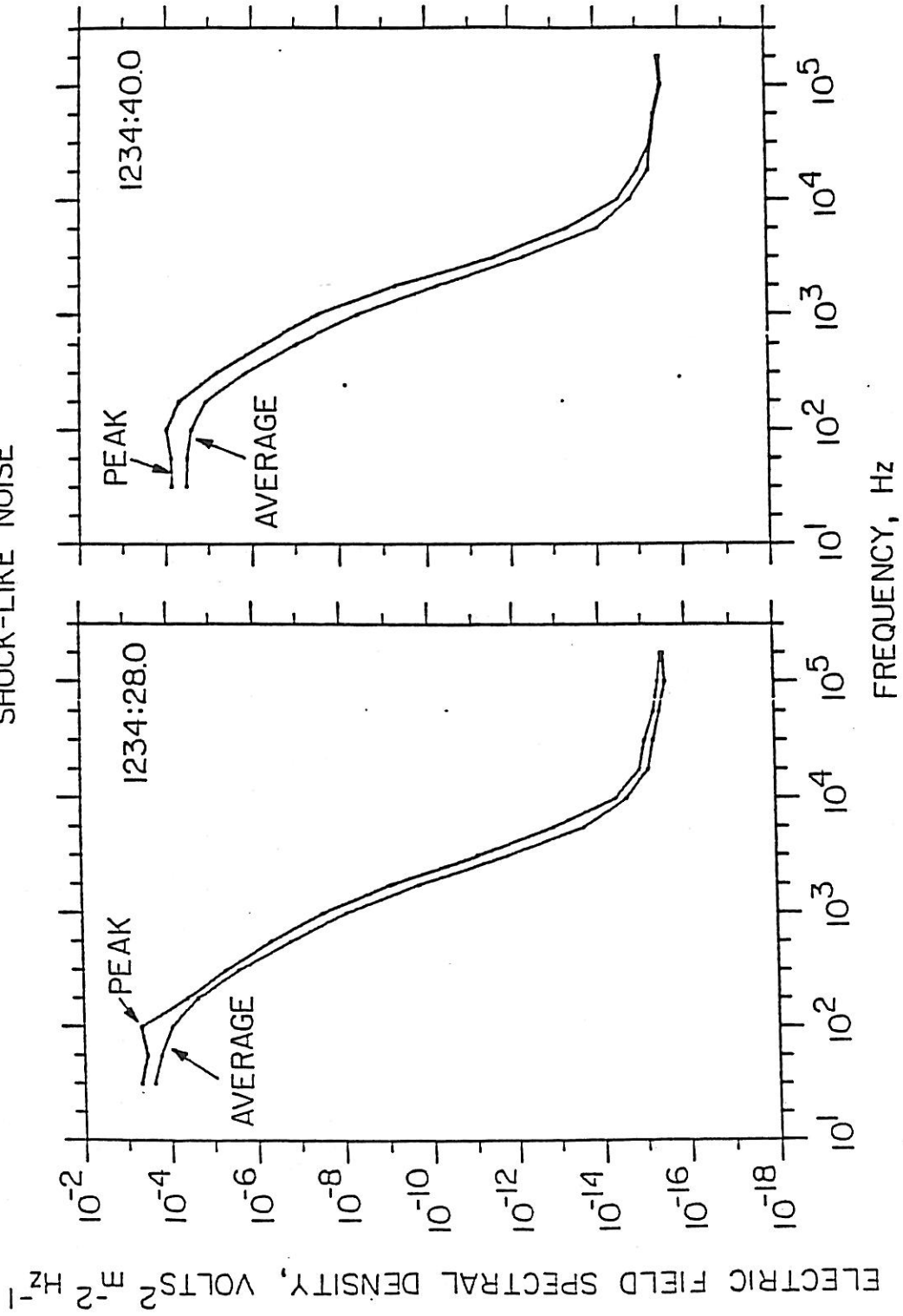


Figure 15

Figure 16. The spectrums of the intense shock-like electrostatic noise at the time 1234:28 and 1234:40 UT. Most of the power in this noise is concentrated at frequencies below a few hundred Hz.

SHOCK-LIKE NOISE



AMPTE-IRM, DEC. 27, 1984

Figure 16

Figure 17. A model for the instability analysis for the artificial comet experiment. Barium ions are stationary, protons stream through the barium plasma with the solar wind velocity. Two groups of electrons (hot and cold) drift with a velocity, V_D , between 0 and V_{sw} .

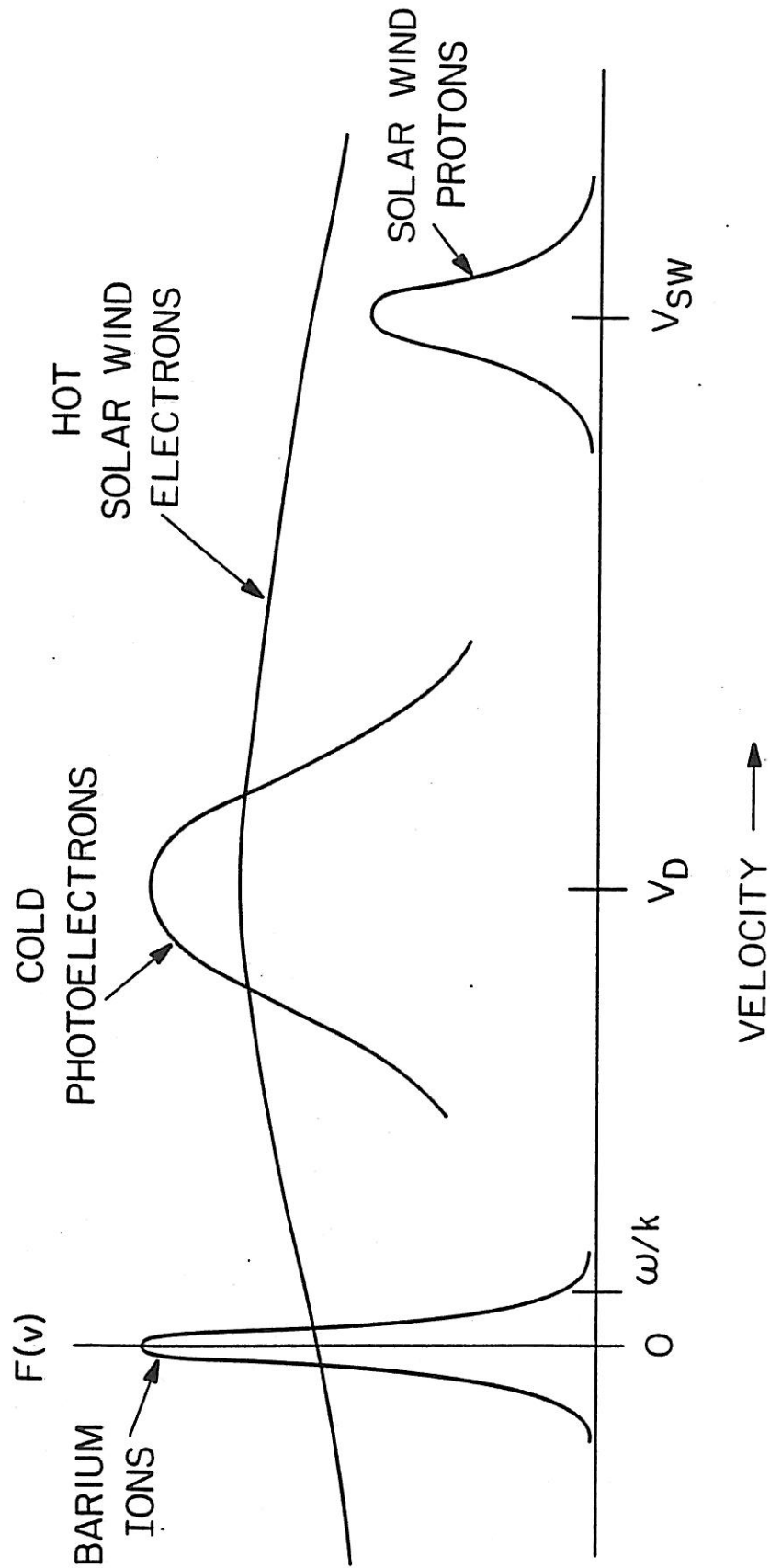


Figure 17

Figure 18. A representative growth rate calculation for $N_{Ba}^+ = 10$ $N_p = 80 \text{ cm}^{-3}$, $N_e^c = N_{Ba}^+$, $\theta = 0$. The upper panel shows $k\lambda_D$ vs. frequency and the lower panel shows γ vs. frequency.

A-G85-709-2

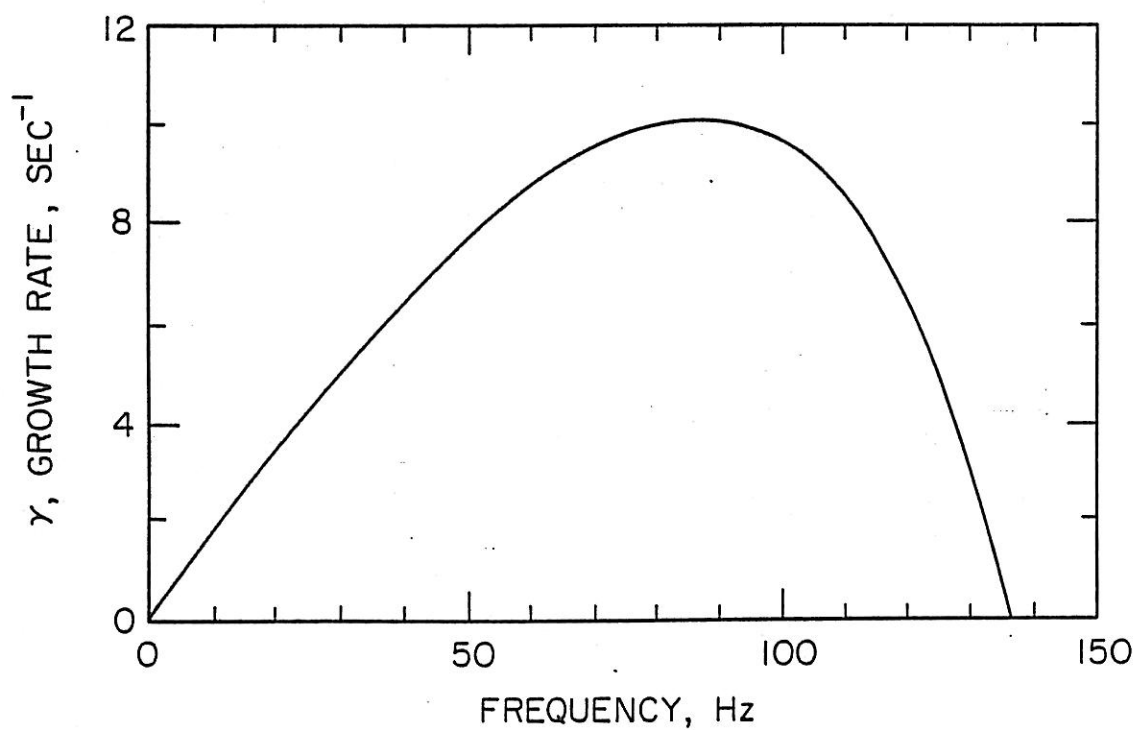
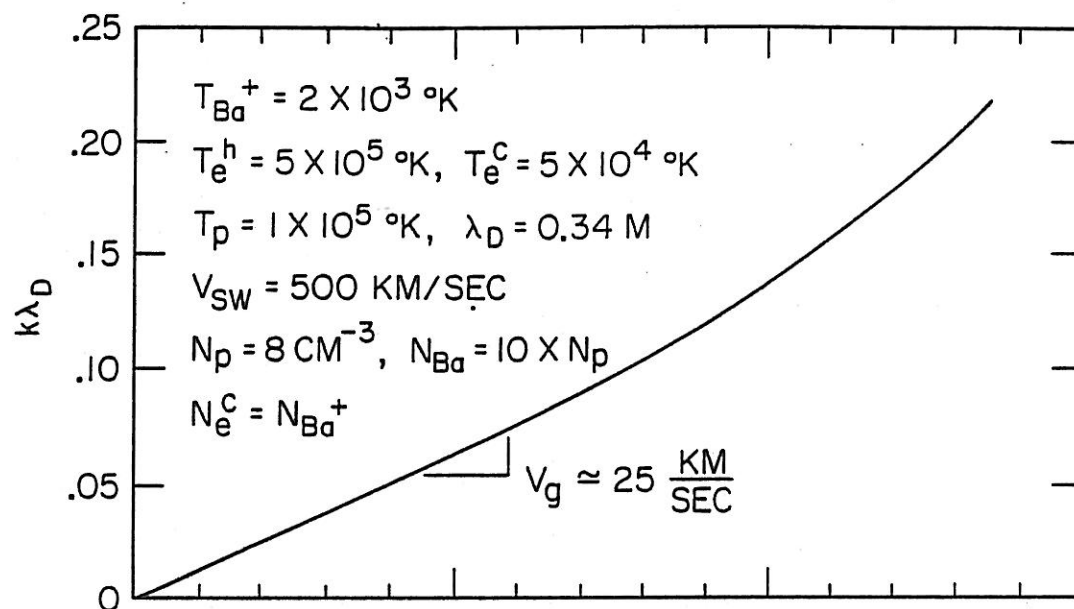


Figure 18

Figure 19. A plot of the frequency for the marginal stability, labelled $\gamma = 0$, and the frequency for the maximum growth rate, the dashed curve marked γ_{\max} , as the functions of N_{Ba}^+/N_p , the barium to proton density ratio for $\theta = 0^\circ$, $N_e^c = 0$.

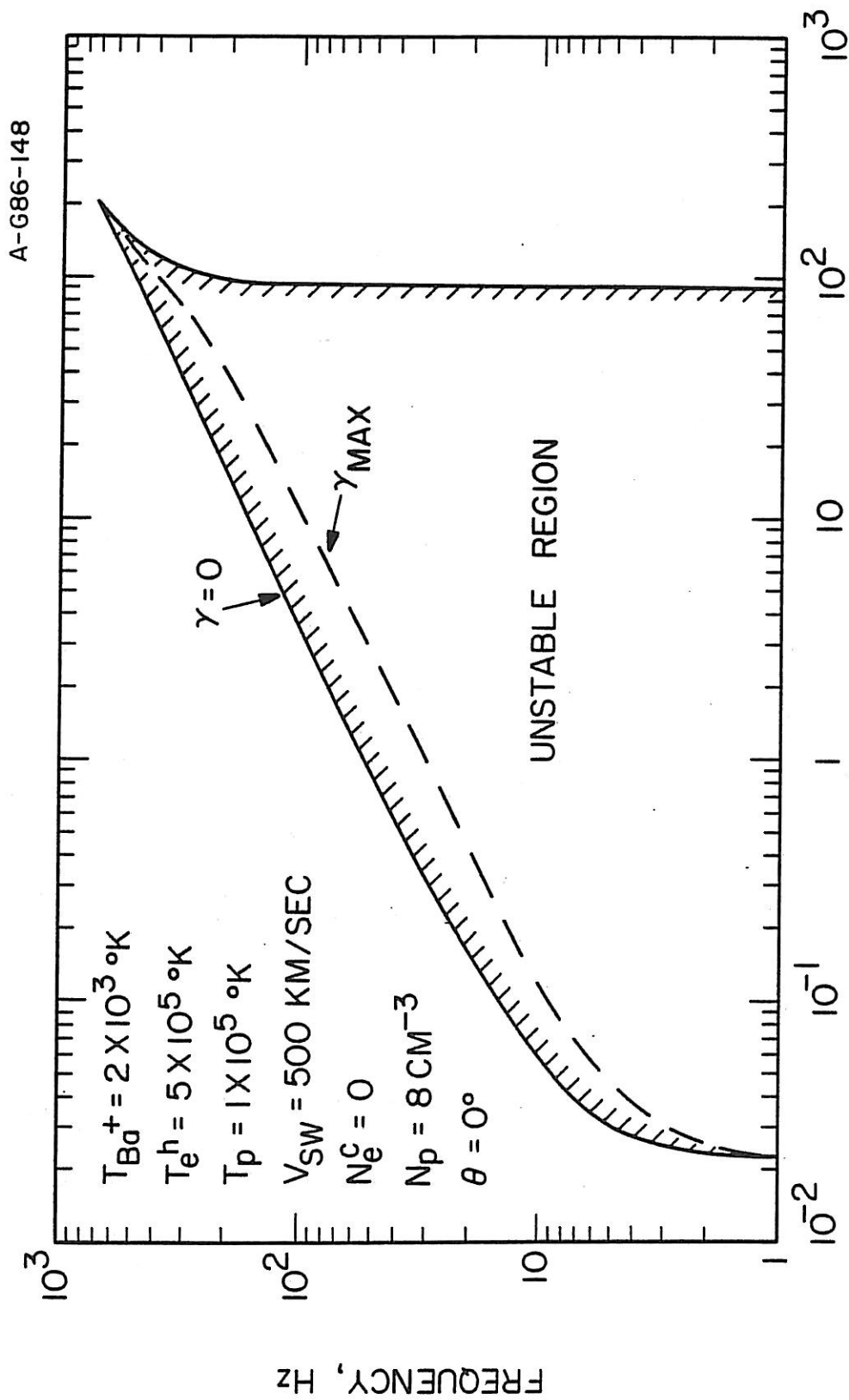
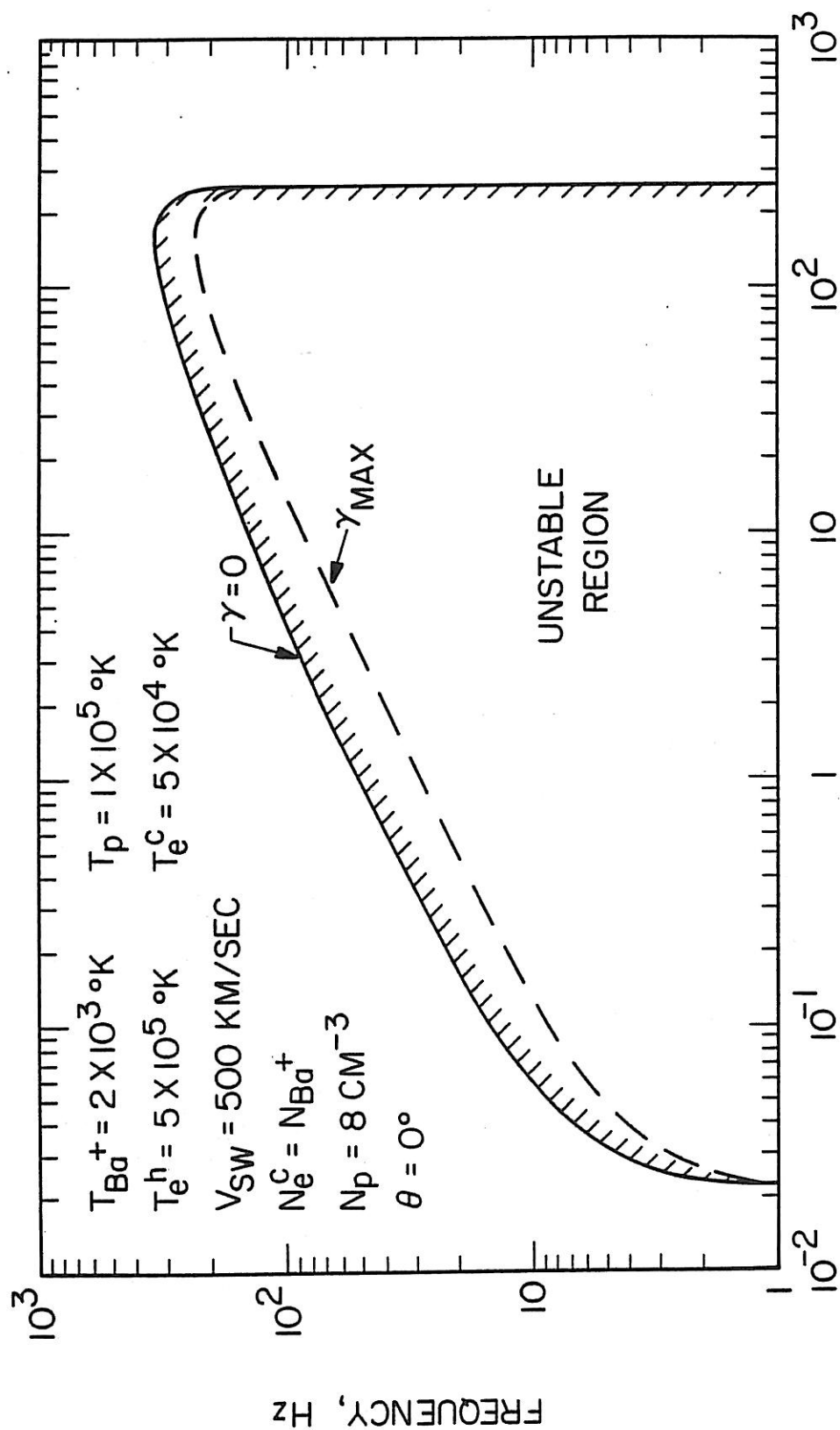


Figure 19

Figure 20. The same plot as in Figure 19 for $N_e^c = N_{Ba}^+$.

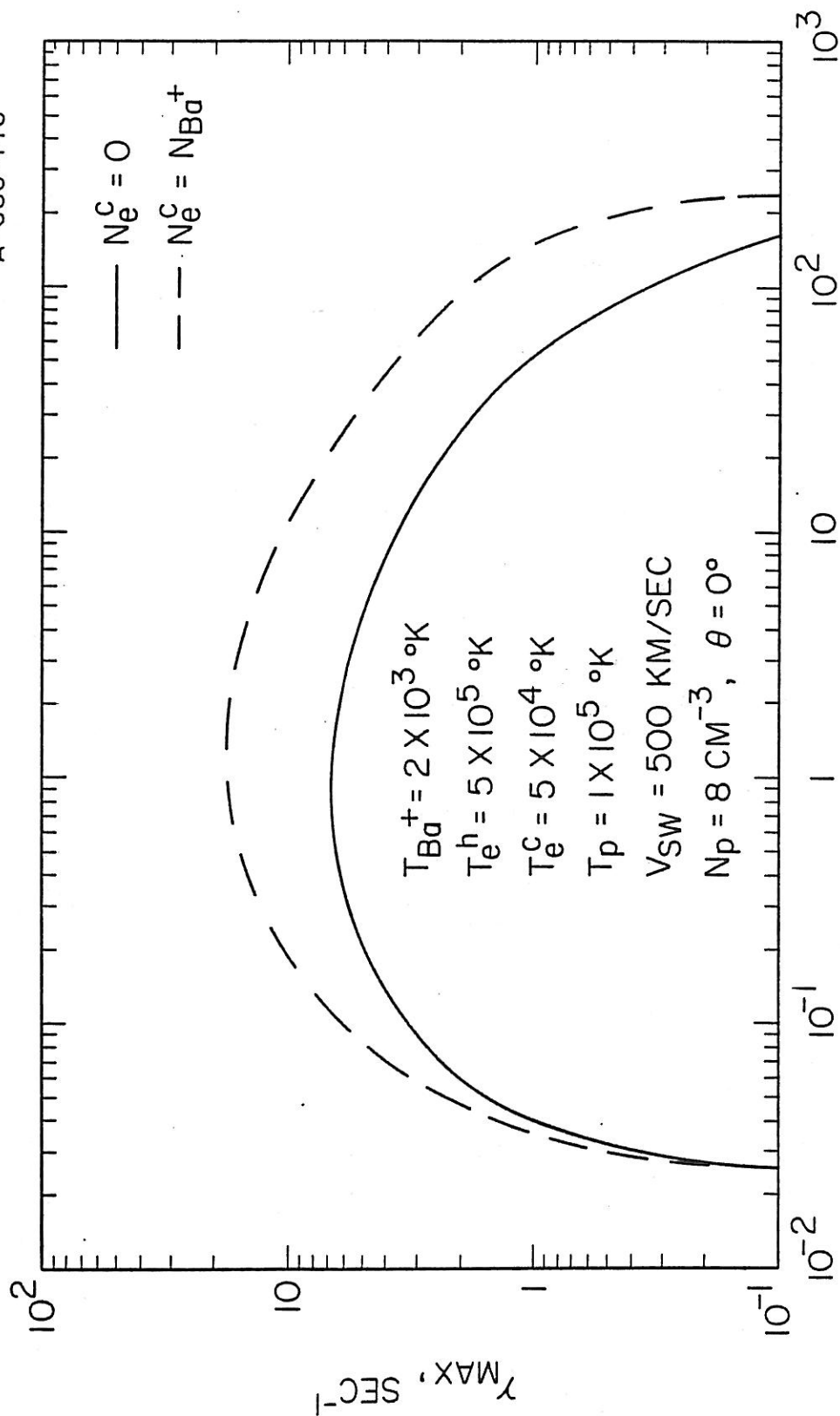


N_{Ba^+}/N_p , BARIUM TO PROTON DENSITY RATIO

Figure 20

Figure 21. A plot of the maximum growth rates versus N_{Ba}^+/N_p for $\theta = 0^\circ$. The solid curve is for $N_e^c = 0$ and the dashed curve is for $N_e^c = N_{Ba}^+$.

A-G86-146



$N_{Ba^{+}}/N_p$, BARIUM TO PROTON DENSITY RATIO

Figure 21

Figure 22. Plots of maximum growth rates versus θ for $N_{Ba}^+ = 10 N_p = 80 \text{ cm}^{-3}$. The solid curve is for the case $N_e^c = 0$ and the dashed curve is for the case $N_e^c = N_{Ba}^+$.

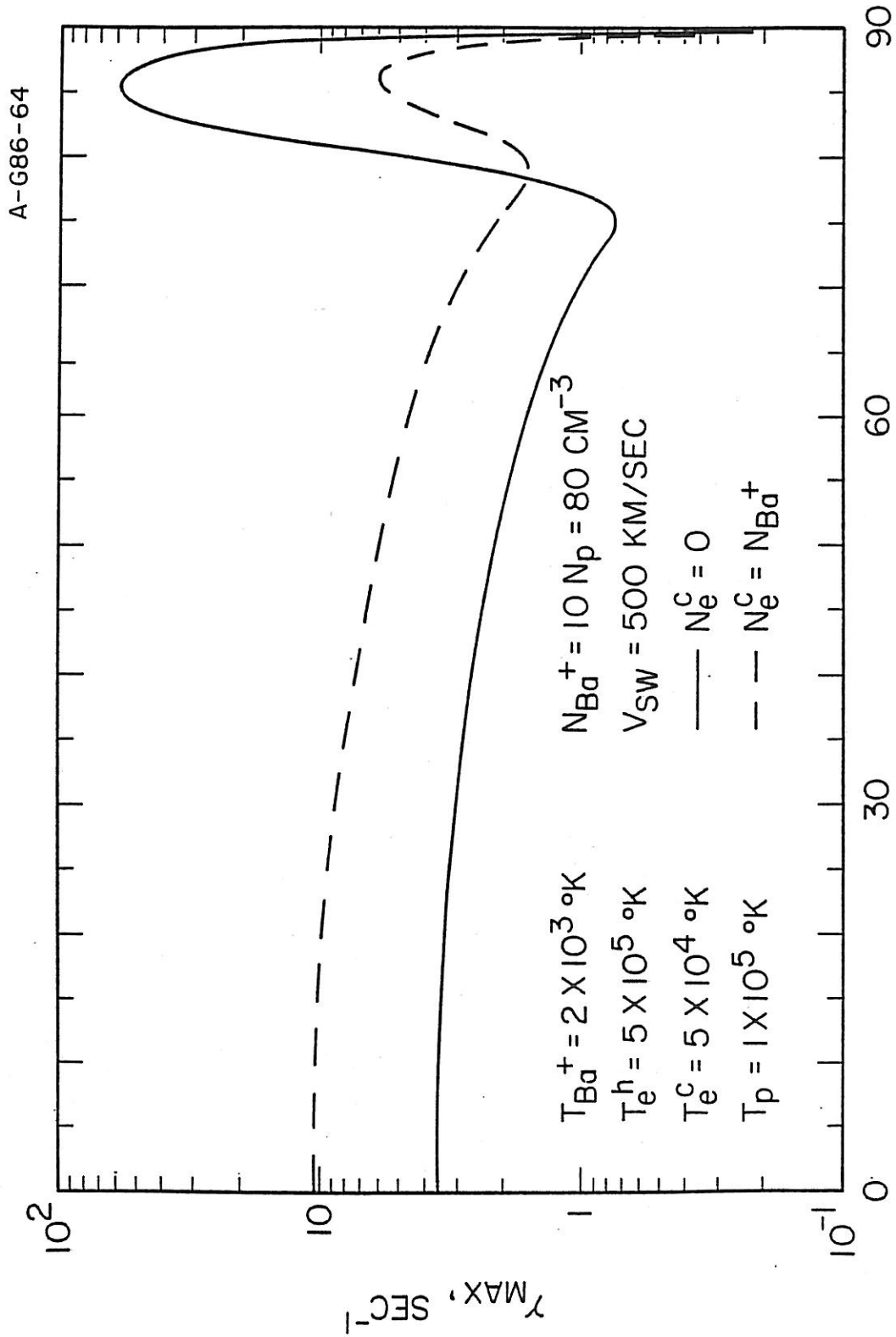


Figure 22

Figure 23. Plots of $k\lambda_D$ vs. f (upper panel) and γ vs f (lower panel) for $N_e^c = 0$, $N_{Ba}^+ = 10$ $N_p = 80$ cm^{-3} , $\theta = 85.5^\circ$.

A-G86-62-1

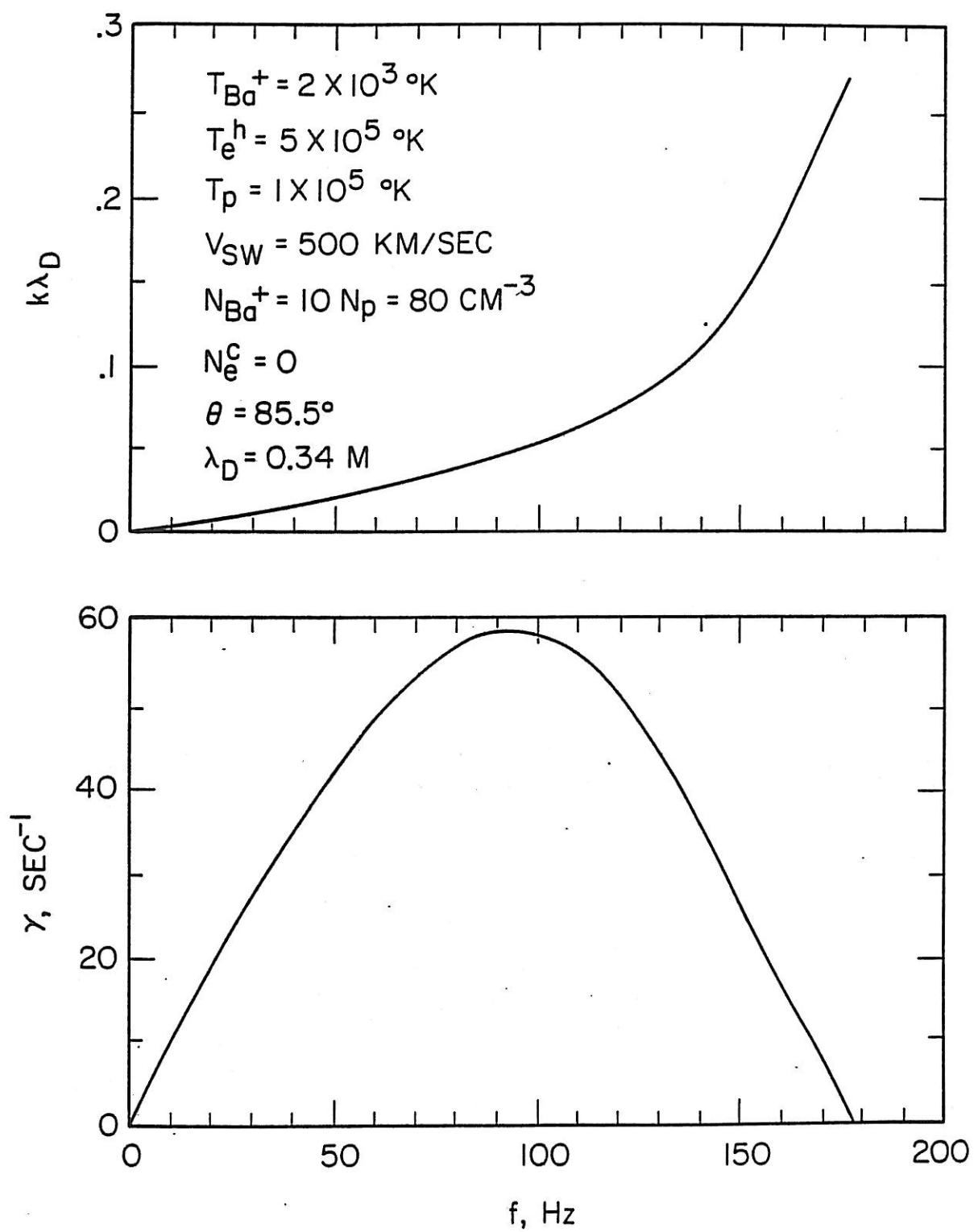
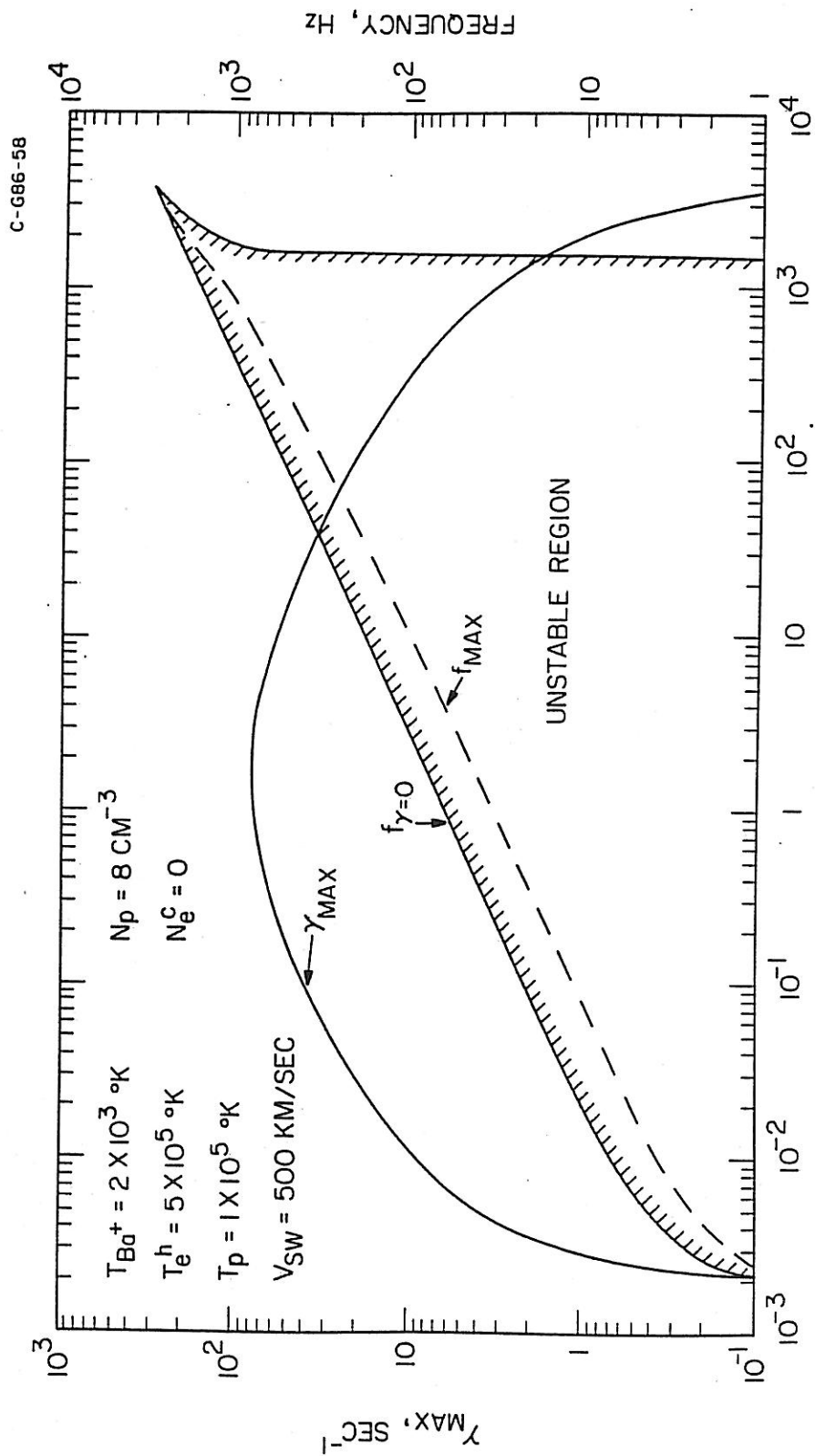


Figure 24. Plots of the frequency for the marginal instability, $f_{\gamma=0}$, vs. N_{Ba}^+/N_p , the barium to proton density ratio and the maximum growth rate, γ_{max} , vs. N_{Ba}^+/N_p , and the frequency corresponding to the maximum growth rate, f_{max} , vs. N_{Ba}^+/N_p for the case $N_p = 8 \text{ cm}^{-3}$, $N_e^c = 0$. The angle, θ , for this plot is the one which corresponds to the peak value of γ_{max} .



N_{Ba^+}/N_p , BARIUM TO PROTON DENSITY RATIO

Figure 24

Figure 25. The same plots as in Figure 24 for $N_e^c = N_{Ba}^+$.

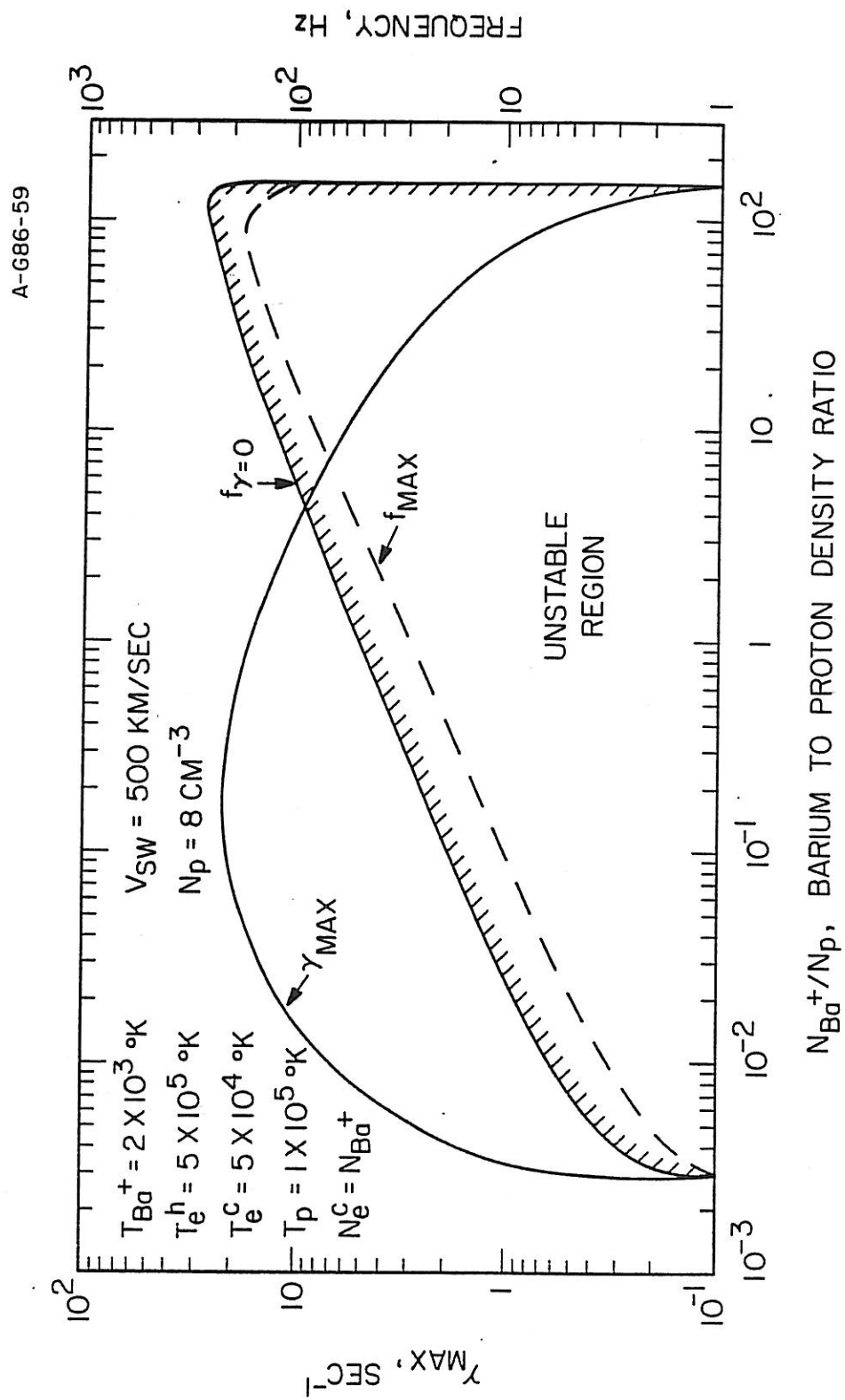


Figure 25

Figure 26. Titan and its environment during Voyager 1 flyby. Magnetospheric plasma flows around Titan. Voyager 1 trajectory, projected in the Saturnian equatorial plane, is shown. The sheath noise was observed in the cross-hatched region.

A-685-517

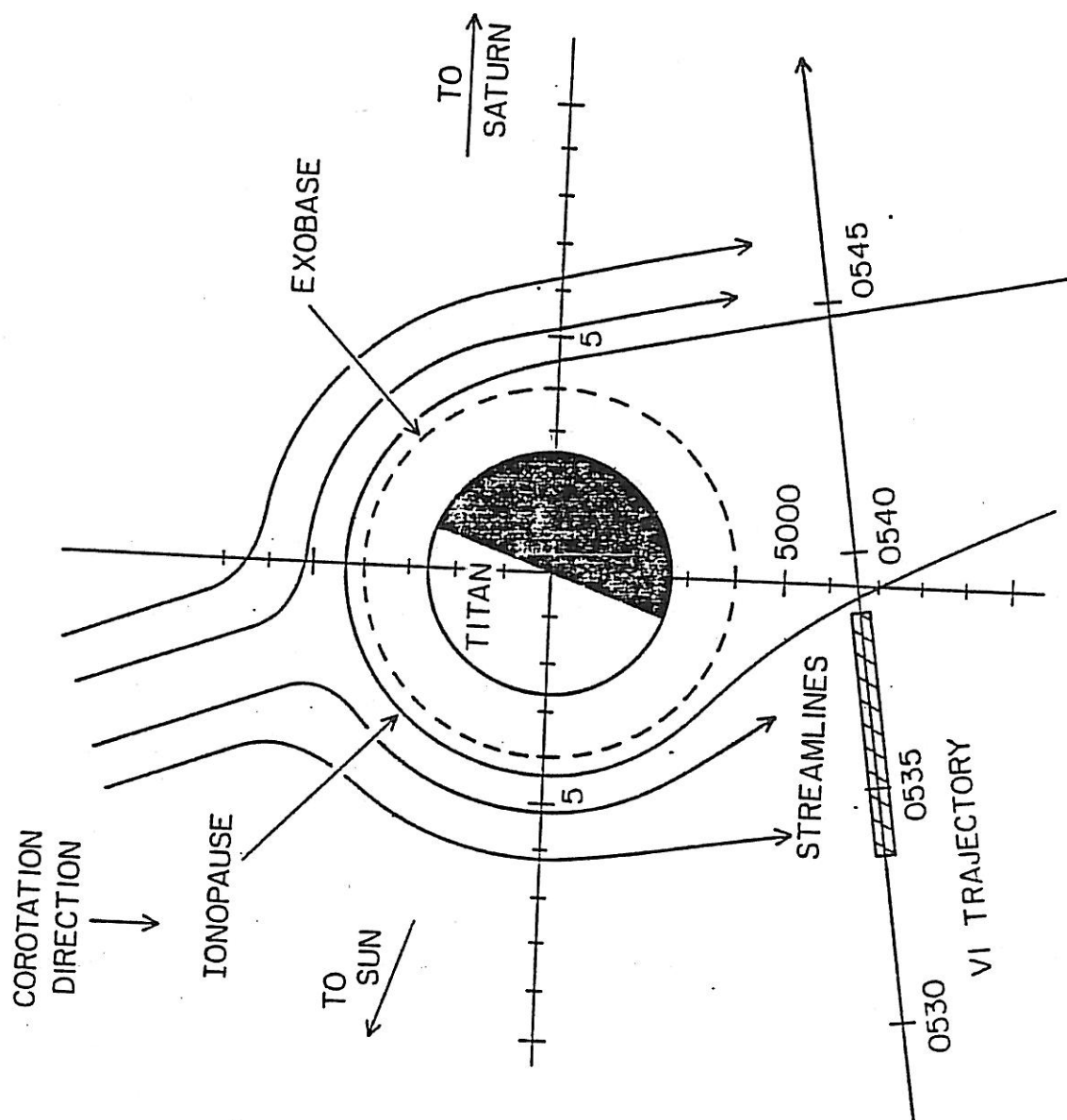


Figure 26

Figure 27. Upper panel shows the plasma density along the Voyager 1 trajectory. The dashed line indicates the plasma density level of the magnetosphere near Titan's orbit, which is 0.3 cm^{-3} . The lower panel shows the electric field intensities. The sheath noise occurs from 0532:30 to 0538:30 SCET.

A-G85-597

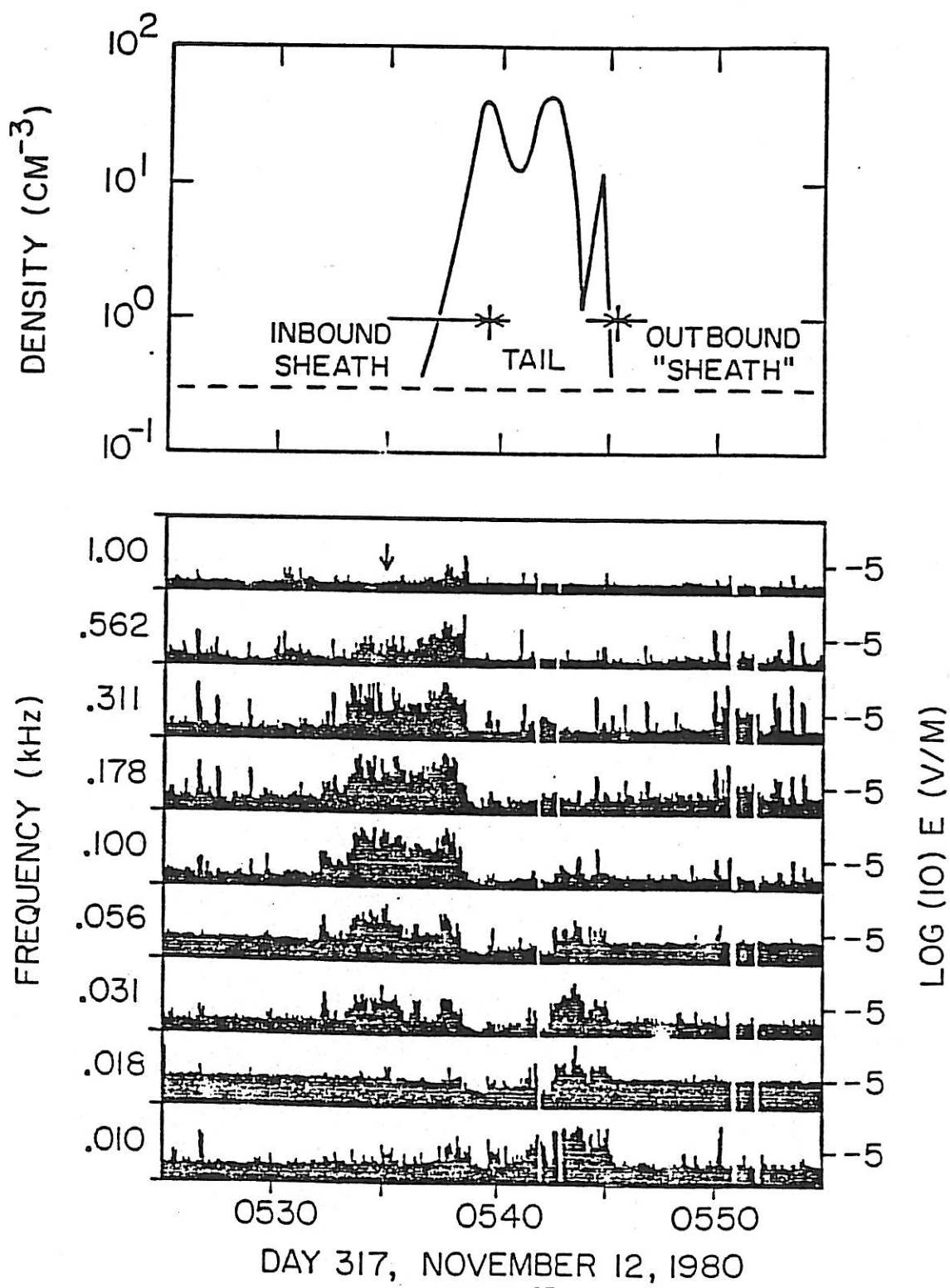


Figure 28. A spectrum of the sheath noise at the time
0535:35 SCET, as marked by an arrow in Figure 27.

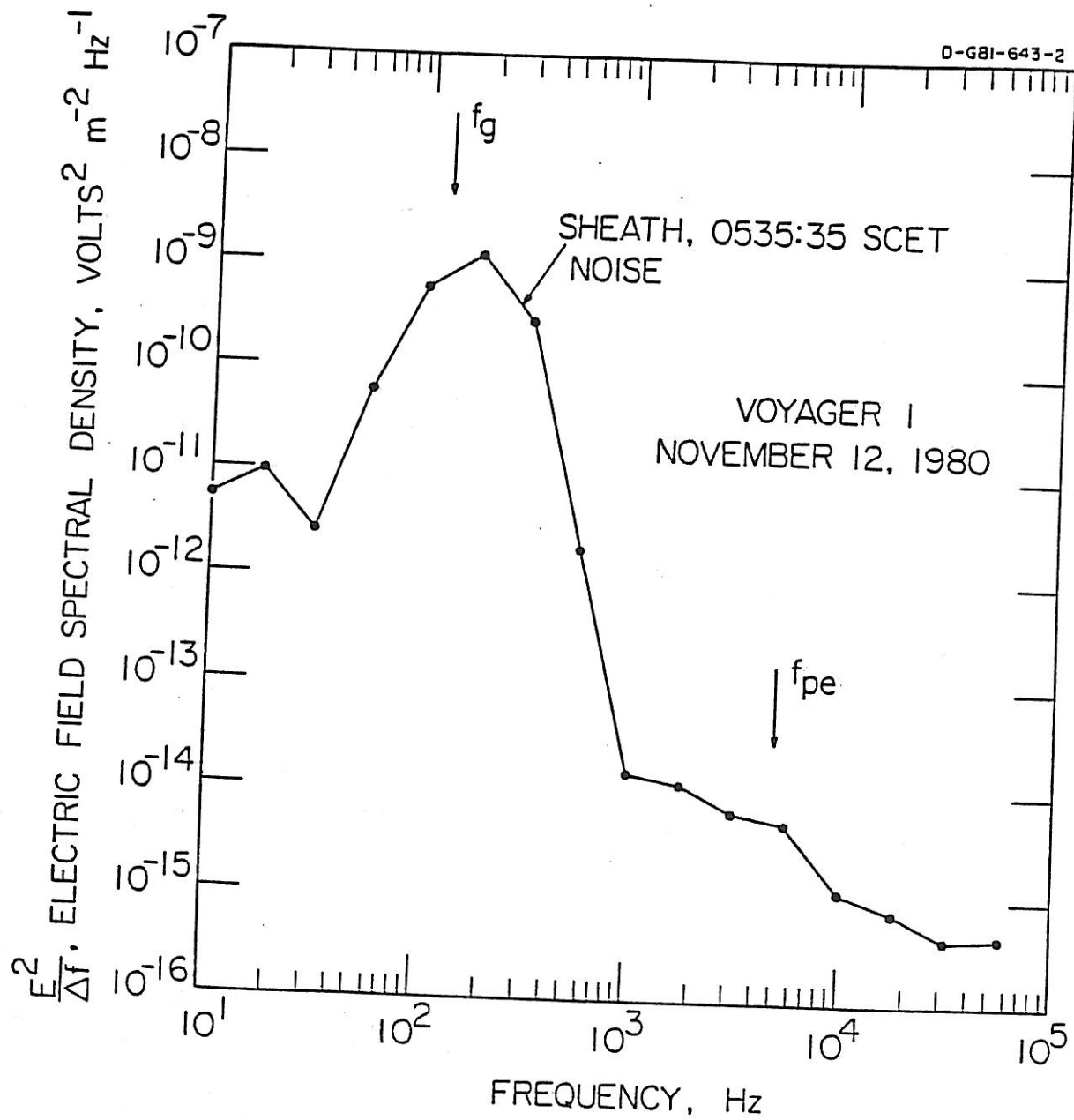


Figure 28

Figure 29. Radial density distribution of Titan's exosphere,
normalized by the density of H at the exobase, N_0
[Hartle et al., 1982].

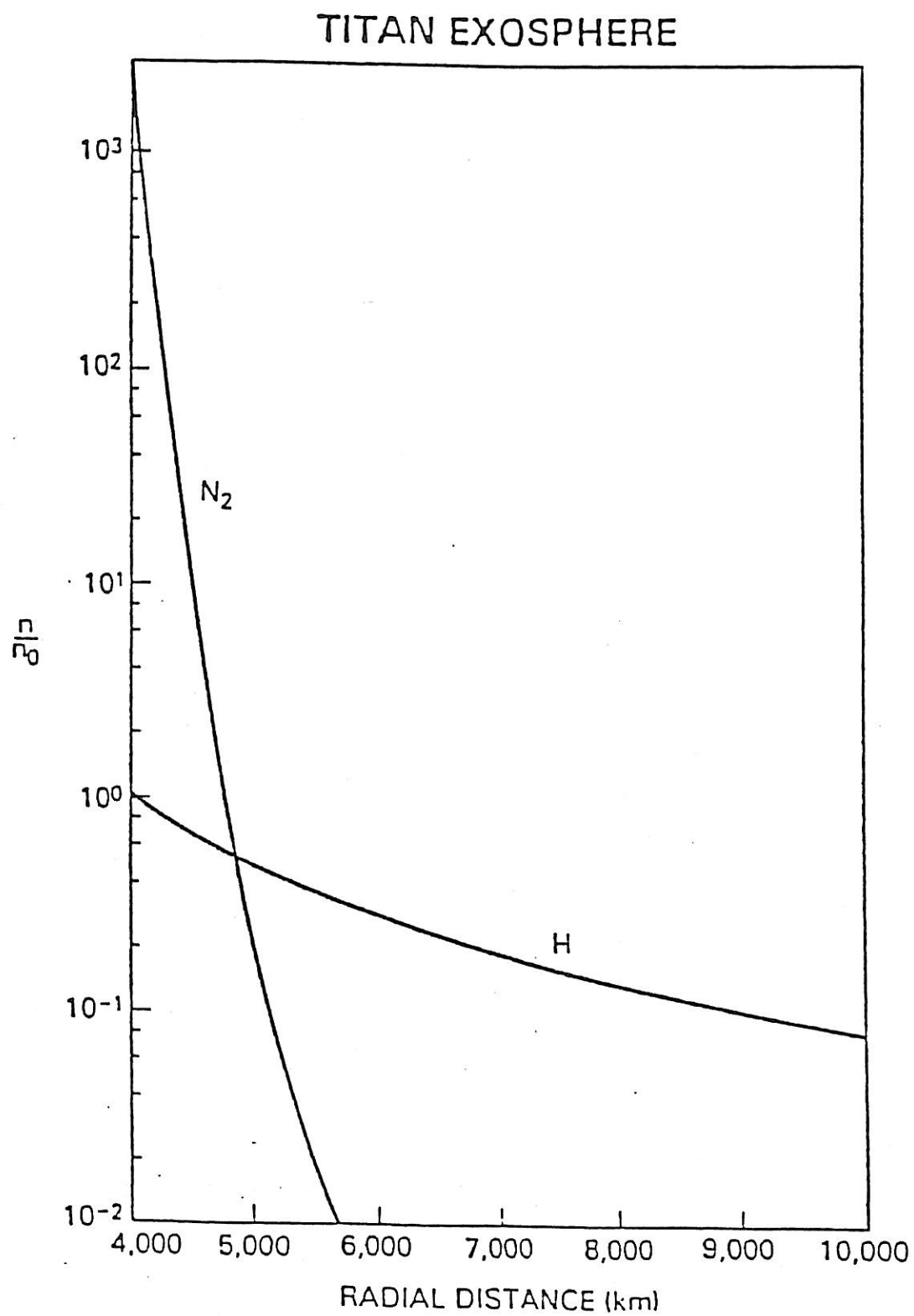


Figure 29

Figure 30. A model for analyzing an ion beam-plasma instability. N^+ and H^+ in the corotational magnetoplasma flow with speed V_m , and electrons (hot and cold) drift with speed, V_D , the newly created ions, N^+ and H^+ , are nearly stationary.

A-685-516-3

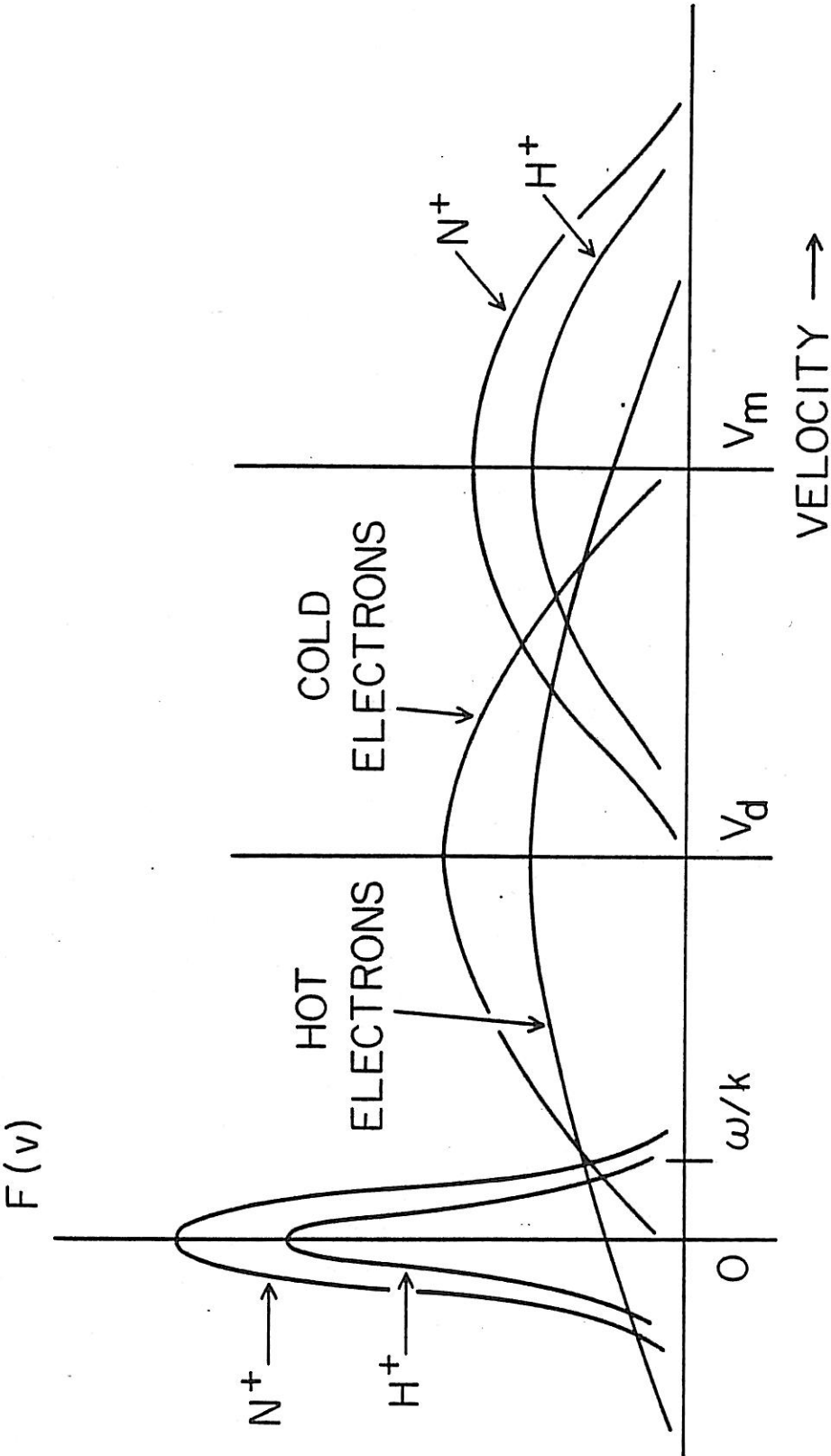


Figure 30

Figure 31. A plot of the growth rate, γ , versus frequency (bottom panel) and $k\lambda_D$, the wave number normalized by the Debye length versus frequency, $\lambda_D = 0.77$ m, $N_s = 5$ $N_b = 1.5$ cm⁻³, $N_{ns} = N_{ps}$ and $N_e^c = 0$.

A-G85-969-1

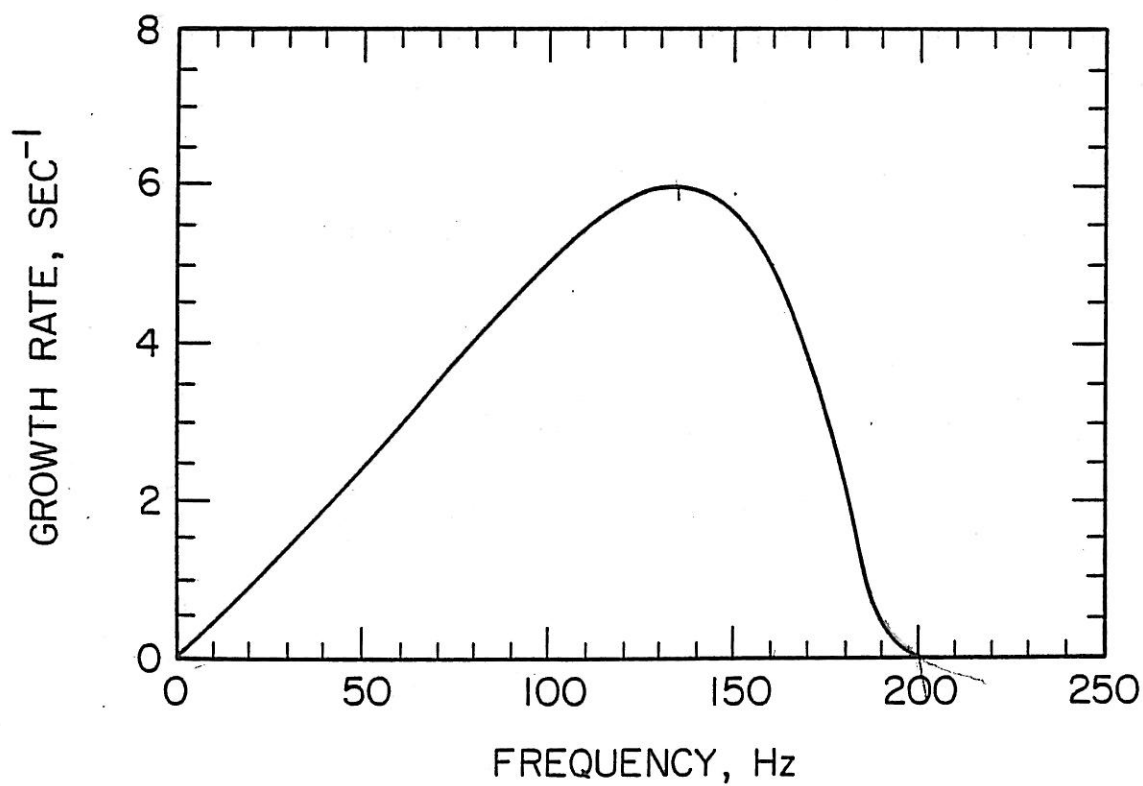
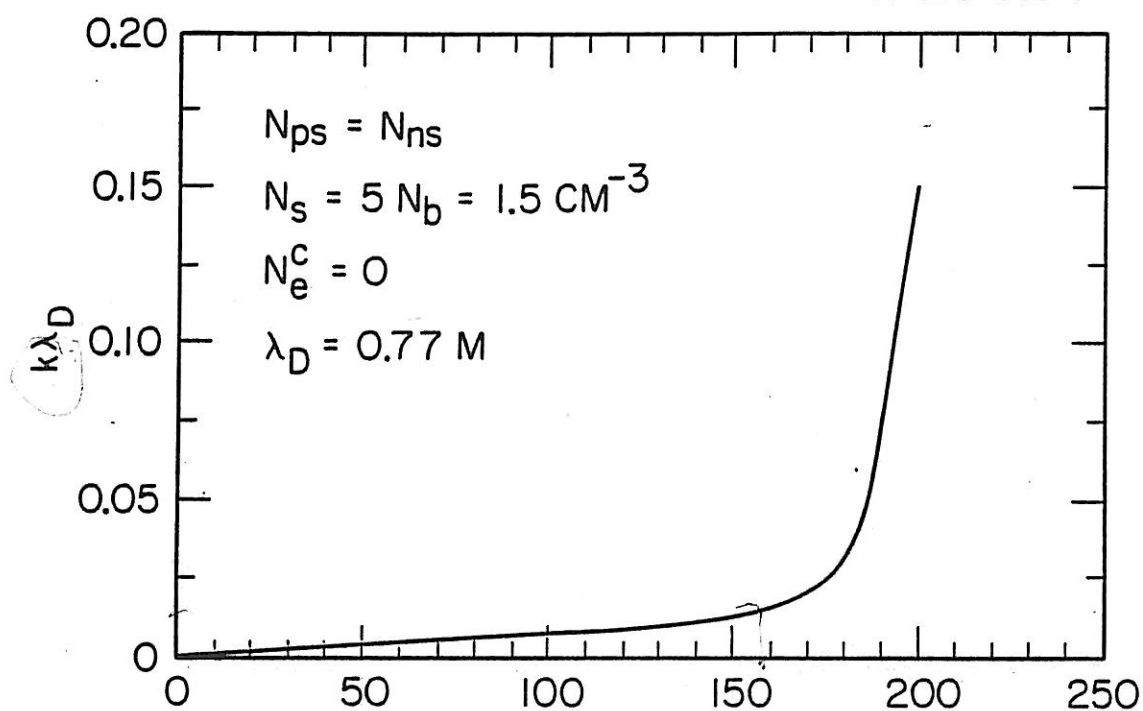


Figure 31

Figure 32. A plot of maximum growth rates, γ_{\max} , as functions of θ for the case $N_{ns} = N_{ps}$, $N_s = N_b$. The solid curve is for the case of absence of cold electrons and the dashed curve is for the case $N_e^c = N_s$.

B-G86-30

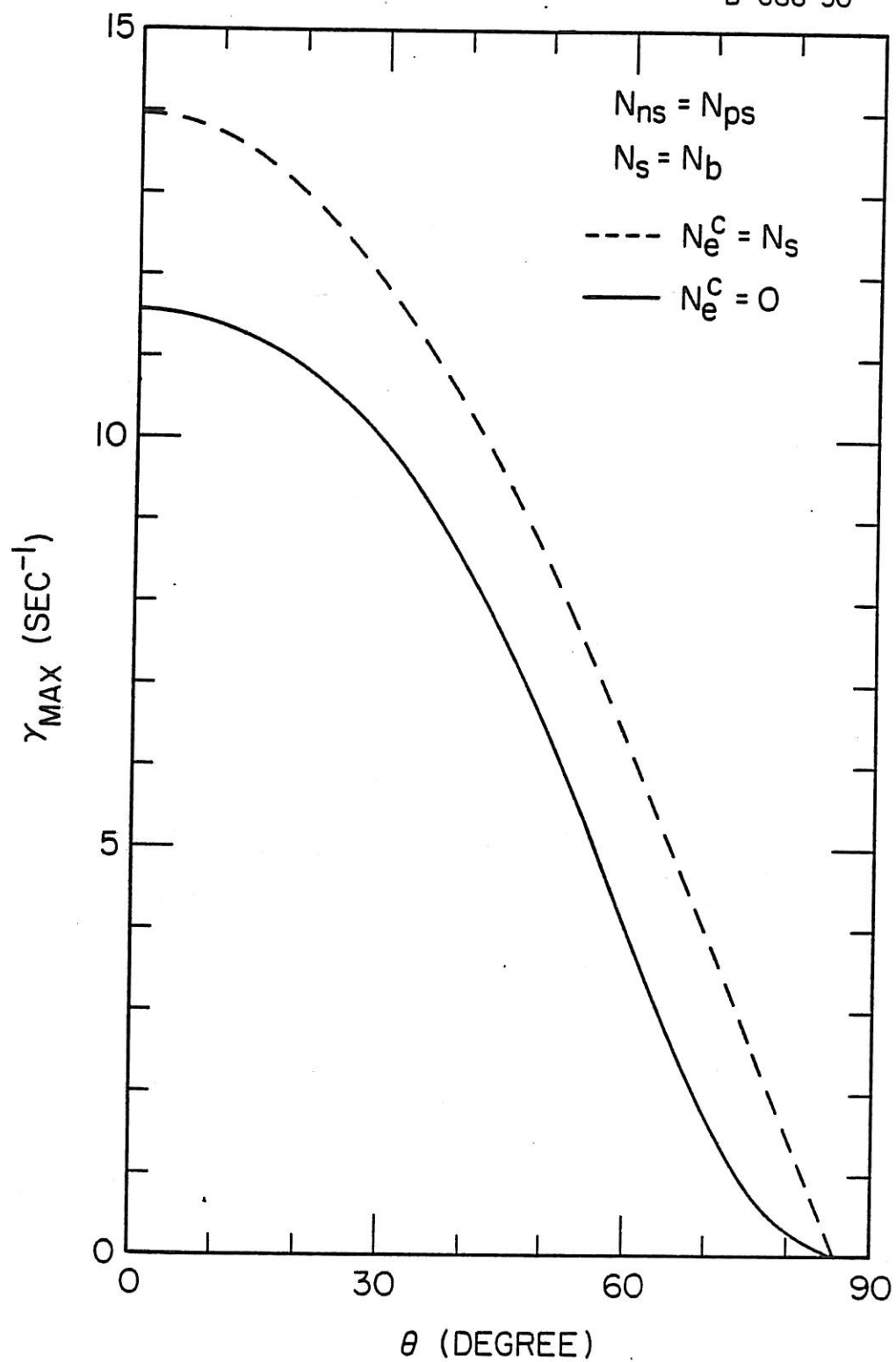


Figure 32

Figure 33. A plot of frequency for the marginal instability vs. the density ratio, N_s/N_b , for the case, $N_{ns} = N_{ps}$, $T_e^c = T_e^h = 200$ eV. The frequency corresponding to the maximum growth rate, γ_{max} , is plotted by the dashed curve.

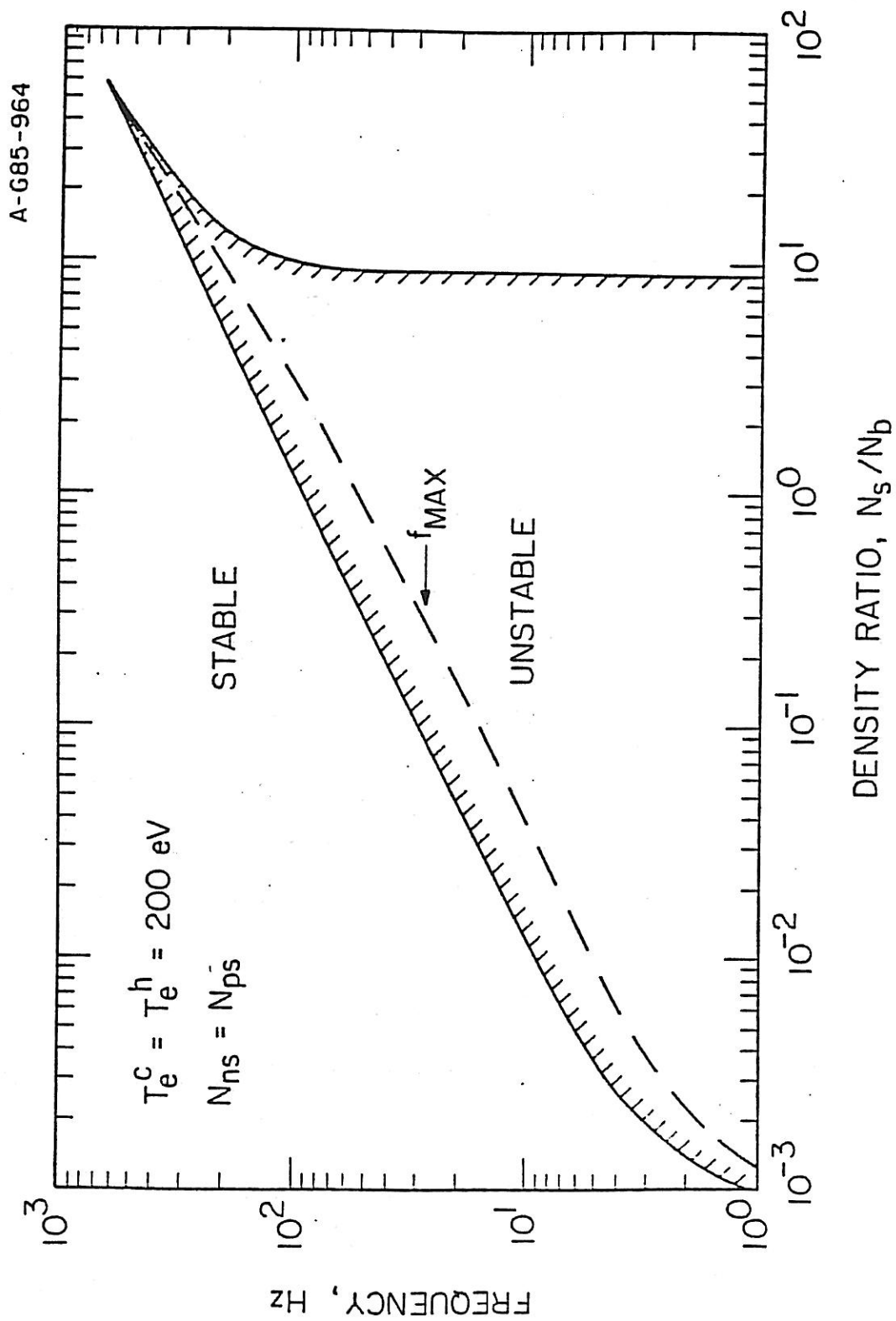


Figure 33

Figure 34. The same plot as Figure 33 for the case $T_e^c =$
2 eV.

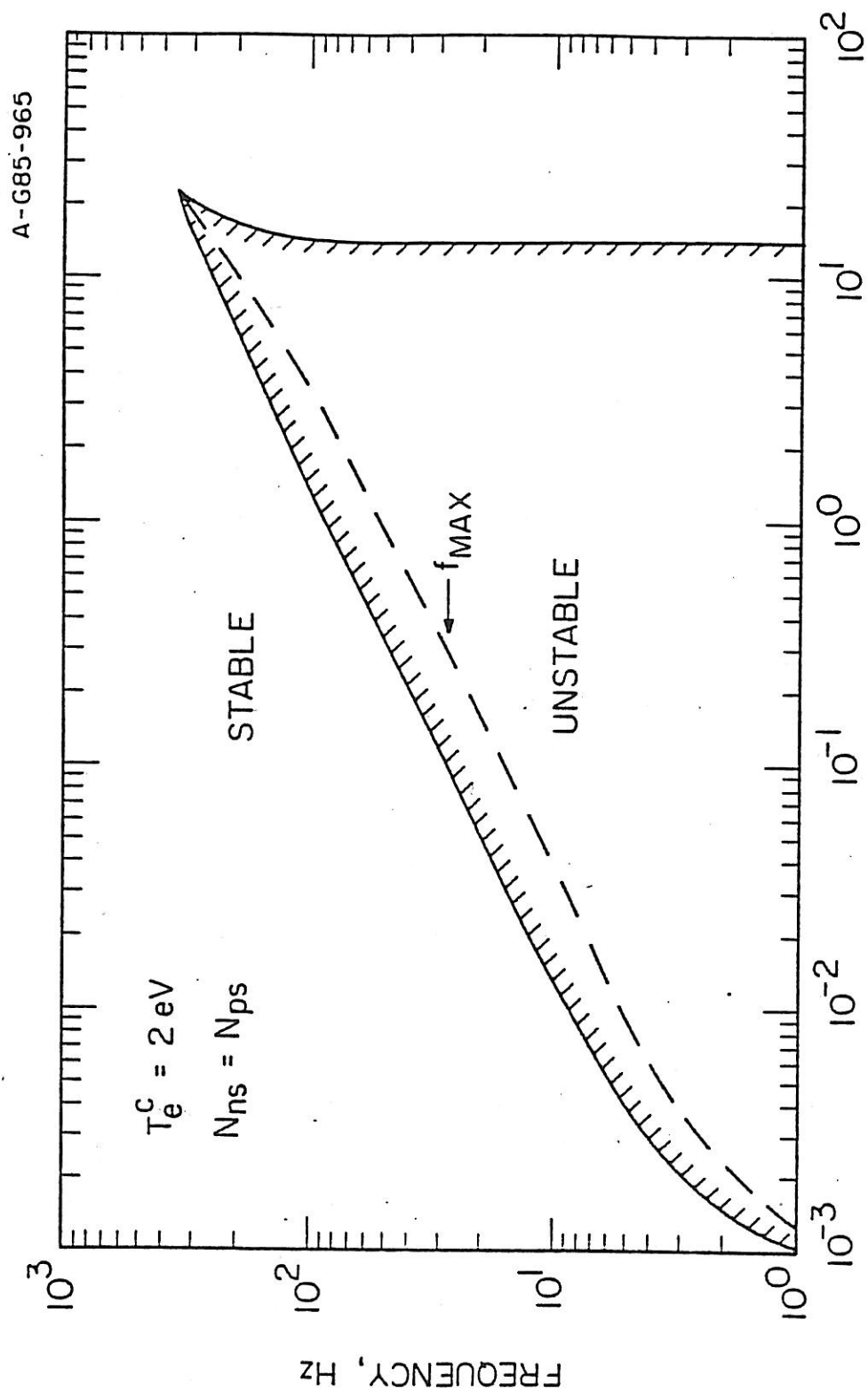


Figure 34

Figure 35. The plot of maximum growth rate vs. N_S/N_D in the same condition of Figure 33.

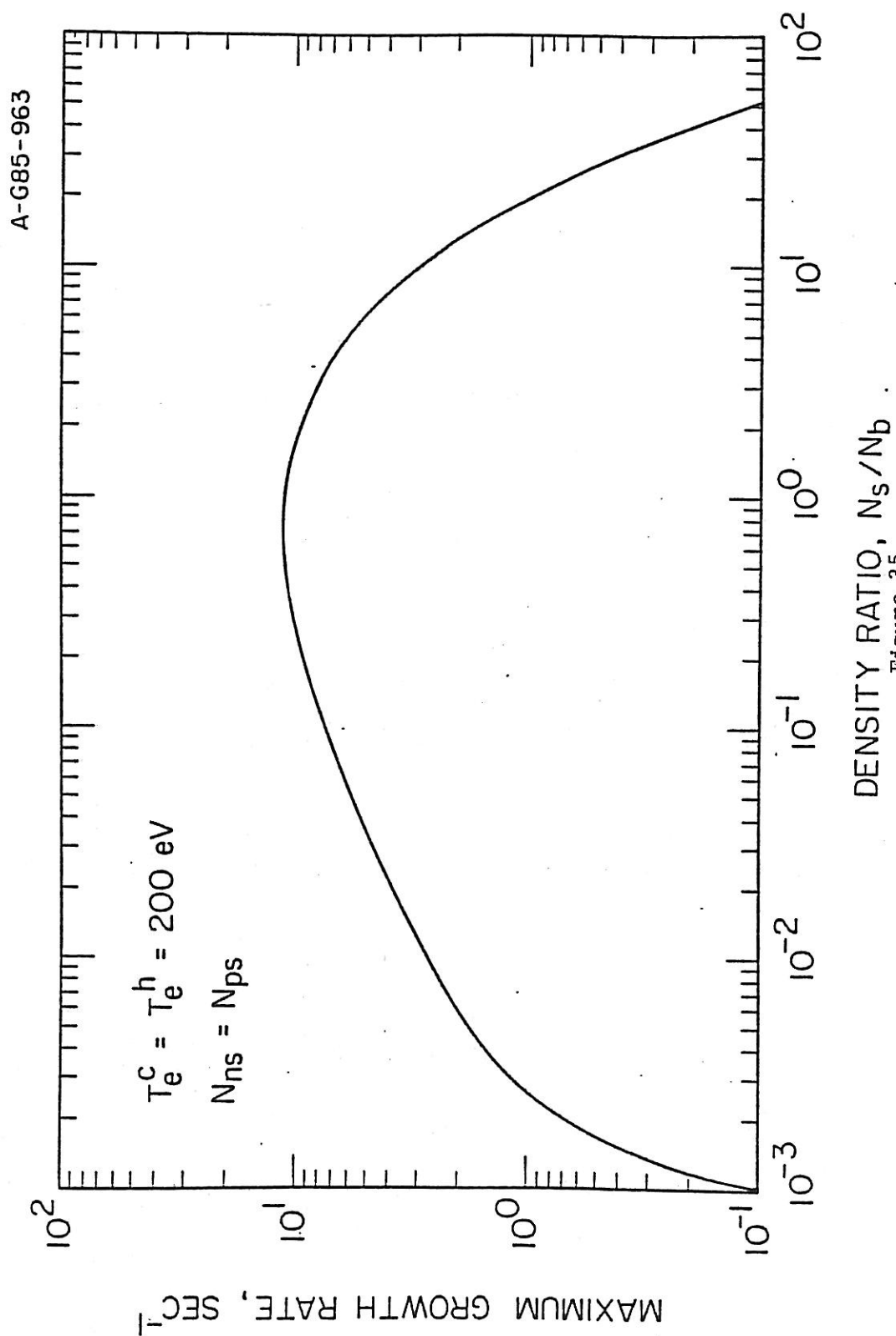


Figure 36. The same plot as Figure 35 for the case $T_e^c =$
2 eV.

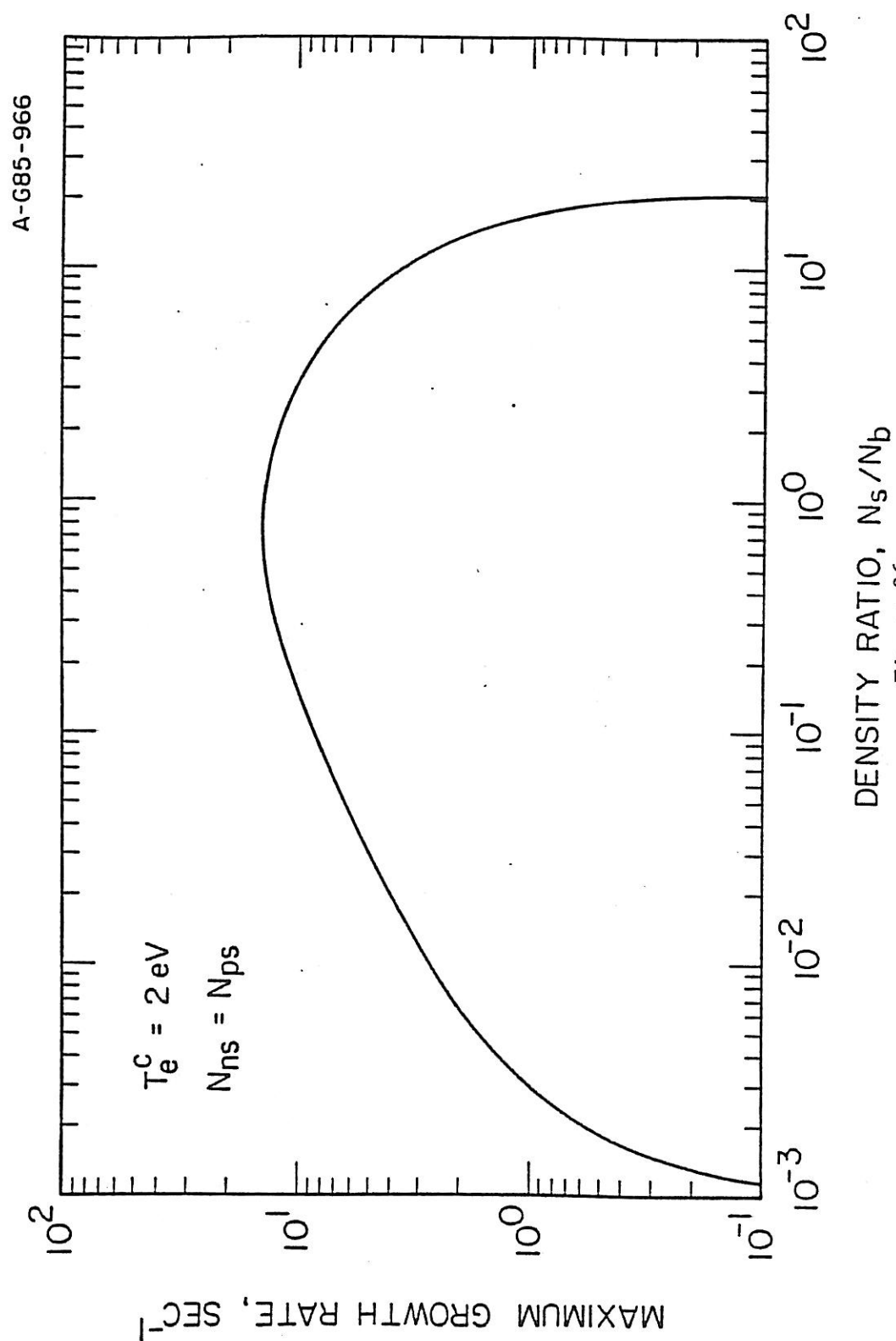


Figure 37. A plot of frequency for the marginal instability
vs. N_s/N_b for the case $T_e^c = T_e^h = 200$ eV, $N_{ns} =$
 $2 N_{ps}$.

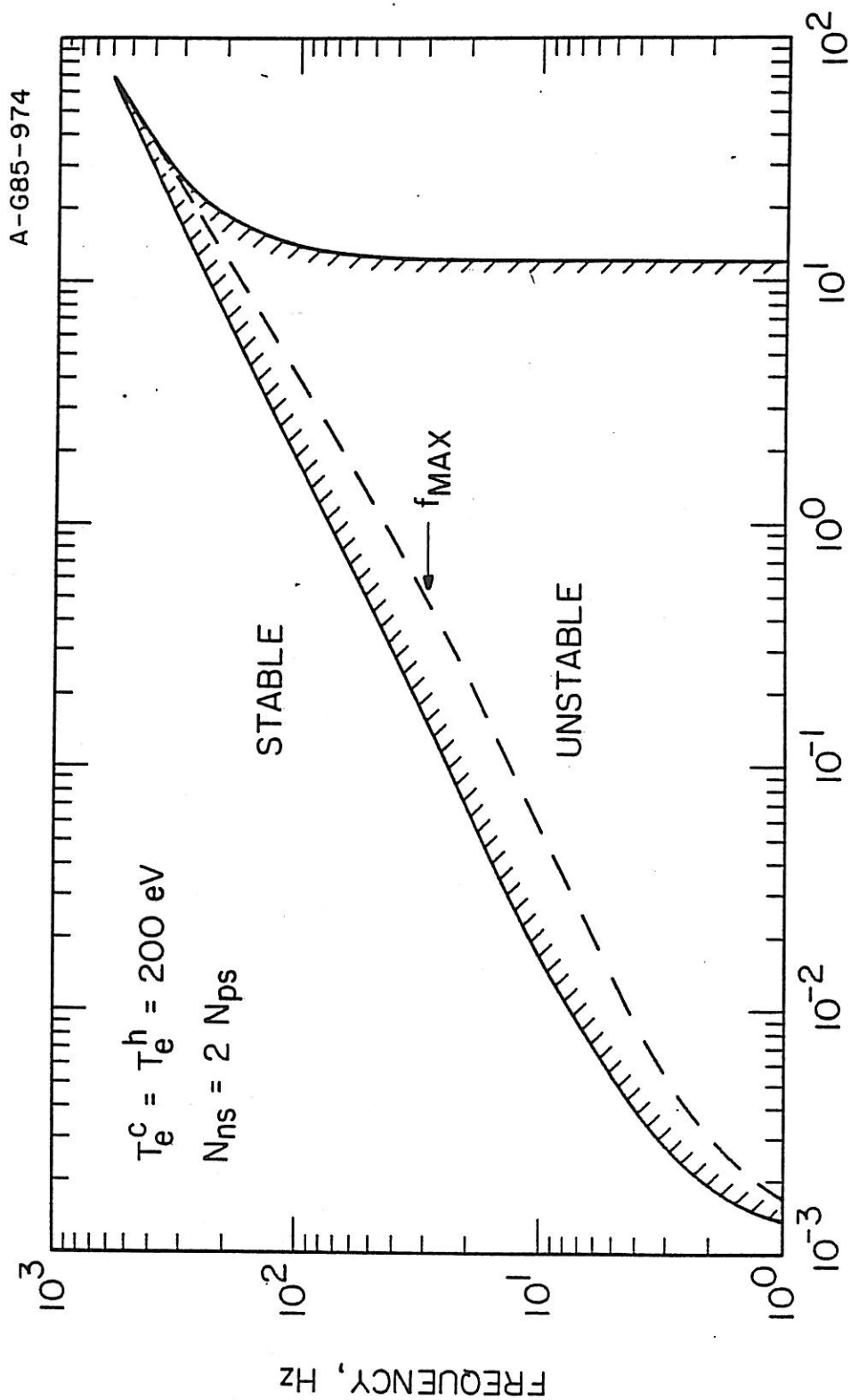


Figure 37

Figure 38. A plot of γ_{\max} vs. N_s/N_b for the case $T_e^c = T_e^h =$
200 eV, $N_{ns} = 2 N_{ps}$.

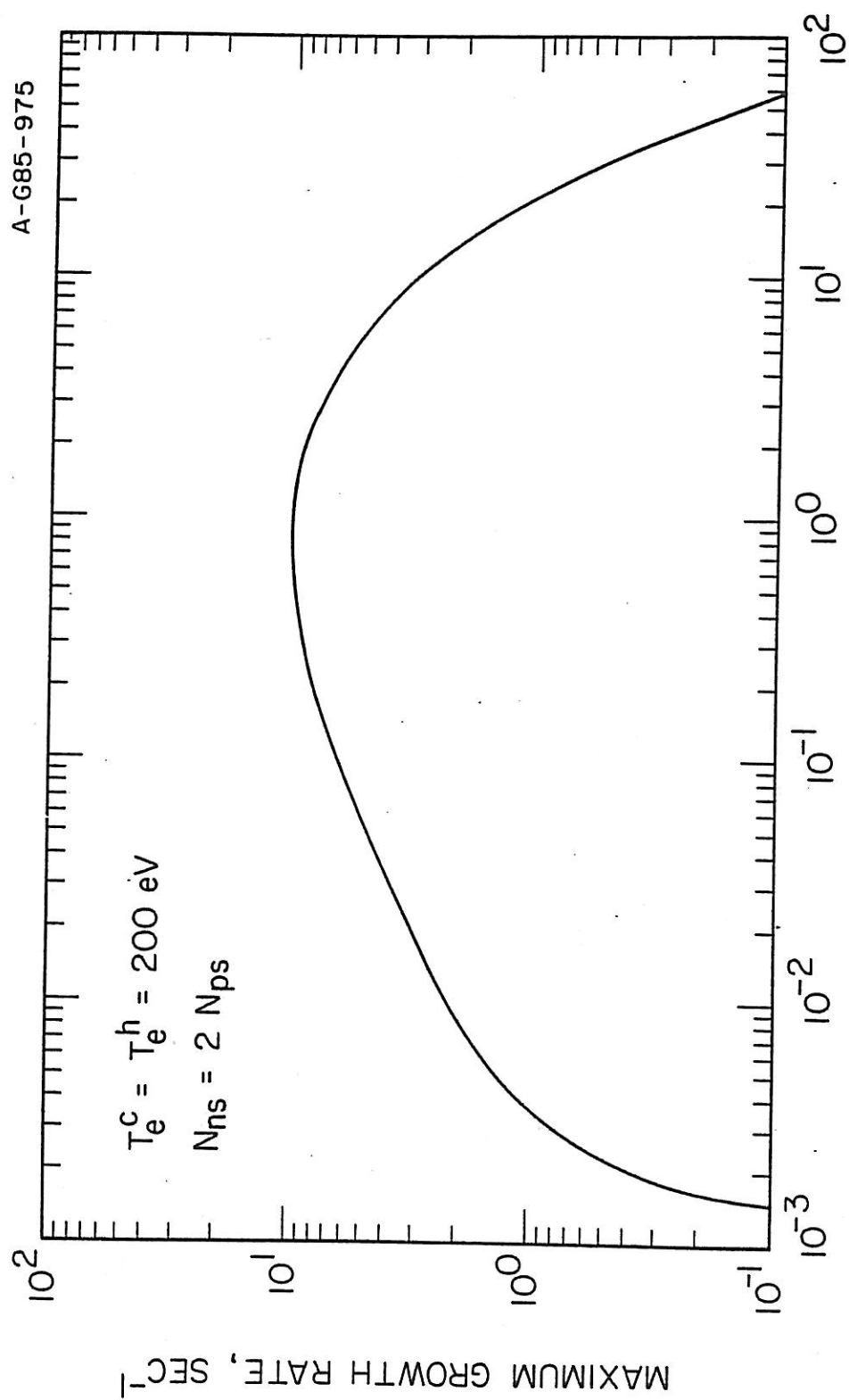


Figure 38

Figure 39. The same plot as in Figure 37 for the case $N_{ns} = 0.5 N_{ps}$.

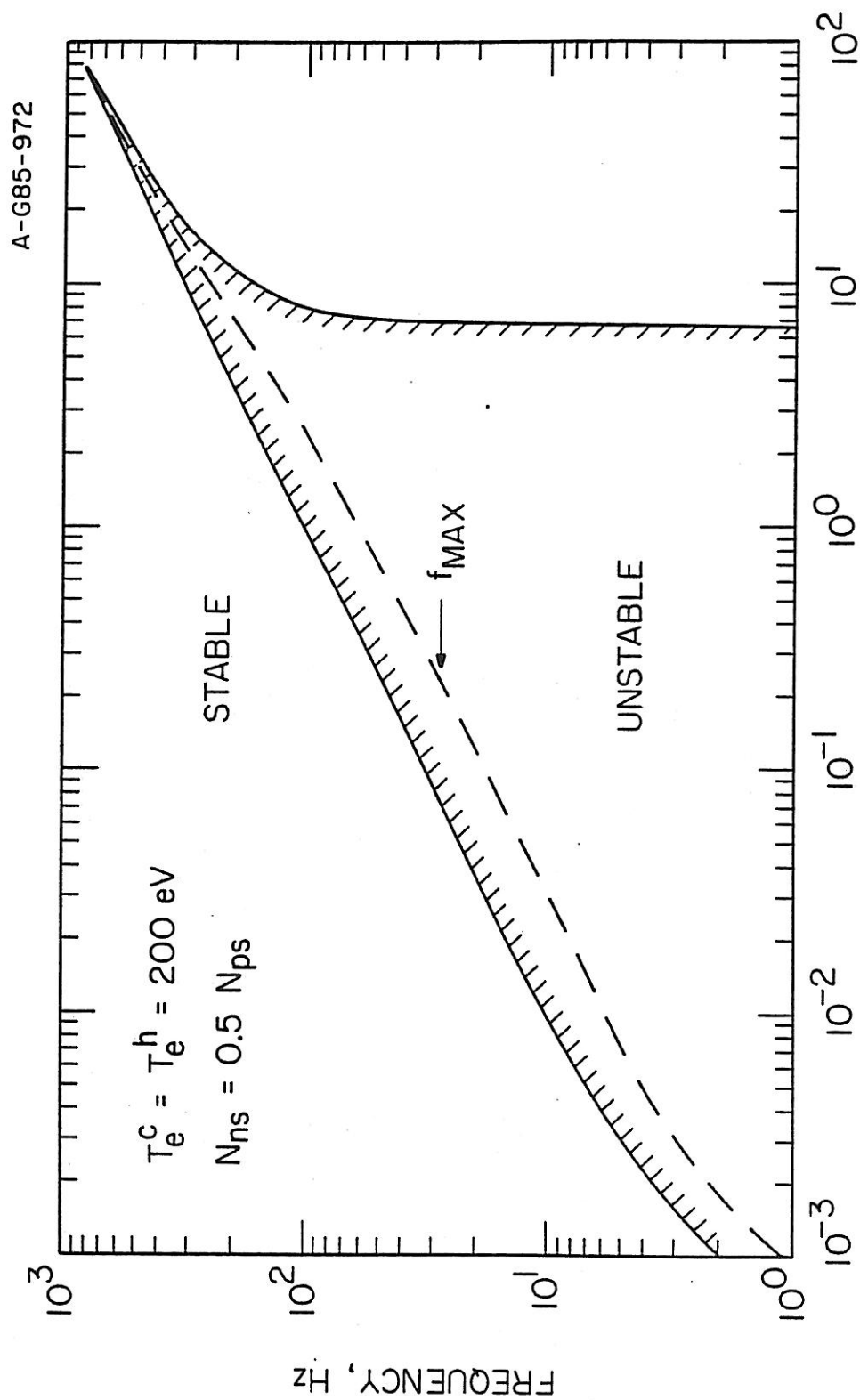


Figure 39

Figure 40. The same plot as in Figure 38 for the case $N_{ns} = 0.5 N_{ps}$.

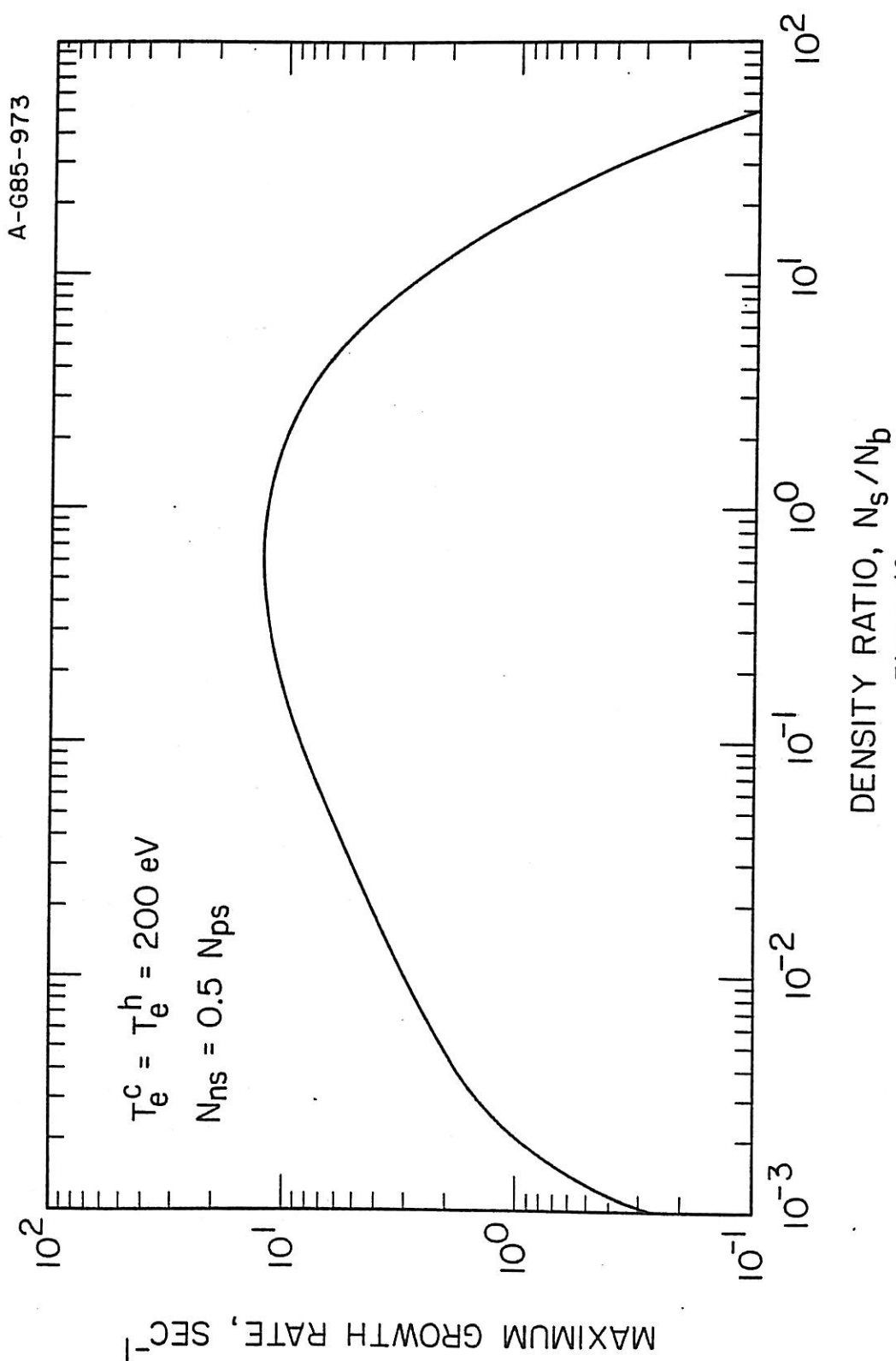


Figure 41. A plot of the frequency for the marginal instability vs. N_s/N_b for the case $T_e^c = 2$ eV, $N_e^c = N_s$ and $N_{ns} = 2 N_{ps}$.

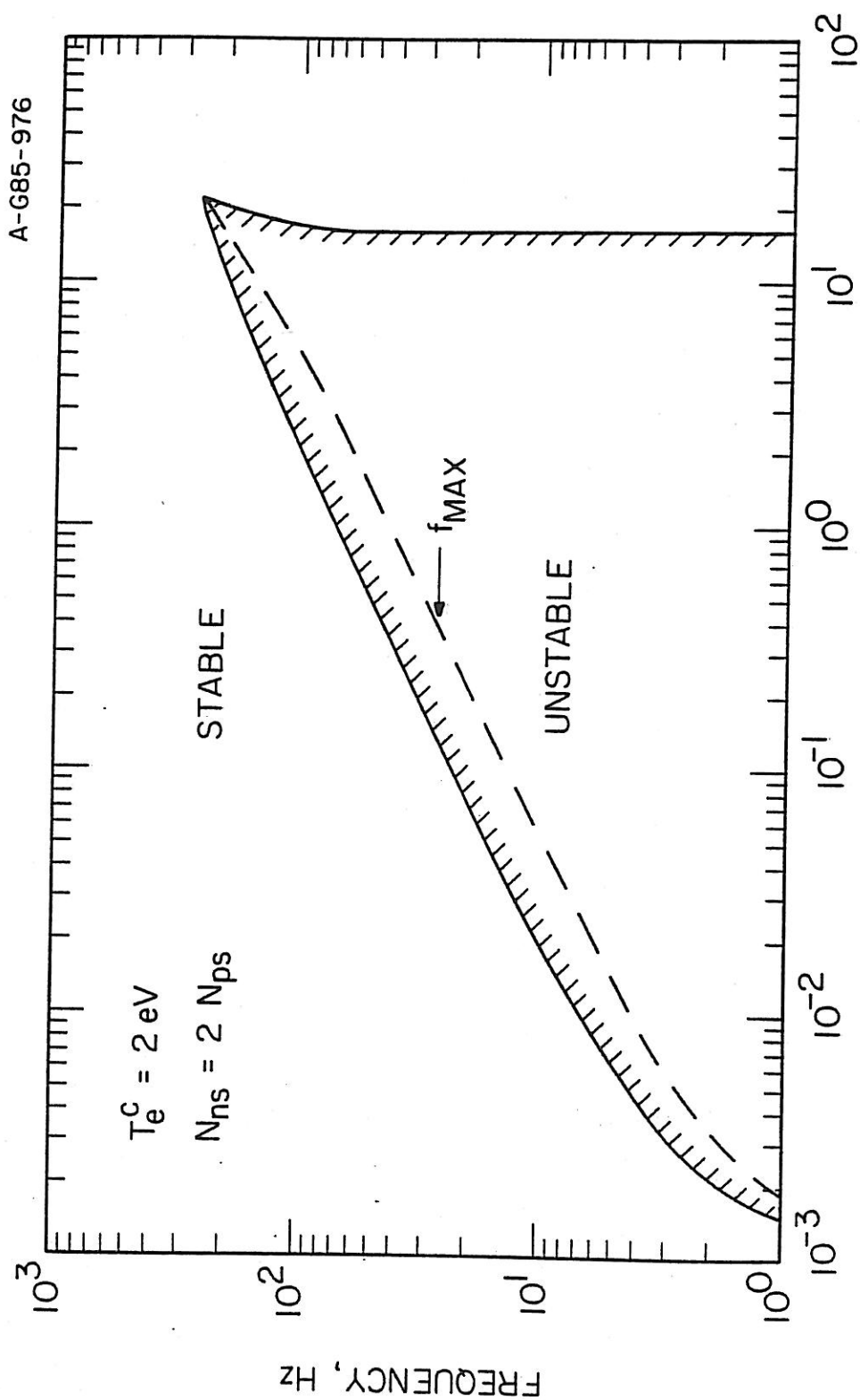


Figure 41

Figure 42. A plot of γ_{\max} vs. N_S/N_D for the case $T_e^c = 2$ eV,
 $N_e^c = N_S$ and $N_{ns} = 2 N_{ps}$.

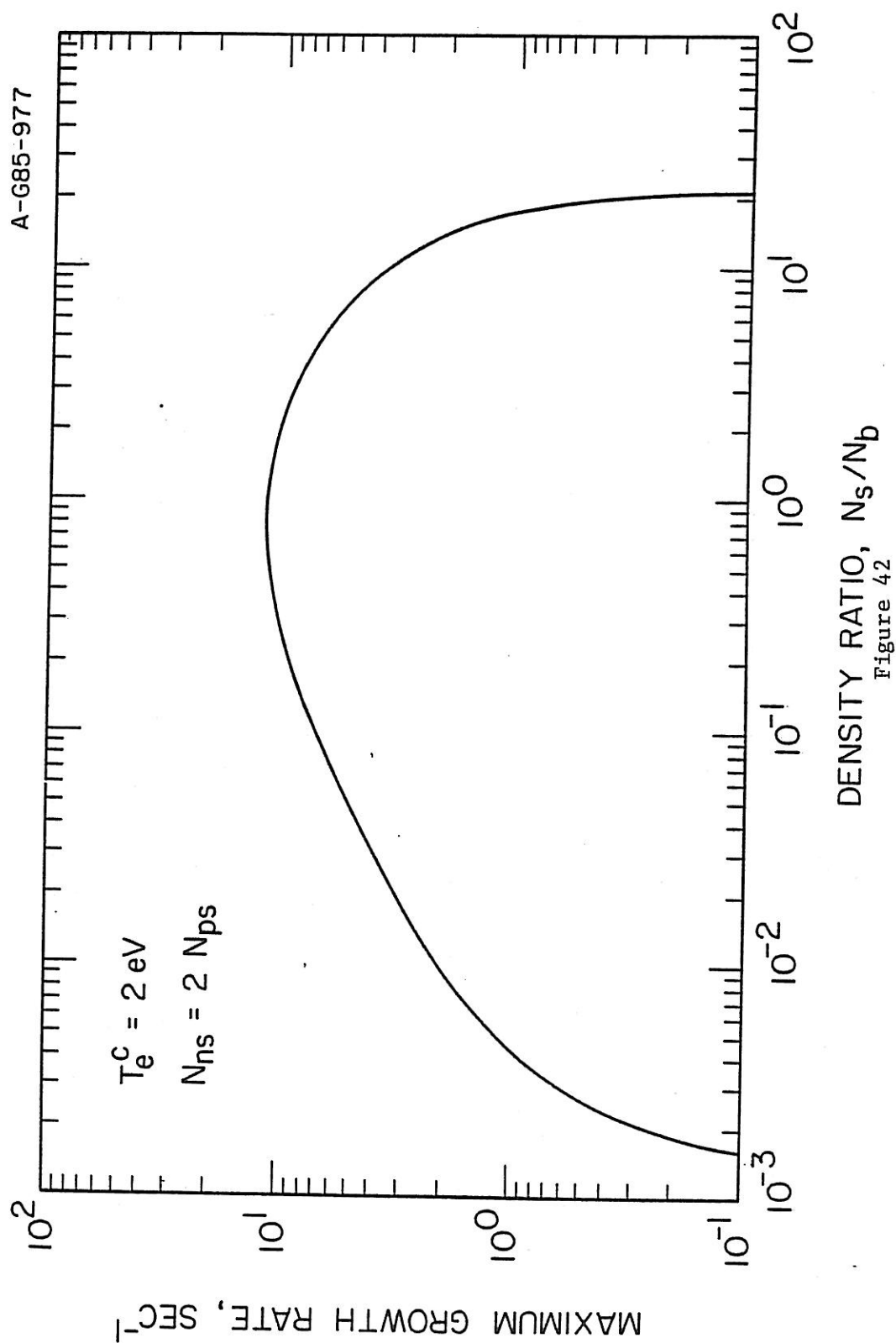


Figure 43. The same plot as in Figure 41 for the case $N_{ns} = 0.5 N_{ps}$.

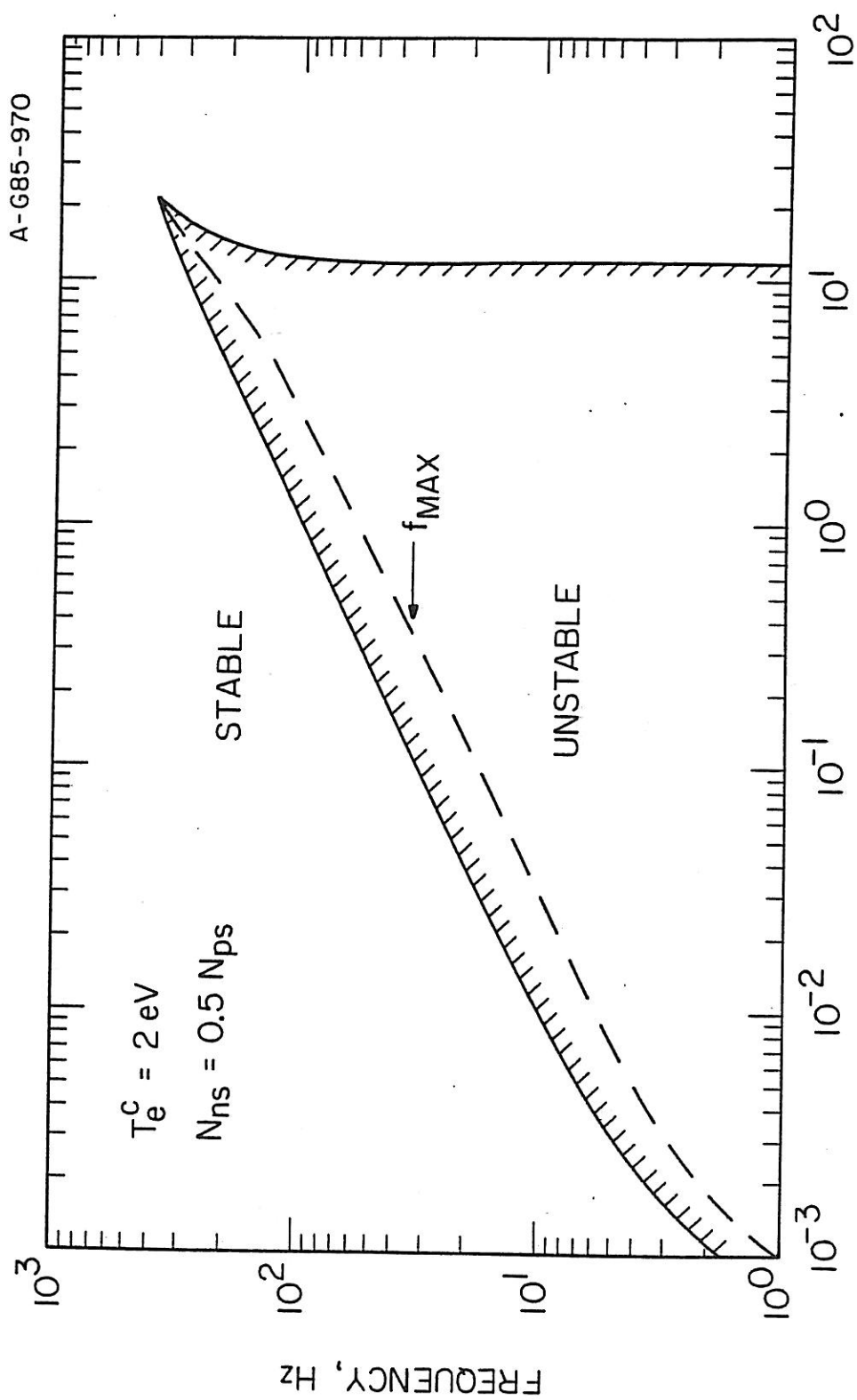


Figure 43

Figure 44. The same plot as in Figure 42 for the case $N_{ns} = 0.5 N_{ps}$.

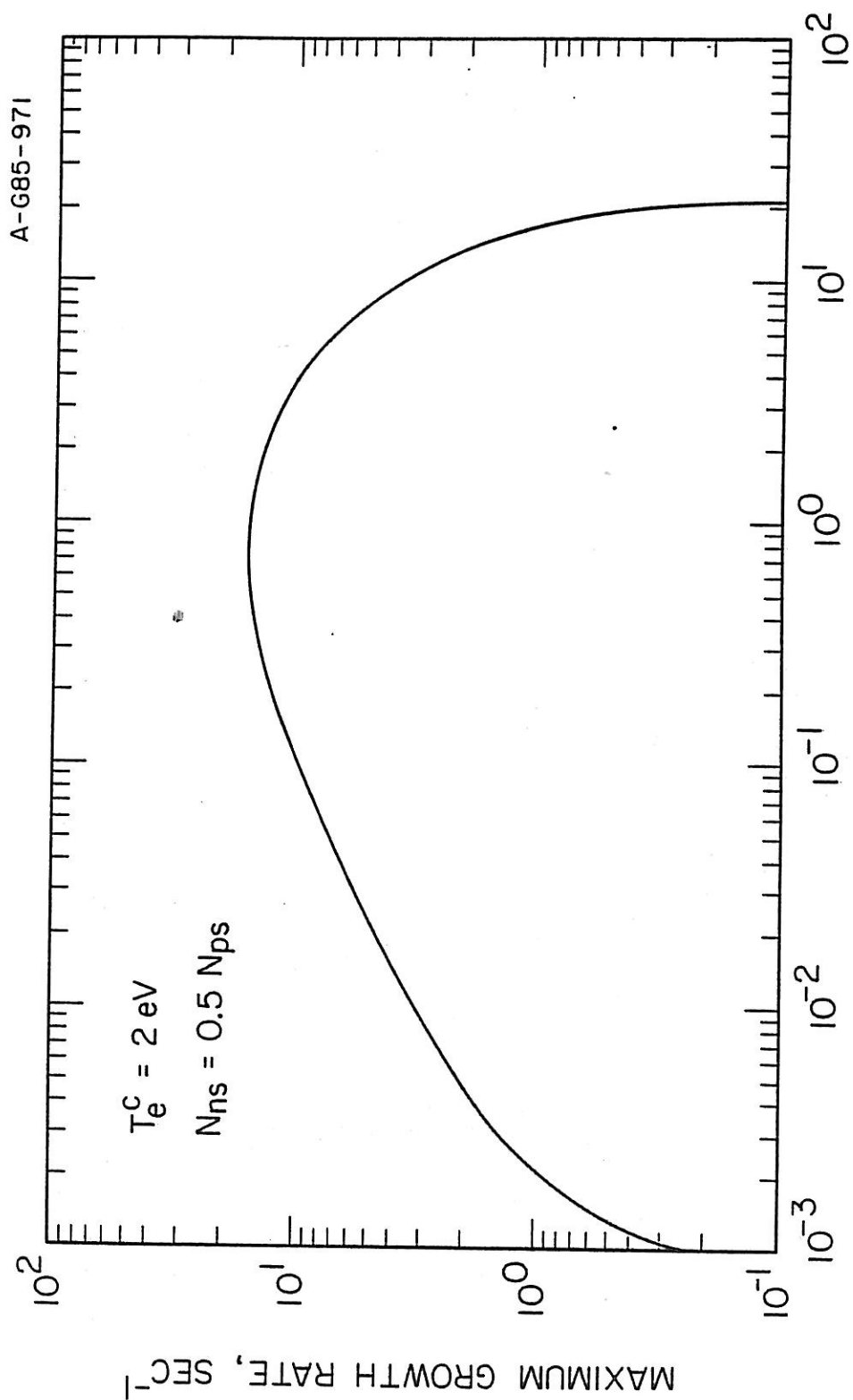


Figure 44

Figure 45. An illustration to the ion gyrations in the sheath. Ions escaped away from the exosphere on the inbound side and were absorbed by the exosphere on the outbound side.

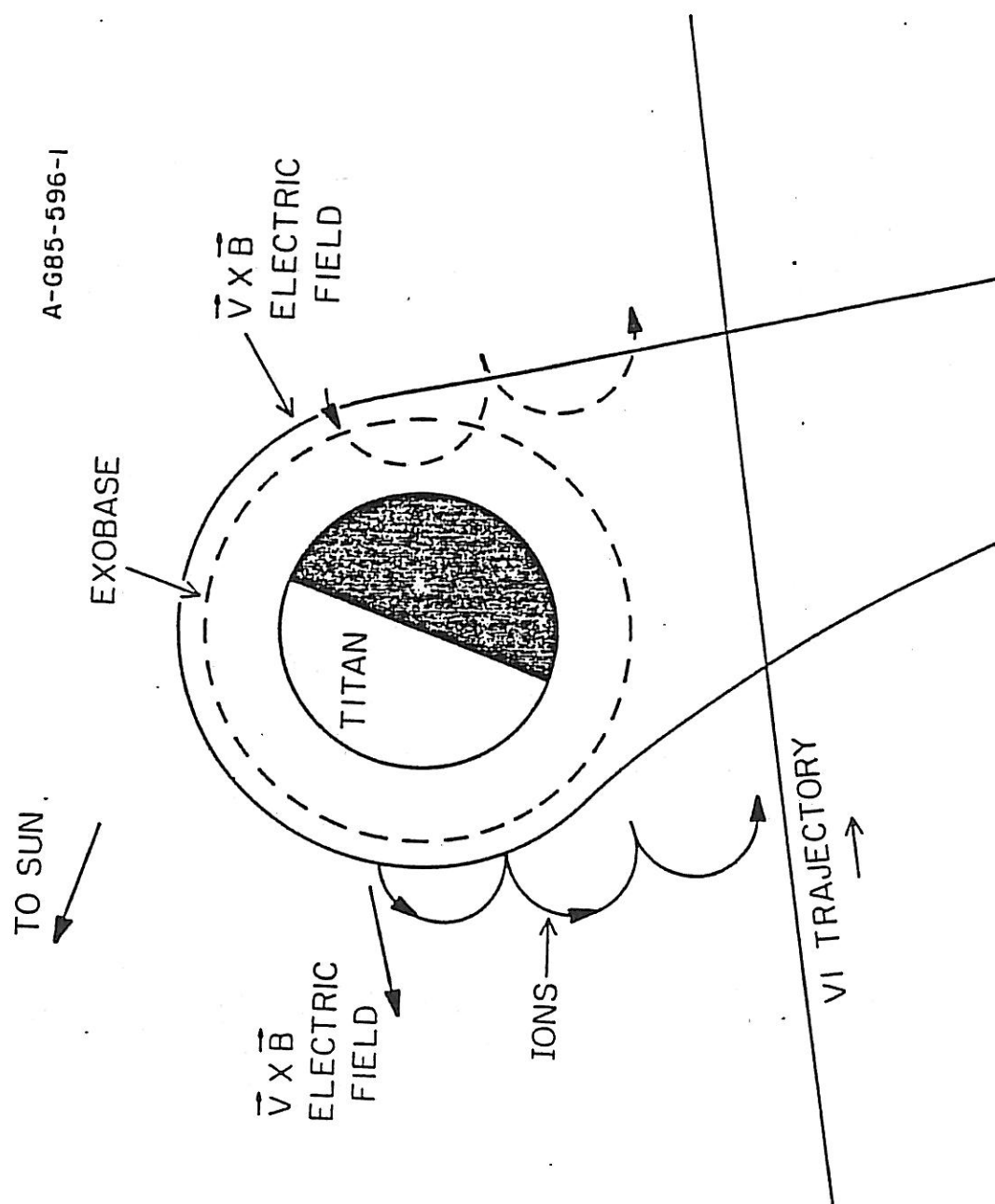


Figure 45

Figure 46. The particle simulation result for the AMPTE lithium release. Plots of field energy and particle energies vs. time for $N_{Li} = N_p$, $\theta = 85^\circ$.

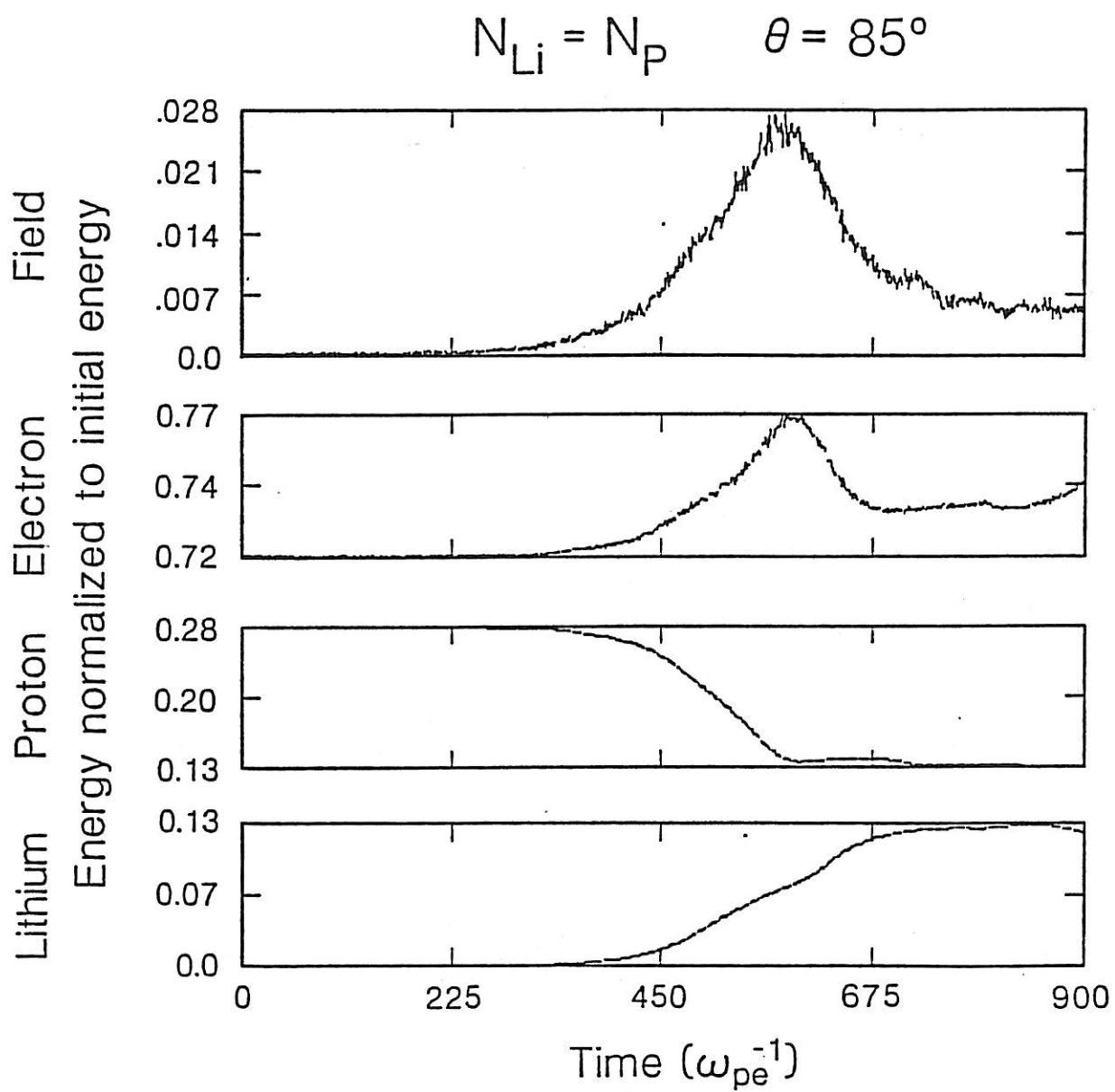


Figure 46

Figure 47. Lithium ion distributions in phase space at $t = 300$
 ω_{pe}^{-1} , $500 \omega_{pe}^{-1}$ and $700 \omega_{pe}^{-1}$.

Lithium

$$N_{\text{Li}} = N_p \quad \theta = 85^\circ \quad v_{\text{Li}} = 0.26 \times 10^{-2} v_e$$

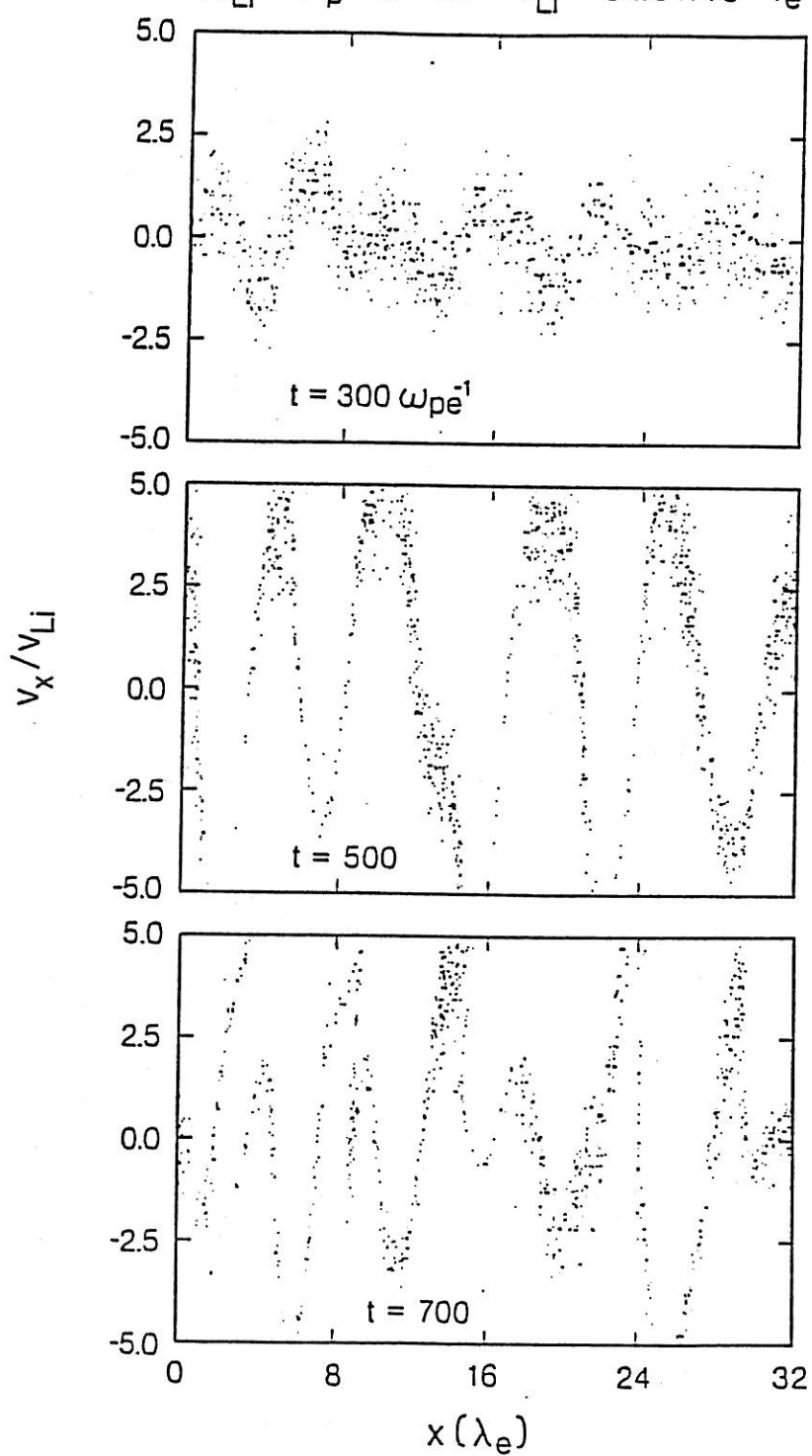


Figure 47

Figure 48. Proton distributions in phase space at $t = 300$
 ω_{pe}^{-1} , $600 \omega_{pe}^{-1}$ and $700 \omega_{pe}^{-1}$.

Protons

$$N_{Li} = N_p \quad \theta = 85^\circ \quad v_p = 0.01 v_e$$

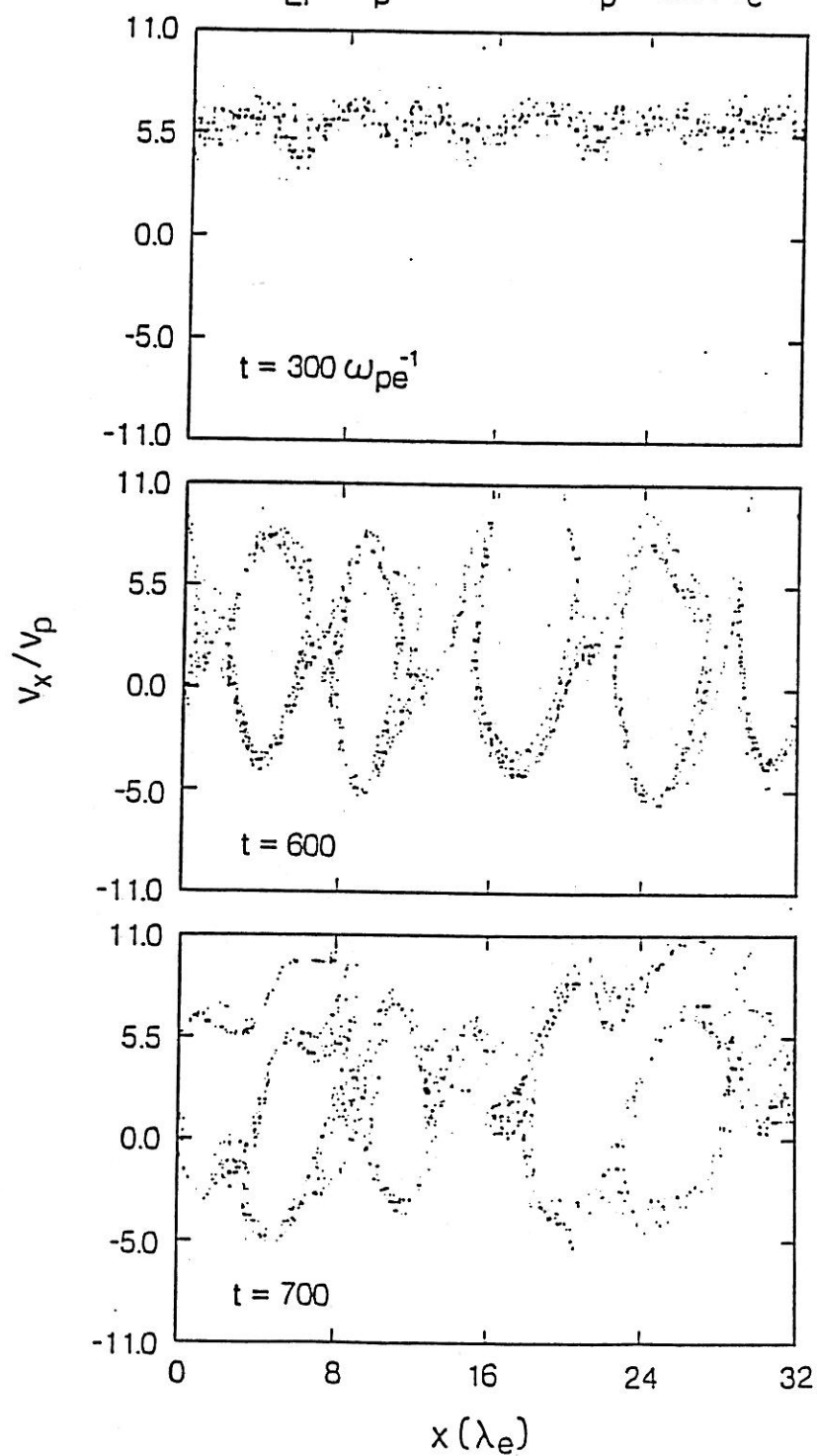


Figure 48

Figure 49. Plots of field energy and particle energies vs.
time for $N_{Li} = 0.11 N_p$, $\theta = 85^\circ$.

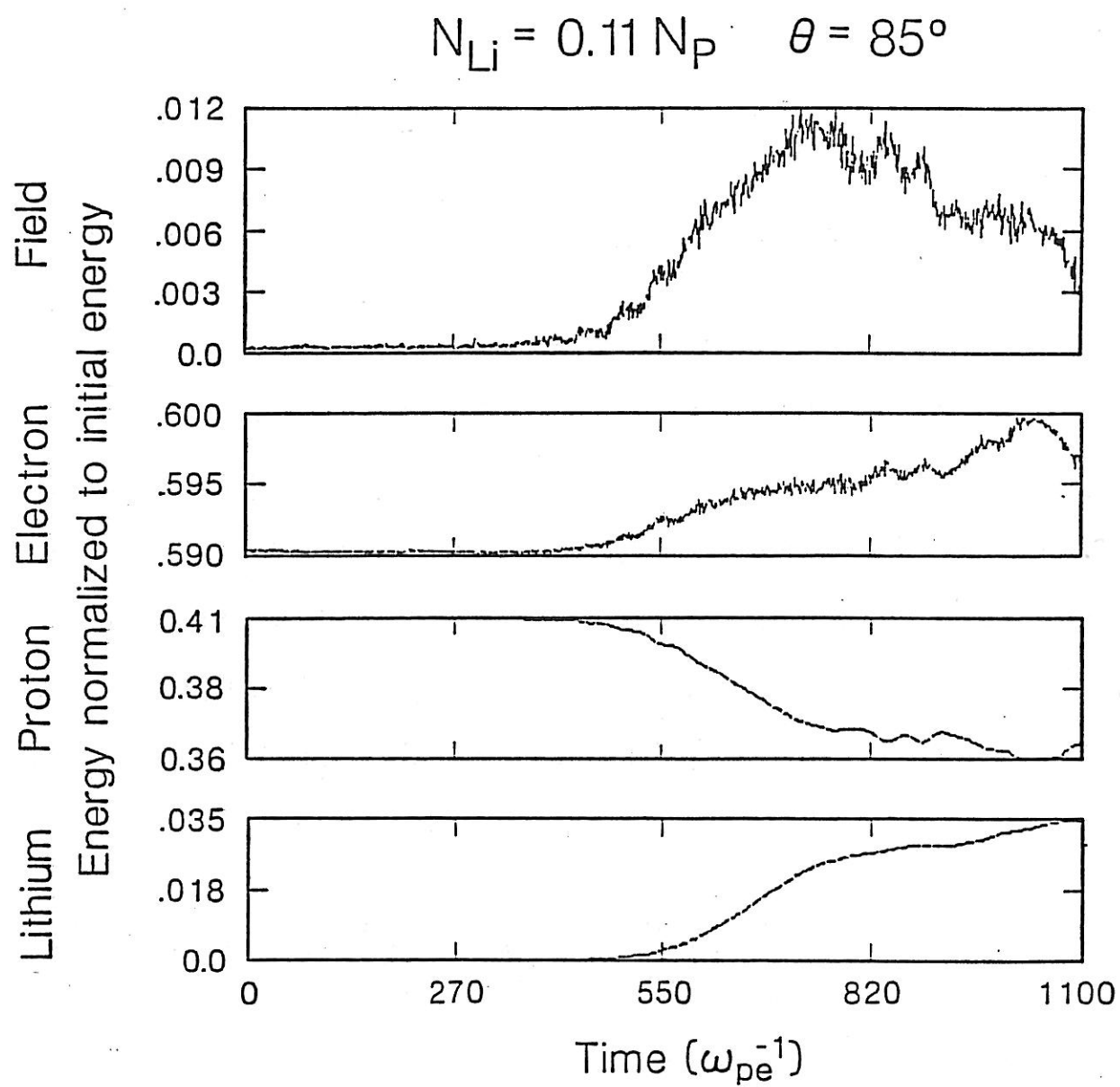


Figure 49

REFERENCES

- Anderson, R. R., D. A. Gurnett, B. Häusler, H. C. Koons, R. H. Holzworth, R. A. Treumann, O. H. Bauer, G. Haerendel, H. Lühr, L. J. Woolliscroft, and M. P. Gough, Electron number density from the AMPTE/IRM plasma wave experiment during solar wind lithium releases, J. Geophys. Res., submitted, 1985.
- Bridge, H. S., J. W. Belcher, A. J. Lazarus, S. Olbert, J. D. Sullivan, F. Bagenal, P. R. Gazis, R. E. Hartle, K. W. Ogilvie, J. D. Scudder, E. C. Sittler, A. Eviatar, G. L. Siscoe, C. K. Goertz, and V. M. Vasyliunas, Plasma observations near Saturn: Initial results from Voyager 1, Science, 212, 217, 1981.
- Broadfoot, A. L., B. R. Sandel, D. E. Shemansky, J. B. Holberg, G. R. Smith, D. F. Strobel, J. C. McConnell, S. Kumar, D. M. Hunten, S. K. Atreka, T. M. Donahue, H. W. Moos, J. L. Bertaux, J. E. Blamont, R. B. Pomphrey, and S. Linick, Extreme ultraviolet observations from Voyager 1 encounter with Saturn, Science, 212, 206, 1981.
- Coates, A. J., A. D. Johnstone, M. F. Smith, and D. J. Rodgers, AMPTE-UKS ion experiment observations of lithium releases in the solar wind, J. Geophys. Res., 91, 1311, 1986.
- Fried, B. D., and S. D. Conte, The Plasma Dispersion Function, Academic Press, New York, 1961.
- Fried, B. D., and A. Y. Wong, Stability limits for longitudinal waves in ion beam-plasma interactions, Phys. Fluids, 9, 1084, 1966.
- Gurnett, D. A., W. S. Kurth, and F. L. Scarf, Plasma waves near Saturn: Initial results from Voyager 1, Science, 212, 239, 1981.
- Gurnett, D. A., F. L. Scarf, and W. S. Kurth, The structure of Titan's wake from plasma wave observations, J. Geophys. Res., 87, 1395, 1982.
- Gurnett, D. A., R. R. Anderson, B. Häusler, G. Haerendel, O. H. Bauer, R. A. Treumann, H. C. Koons, R. H. Holzworth and H. Lühr, Plasma waves associated with the AMPTE artificial comet, Geophys. Res. Lett., 12, 851, 1985.

- Gurnett, D. A., T. Z. Ma, R. R. Anderson, O. H. Bauer, G. Haerendel, B. Häusler, G. Paschmann, R. A. Treumann, H. C. Koons, R. Holzworth, and H. Lühr, Analysis and interpretation of the shock-like electrostatic noise observed during the AMPTE solar wind lithium releases, J. Geophys. Res., 91, 1301, 1986a.
- Gurnett, D. A., R. R. Anderson, T. Z. Ma, G. Haerendel, G. Paschmann, O. H. Bauer, R. A. Treumann, and H. C. Koons, Waves and electrical fields associated with the first AMPTE artificial comet, J. Geophys. Res., in press, 1986b.
- Haerendel, G., G. Paschmann, W. Baumjohann, and C. W. Carlson, Dynamics of the AMPTE artificial comet, Science, submitted, 1985a.
- Haerendel, G., A. Valenzuela, H. Föppl, B. Häusler, F. Melzer, G. Paschmann, and J. Stocker, Physical properties of the lithium injection experiments in the solar wind, J. Geophys. Res., submitted, 1985b.
- Harris, E. G., Unstable plasma oscillations in the magnetic field, Phys. Rev. Lett., 2, 34, 1959.
- Hartle, R. E., E. C. Sittler, Jr., K. W. Ogilvie, J. D. Scudder, A. J. Lazarus, and S. K. Atreya, Titan's ion exosphere observed from Voyager 1, J. Geophys. Res., 87, 1383, 1982.
- Häusler, B., R. H. Holzworth, L. J. Woollischroft, R. R. Anderson, D. A. Gurnett, H. C. Koons, O. H. Bauer, G. Haerendel, A. G. Darbyshire, M. P. Gough, S. R. Jones, N. Klöcker, A. J. Norris, G. Paschmann, and A. Valenzuela, Plasma waves observed by the IRM and UKS spacecraft during the AMPTE solar wind lithium releases: Overview, J. Geophys. Res., 91, 1283, 1986.
- Krall, N. A., and A. W. Trivelpiece, Principles of Plasma Physics, McGraw-Hill, New York, 473, 1973.
- Lühr, H., N. Klöcker, D. J. Southwood, M. W. Dunlop, W. A. C. Mier-Jedrzejowicz, R. P. Rijnbeek, M. Six, B. Häusler, and M. Acuña, In situ magnetic field observations of AMPTE's artificial comet, Science, submitted, 1985.
- Lühr, H., D. J. Southwood, N. Klöcker, M. Acuña, B. Häusler, W. A. C. Mier-Jedrzejowicz, R. P. Rijnbeek, M. Six, In-situ magnetic field measurements during AMPTE solar wind Li^+ -releases, J. Geophys. Res., 91, 1261, 1986.
- Mendis, D. A., and B. T. Tsurutani, The spacecraft encounters of Comet Halley, EOS, 67, No. 20, 1986.

- Muller, D. E., A method for solving algebraic equations using an automatic computer, Math. Comp., 10, 208, 1956.
- Ness, N. F., M. H. Acuña, R. P. Lepping, J. E. P. Connerney, K. W. Behannon, L. F. Burlaga and F. M. Neubauer, Magnetic field studies by Voyager 1: Preliminary results at Saturn, Science, 212, 211, 1981.
- Neubauer, F. M., D. A. Gurnett, J. D. Scudder, and R. E. Hartle, Titan's magnetospheric interaction, Saturn, The University of Arizona Press, 760-781, 1984.
- Omidi, N., T. Z. Ma, M. Ashour-Abdalla, D. A. Gurnett and R. D. Syroda, Simulation of electrostatic waves generated during the AMPTE lithium release in the solar wind, EOS, 67, No. 16, p. 349, 1986.
- Paschmann, G., C. W. Carlson, W. Baumjohann, D. W. Curtis, N. Sckopke, and G. Haerendel, Plasma observations on AMPTE-IRM for the Li-Releases in the solar wind, J. Geophys. Res., 91, 1271, 1986.
- Rodgers, D. J., A. J. Coates, A. D. Johnstone, M. F. Smith, D. A. Bryant, D. S. Hall and C. p. Chaloner, UKS plasma measurements near the AMPTE artificial comet, Science, submitted, 1985.
- Rodriguez, P., Magnetosheath electrostatic turbulence, J. Geophys. Res., 84, 917, 1979.
- Salzer, H. E., Formulas for calculating the error function of a complex variable, Math. Tables, p. 67, 1951.
- Scarf, F. L., F. V. Coroniti, C. F. Kennel, D. A. Gurnett, W.-H. Ip, and E. J. Smith, ICE plasma wave observations, EOS, 66, No. 46, 1014, 1985.
- Scarf, F. L., W. W. L. Taylor, C. T. Russell, and R. C. Elphic, Pioneer Venus plasma wave observations: The solar wind-Venus interaction, J. Geophys. Res., 85, 7599, 1980.
- Shawhan, S. D., and G. B. Murphy, Plasma diagnostics package assessment of the STS-3 orbiter environment, J. Spacecraft and Rockets, Special STS-3/OSS-1 issue, 1983.
- Smith, G. R., D. F. Strobel, A. L. Broadfoot, B. R. Sandel, D. E. Shemansky, and J. B. Holweg, Titan's upper atmosphere: Composition and temperature from the EUV solar occultation results, J. Geophys. Res., 87, 1982.
- Stepanov, K. N., Low-frequency oscillations of a plasma in a magnetic field, Soviet Physics JETP, 35(8), 808, 1959.